Quantum dynamics of STM and laser induced desorption of atoms and molecules from surfaces

A thesis submitted in partial fulfilment of the requirements
for the degree of Doctor of Philosophy

by

Gisela Boendgen

Chemistry Department
University College London

December 2000

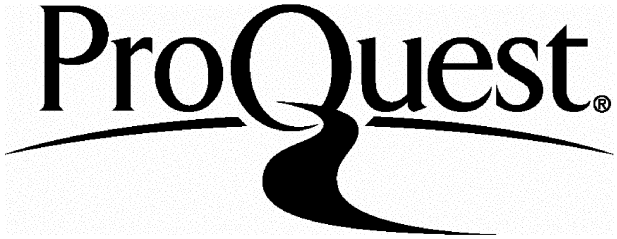

Abstract

The manipulation of atoms and molecules at solid surfaces by electronic excitations with electrons (or holes) emitted from the tip of a scanning tunneling microscope (STM) or with laser radiation is both of applied and fundamental interest, e.g. for micro- and nanostructuring of materials, the clarification of elementary (catalytic) reaction mechanisms and for the question of how to treat the quantum dynamics of a laser or STM driven "system" (the adsorbate) in contact with a dissipative (energy-withdrawing) "bath" (the substrate).

Desorption induced by electronic transitions (DIET) and its variant DIMET (M = multiple) are among the simplest possible "reactions" of adsorbate-surface systems; usually involving extremely short-lived electronically excited intermediates. In this thesis, the ultra-short dynamics of directly (localised to the adsorbate-substrate complex) and indirectly (i.e., through the substrate) stimulated DIET and DIMET processes was studied for Si(100)-(2x1):H(D) and Pt(111):NO.

Isotope effects and the influence of substrate temperature and applied electric fields on the desorption yields were examined and possibilities to actively control the outcome (e.g. yields, isotope ratios), for example by laser shaping techniques, were investigated.

For that purpose, time-dependent wave packet methods and open system density matrix theory were used to account for energy dissipation and thus resulting ultrashort lifetime of the electronically excited states involved.

Acknowledgements

First and foremost I wish to thank my supervisor, Professor Dr. Peter Saalfrank, for providing the opportunity, stimulation and support for this work. He always let me profit from his great knowledge and answered all my questions with immense patience. Thank you very much for everything, Peter!

Thanks must also go to the Deutsche Forschungsgemeinschaft DFG, project Sfb 450 TP C1 at Freie Universität Berlin, and to the UCL Chemistry Department for the financial support, without which my research work and my stay in London would have been impossible.

A very hearty "Thank you" to my (ex)-fellows Dr. Tillmann Klamroth and Mathias Nest for answering all my endless questions! And also for being quite interesting house mates; I learned a lot of fascinating things. Jungs, working (and living) with you was great fun!

Finishing this thesis would have been very difficult without the help of two dear friends: Maria and Erasmo. They not only offered me shelter, support and encouragement, but also the most delicious food. I will never be able to express how much your help meant to me, thank you very much!

Finishing, I would like to thank Dr. David Rowley for proofreading most of my thesis, and all other peoples, who have somehow contributed not only to this work but to life in general over the past two years.

Contents

Chapter 1

Introduction

1.1 General aspects

Surfaces play an important role in catalysis [1, 2], semiconductor technology [3, 4] and corrosion research [5, 6] and considerable progress in surface science has been achieved during recent years. A large variety of experimental techniques has been developed giving information about the geometric, electronic and vibrational structure of solid surfaces [2].

Lasers [7] and Scanning Tunneling Microscopes (STM) [8] are powerful tools for modern physics and physical chemistry in general and for surface science in particular. Beside their use for imaging or spectroscopically detecting the surface and the ad-species, they can also be used to actively manipulate them [9, 10]. Simple vibrational or rotational excitations of the adsorbate can be induced, as can specific lateral motion. Additionally, bond breaking can be enforced, leading to adsorbate dissociation or desorption of the adsorbed species.

These processes usually involve interactions of the adsorbate with a large number of degrees of freedom, e.g. lattice phonons or electron-hole pairs of a substrate, which makes a proper theoretical description very challenging. The presence of the surface provides new excitation/relaxation channels in addition to the ones that exist in the

gas phase. Energy dissipation may involve the transfer of energy and/or charged particles (e.g. electrons) between substrate and ad-species. A universal possibility for surface adsorbed particles is the energy transfer via phonon coupling. More efficient electronic couplings may operate on substrates with small or no band gaps; the details of the excitation/relaxation mechanisms usually depend on the substrate (see below).

Advances in surface preparation and vacuum techniques, and above all in laser technology [2], have led to an enormous increase of activity in the field of surface photochemistry [11, 12]. Major fields of interest include photo-excitation and relaxation mechanisms, adsorbate-surface interaction and the corresponding dynamics [7]. In many modern surface experiments, lasers are indispensable in detecting and analysing product quantum state distributions. Furthermore, laser photons have been shown to open new reaction channels which are not accessible by thermal activation [7]. The resolution of low-energy continuous wave lasers allows one to concentrate on specific dynamical processes with minimal interferences from unwanted processes. With pulsed femtosecond lasers, the study of the chemistry of individual bonds is possible and dynamics and reaction time scales can be probed rigorously [13].

The invention of the Scanning Tunneling Microscope (STM) [8] has allowed probing of material structure and chemical reactions with atomic resolution. Furthermore, the possibility to induce *local* bond breaking allows surface modification of materials at the atomic and nanometer scale [14].

There are four basic mechanisms underlying the spatially resolved manipulation and chemistry with STM, which involve atomic forces, tunneling and field-emitted electrons and the electric field. While atomic forces are mainly used to slide and push atoms and molecules along the surface [15, 16], tunneling electrons can be used to enforce desorption of adatoms [17, 18, 19] or to transfer single atoms [20, 21] or molecules reversibly [22] between substrate surface and the STM tip ("atomic switch", see also [23]).

1.2 Excitation mechanisms

The manipulation of adsorbates can be initiated by photons, electrons, holes, or ions. The possible outcomes are, for example, vibrational or rotational excitations of the adsorbate [7, 24, 17], dissociation of the ad-species or the desorption of atoms and molecules from the surface [7, 25]. Desorption is not only the best studied "reaction" of them all, it is also of practical relevance for the nanostructuring of materials and the passivation of microelectronic devices [26].

Laser and STM-induced desorption via short-lived electronic states is the main subject of this thesis. One can distinguish between *direct* and *indirect* substrate-mediated excitation mechanisms [27]. In surface-photochemistry, the direct mechanism prevails typically for insulator and semiconductor surfaces and results from the coupling between the radiation field and the transition dipole moment of the adsorbate. On metal surfaces, an indirect mechanism predominates. UV/vis lasers create "hot electrons", i.e. electron/hole pairs, in the solid which can tunnel to empty resonant adsorbate levels thus driving the adsorbate-substrate dynamics indirectly [27].

The initial excitation of an adsorbate on a metal surface is typically short-lived ($\sim$ femtoseconds) since the resonant electronic level of the adsorbate is broadened due to coupling to the continuum states of the metal. In photochemistry, direct and indirect excitation mechanisms can be distinguished experimentally by the dependence of the cross section on the angle of incidence and the polarization of the laser light. In case of a substrate mediated process, the desorption yield scales with substrate absorptivity, whereas for direct excitations it scales only with the magnitude of the electric field. In case of indirect electronic excitation involving electronically excited states, one can distinguish between the single and the multiple excitation limits on the time scale of the vibrational relaxation of the adsorbate. Continuous wave (cw) or nanosecond (ns) lasers with low laser intensities produce only a small concentration of hot electrons and thus rare excitation events. Because

each desorbed particle has been excited initially only once, the desorption process is characterized as DIET (*Desorption Induced by Electronic Transitions*, single excitation limit). Intense laser pulses in the pico- or femtosecond regime create a high density of electron/hole pairs in the metal surface, thus leading to multiple excitation/deexcitation of the adsorbate (DIMET, *Desorption Induced by Multiple Electronic Transitions*, multiple-excitation limit).

DIET and DIMET can cause very different experimental outcomes [28]. In photochemistry, DIMET can be distinguished from DIET by various characteristics, the so-called "DIMET hallmarks"[28]: (1) The desorption yields are usually higher in DIMET; (2) the desorbates are translationally and vibrationally "hotter" in DIMET; (3) the desorption yield scales linearly with the laser fluence $\mathcal{F}$ in case of DIET and according to $\mathcal{F}^n (n > 1)$ for DIMET; (4) the translational and vibrational energy of the desorbates is independent of $\mathcal{F}$ in the case of DIET, while they increase with the laser fluence in the case of DIMET.

Somewhat analogous to DIET and DIMET are desorption mechanisms induced by STM electrons at positive sample bias, where it is possible to delineate two distinct mechanistic routes as well. High energetic, field-emitted electrons from the STM tip can cause direct excitation of the adsorbate. When the electron energy exceeds a certain threshold to form a resonance, i.e., a short-lived electronically excited intermediate, eventually the surface-adsorbate bond can break ("above threshold mechanism"). On the other hand, lower energetic electrons tunneling from the STM tip to the adsorbate system can induce multiple vibrational excitation and desorption becomes possible by "vibrational ladder climbing" ("below threshold mechanism") [14, 29]. The "ladder climbing" pathway is often less efficient than the "above threshold mechanism" and is relevant only for systems with long vibrational lifetimes.

Vibrational heating is also believed to be the underlying microscopic mechanism in recent STM desorption experiment by Stokbro et al. at negative sample bias. In this case, holes instead of electrons tunnel from the tip towards the sample. A

desorption mechanism was suggested which involves inelastic scattering of a tunneling hole with a hole resonance on the sample, thus causing "vibrational ladder climbing" and subsequent desorption [30].

1.3 Dissipation

A significant difference between the dynamics on solid surfaces and its corresponding gas-phase counterpart is the influence of surfaces and adsorbate phonons and/or electron-hole pairs. The surface provides the adsorbate system with a dissipative environment. Due to the environment not only is indirect adsorbate excitation (see above) possible, but energy and phase relaxation of an excited adsorbate is possible by interaction with the environment. Energy can be transferred to substrate phonons, for example, or temporary trapped electrons can tunnel back to the substrate conduction band after excitation. Dissipation phenomena on surfaces often lead to ultrashort excitation lifetimes in the range of 10^{-13} to 10^{-15} seconds for electronic and 10^{-9} to 10^{-12} for vibrational excitations. The dissipation can significantly influence the primary dynamics, thus a crucial point in theoretical surface chemistry is the treatment of the interaction between the adsorbate, the surface and the excitation source (e.g. photons, electrons).

In surface-adsorbate systems, dissipation occurs microscopically through non-adiabatic coupling of the electronic states. The electronic excitation and quenching process has for example been described by multiple state models [31] or by explicit inclusion of electronic degrees of freedom [32]. However, in practice mostly a phenomenological relaxation rate is chosen to fit experimental data and dissipation, in particular continuous electronic quenching, can be included in the dynamics calculation via imaginary potentials [31, 29].

A consistent quantum treatment of a so-called *open system* is possible within the framework of open system density matrix theory [33]. Dissipation is included here as an additional term to the Hamiltonian (dissipation-free) formulation of the nuclear

time evolution. The underlying equation of motion is the *Liouville - von Neumann* equation, for which efficient algorithms for the numerical integration have been developed within recent years [34, 35, 36]. There are different alternatives for the treatment of the dissipative term, for example the dynamical semigroup ansatz by Lindblad [37] or the treatment of the dissipation in a microscopical theory according to Redfield [38].

1.4 Models for the desorption processes

Traditionally, desorption resulting from non-adiabatic electronic transitions has been described with the help of simple models. Typically, just two electronic states and the desorption coordinate [1] as a single mode are included. In the original variants, the adsorbate motion was treated classically.

The two most prominent models of this type are the Menzel-Gomer-Redhead (MGR) [39, 40] and the Antoniewicz model [41]. In the former, shown in Fig.1.1, an initial Franck-Condon transition is assumed from a bound electronic ground state $|g\rangle$ to a *repulsive* excited state $|e\rangle$, where the adsorbate moves *outward*, i.e., further away from the surface. The coupling of the adsorbate to the electronic or phonon degrees of freedom of the substrate causes ultrafast energy relaxation (quenching) back to the ground state, from where the particle can desorb if it has gained enough kinetic energy in the excited state.

In contrast to the MGR model, the electronically excited state in the Antoniewicz model is a bound state (see Fig.1.2). The excited state equilibrium bond length is shorter than in the ground state, hence the excited adsorbate moves initially *towards* the surface before relaxation to the ground state and eventually desorption occurs. This scenario was suggested by Antoniewicz for the electron- or photon-induced desorption of neutral species from a metal surface. A charge transfer from the metal to the adsorbate after the initial excitation is assumed. The now negatively

[1] usually the distance of the centre-of-mass of the desorbing species from the surface

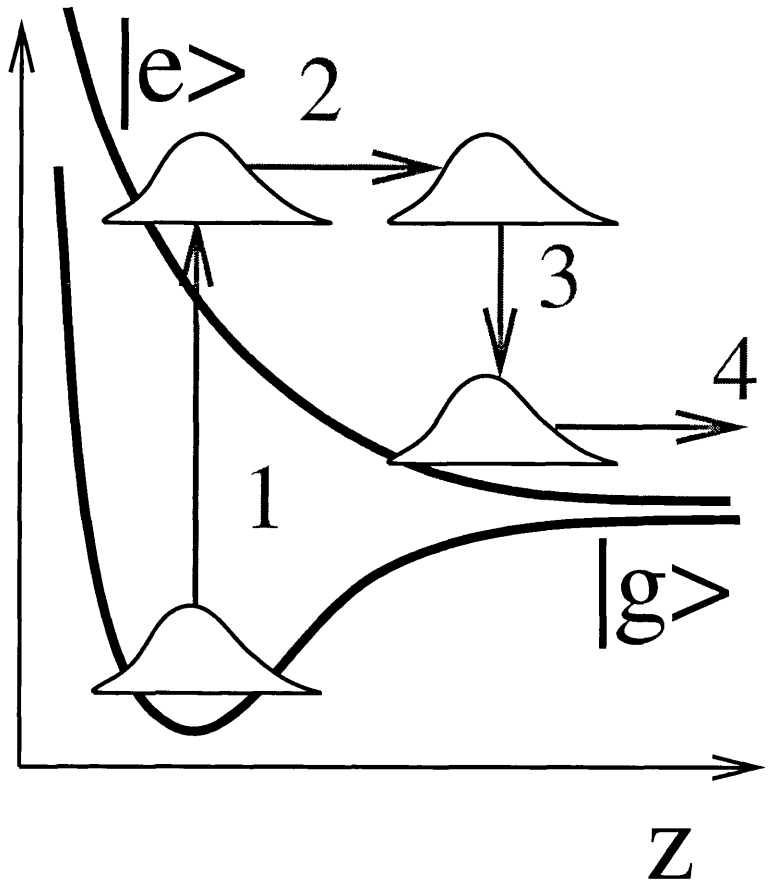

Figure 1.1: *Menzel-Gomer-Redhead model for the photo-induced desorption from solid surfaces. After an initial Franck-Condon transition (1) from the electronic ground to the excited state, the system evolves there for a short time and moves towards larger adsorbate-surface distance Z (2) before it relaxes back to the ground state (3). Bond breaking (4) can occur if the particle has gained enough kinetic energy on the excited state surface.*

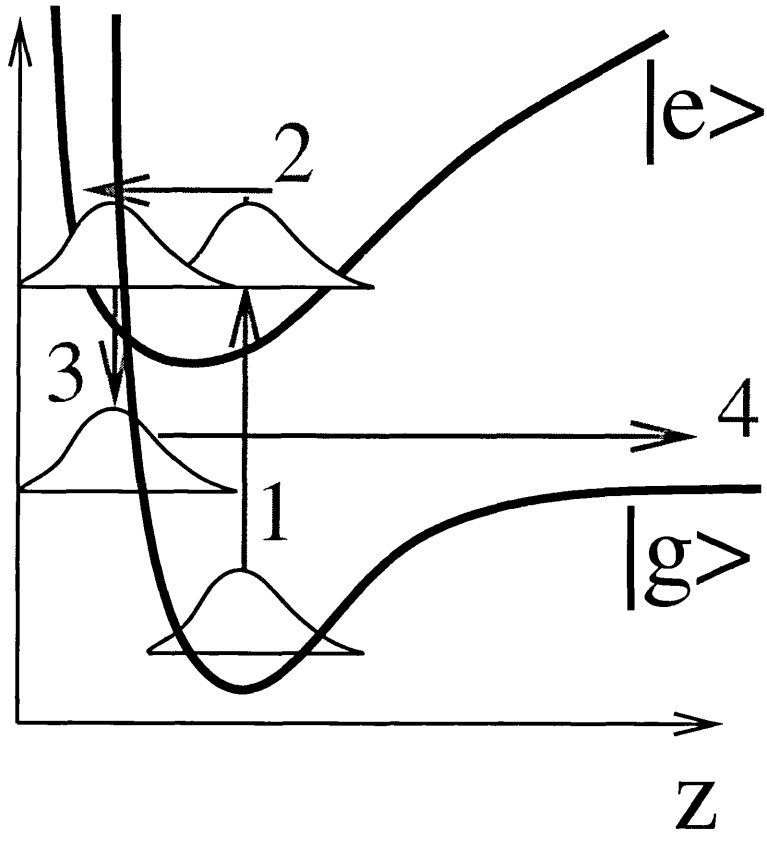

Figure 1.2: *Antoniewicz model for the electron- or photon-stimulated desorption from metal surfaces. After the initial Franck-Condon excitation to the excited state* $|e\rangle$ *(1), the now negatively or positively charged adsorbate is attracted to the surface by an image-potential. The system evolves in the excited state towards the surface (2) before it is quenched back to the ground state* $|g\rangle$ *(3). From there it can desorb if it has gained enough potential energy in the excited state.*

or positively charged adsorbate is initially attracted to the surface by an image-potential, before the electronic quenching occurs on an ultrashort time scale.

Despite being very simple, both the MGR and the Antoniewicz model were remarkably successful in explaining a wide range of phenomena, such as subtle isotope and temperature effects, non-thermal energy distribution of desorbates, or "threshold" and "resonance" effects for excitation wave length (in photochemistry) or electron energies (in electron-stimulated desorption). To explain specific observations for specific systems, both scenarios were improved in many ways in recent years years[12]: (1) Multi-state rather than two state models were developed; (2) quantum effects for the nuclear motion were included, and (3) multi-dimensional models including internal adsorbate modes were proposed.

1.5 Outline of the work

The outline of this thesis is as follows: First, in section 2, general aspects of the models and the theoretical simulations are outlined. The open system density matrix approach is reviewed and different quantum dynamical methods to solve the underlying Liouville - von Neumann equation are introduced.

In section 3, the *STM-induced desorption* of hydrogen and deuterium from a Si(100)-(2x1):H/D surface is investigated, both in the "above" (section 3.2) and the "below threshold" regime at positive sample bias (section 3.4), as well as with negative sample bias (section 3.2.6). The general influence of the external field present in the STM is studied in section 3.3.

For the STM-induced desorption following the "above threshold" mechanism, the (hypothetical) case of coordinate-independent decay of the electronically excited state is considered in subsection 3.2.3 to address isotope effects and to quantify the importance of a quantum treatment. The effects of coordinate-dependent electronic relaxation are investigated in subsection 3.2.4, and finite surface temperature is included in subsection 3.2.5.

Different models for the excitation and dissipation rates are discussed in subsections 3.4.4 and 3.4.5 for the STM-induced desorption in the "below threshold" limit. Surface temperature effects and the dependence of the desorption yields on the tunneling current and the applied voltage are studied in subsection 3.4.6.2.

In section 4, the *laser-induced desorption* of H and D from Si(100)-(2x1):H/D is considered and the use of femtosecond lasers is suggested to influence the desorption yields and the corresponding isotope ratios.

In the final part of this work, the photo-induced desorption of NO from Pt(111) (section 5) is investigated. This system is one of the best studied metal/adsorbate systems (see for example [42, 43, 44, 31, 45, 46, 35, 47, 48, 49]). For this system an indirect, "hot" substrate electron excitation mechanism is assumed [48, 49]. Two-dimensional generalized model potentials, including the NO-Pt distance and the NO vibrational coordinate, are adopted from Sathyamurthy and co-workers [47] and the nuclear desorption dynamics is studied within the DIET (section 5.4) as well as the DIMET limits (section 5.5).

For DIET, the relevance of the negative ion model is systematically addressed and the effects of coordinate-dependent electronic quenching are investigated. Finally, the sub-ps laser-induced DIMET dynamics is studied and the translational and vibrational energies of the desorbates are compared for the DIET and DIMET case. A final section 6 concludes this work.

Chapter 2

Quantum dynamical methods

2.1 Outline of density matrix theory

2.1.1 The density matrix formalism

The dynamics of simple, isolated systems like the harmonic oscillator or the hydrogen atom can be described by the time-dependent Schrödinger equation [1]

$$i\hbar\frac{\partial}{\partial t}|\Psi(t)\rangle = \hat{H}|\Psi(t)\rangle \quad . \tag{2.1}$$

An unambiguous solution, $|\Psi(t)\rangle$, of this first-order differential equation is obtained by determining an initial wave function $|\Psi(t=0)\rangle$. Provided Eq.(2.1) can be solved, the time-dependence of physical observables is given by the expectation values of the related Hamiltonian $\hat{H}$ with respect to the time-dependent wave function.

However, under most real life conditions systems are hardly isolated and perturbations from the environment have to be taken into account. Often the disturbances of the relevant system by the environment are weak and can be neglected at first. If the environment is characterised only by a small number of degrees of freedom one can attempt to solve the time-dependent Schrödinger equation again, but now for the

[1] The Schrödinger equation is universal, but so far, unfortunately, it can be solved exactly for systems with few degrees of freedom only.

system and the *small* environment. Unfortunately, such an approach is impossible if the environment is large, i.e. forming a macroscopic system. This could be a condensed phase (with or without a finite macroscopic temperature) or a large molecule as scaffold surrounding a small, active quantum system, e.g. a chromophore. In this case one has to resort to statistical methods.

Any coupling of an *open system* to the external degrees of freedom of a *"bath"* results in energy exchange between the system and its environment. If initially energy is disposed in the system, this will be transfered to the environment, i.e., degrees of freedom of the surrounding bath accept the energy and distribute it among themselves. If the reservoir is a macroscopic system, the energy dissipates over the huge number of degrees of freedom and the environment does not "feel" this increase of internal energy. The energy transfer from the system to the bath is termed *relaxation.* If there is no chance for the energy to move back into the system, the unidirectional energy exchange with the environment is called *dissipation.* Obviously, on short time scales the distinction between relaxation and dissipation is likely to be blurred and hence there is no strict discrimination of both terms in the literature.

A consistent quantum mechanical description of *open systems* coupled to an environment is possible by density matrix theory, where the concept of the density matrix represents a combination between a quantum-mechanical and a statistical description of the system.

The density operator $\hat{\rho}$ for a system represented by a mixture of pure states is defined as:

$$\hat{\rho} = \sum_k p_k |\Psi_k\rangle\langle\Psi_k| \quad . \tag{2.2}$$

p_k can be interpreted as the probability to find the system in a pure state k described by the state vector $|\Psi_k\rangle$ with

$$0 \leq p_k \leq 1 \quad \text{and} \quad \sum_k p_k \;=\; 1 \qquad .$$

By representing $\hat{\rho}$ within an orthonormal basis $\{|\phi_n\rangle\}$, e.g. eigenfunctions of $\hat{H}$ with coefficients a_{nk}, one can describe the density operator as matrix $\underline{\underline{\rho}}$ with

elements:

$$\rho_{nm} = \langle\phi_n|\hat{\rho}|\phi_m\rangle = \sum_k p_k \langle\phi_n|\Psi_k\rangle\langle\Psi_k|\phi_m\rangle = \sum_k p_k a_{nk} a^*_{mk} \quad . \tag{2.3}$$

The diagonal elements ρ_{nn} represent the population of state $|\phi_n\rangle$, while the off-diagonal elements ρ_{nm} describe the coherences between state $|\phi_n\rangle$ and $|\phi_m\rangle$. For the norm of $\hat{\rho}$ one obtains:

$$\begin{aligned} Tr\{\hat{\rho}\} &= Tr\{\underline{\underline{\rho}}\} \\ &= \sum_{n=1}^{N} \rho_{nn} \\ &= \sum_n \sum_k p_k \langle\phi_n|\Psi_k\rangle\langle\Psi_k|\phi_n\rangle \\ &= \sum_k p_k \sum_n \langle\Psi_k|\phi_n\rangle\langle\phi_n|\Psi_k\rangle \\ &= \sum_k p_k = 1 \end{aligned} \tag{2.4}$$

by using the completeness relation $\sum_n |\phi_n\rangle\langle\phi_n| = 1$.

The expectation values of operators $\hat{A}$ are given from the trace relation:

$$\begin{aligned} \langle\hat{A}\rangle &= Tr\{\hat{\rho}\hat{A}\} = \sum_k p_k \langle\Psi_k|\hat{A}|\Psi_k\rangle \\ &= \sum_{n,m} \rho_{nm} A_{nm} \quad . \end{aligned} \tag{2.5}$$

In general, the expectation values depend on both the populations ρ_{nn} and the coherences ρ_{nm}. In particular, if the $|\phi_n\rangle$ are eigenfunctions of $\hat{H}$, then for all operators $[\hat{H}, \hat{A}] \neq 0$ the off-diagonal elements ρ_{nm} of $\underline{\underline{\rho}}$ contribute to $\langle\hat{A}\rangle$.

2.1.2 Time evolution of $\hat{\rho}$: The Liouville - von Neumann equation

In a *closed* system, the time-evolution of $\hat{\rho}$ is given by the non-dissipative *Liouville - von Neumann equation*:

$$i\hbar\frac{\partial}{\partial t}\hat{\rho} = i\hbar\frac{\partial}{\partial t}\sum_k p_k |\Psi_k\rangle\langle\Psi_k|$$

$$
\begin{aligned}
&= i\hbar \sum_k p_k \Big(|\frac{\partial}{\partial t}\Psi_k\rangle\langle\Psi_k| + |\Psi_k\rangle\langle\frac{\partial}{\partial t}\Psi_k| \Big) \\
&= i\hbar \sum_k p_k \Big[\frac{1}{i\hbar} \Big(|\hat{H}\Psi_k\rangle\langle\Psi_k| - |\Psi_k\rangle\langle\Psi_k|\hat{H} \Big) \Big] \\
&= [\hat{H}, \hat{\rho}] \quad . \qquad (2.6)
\end{aligned}
$$

This equation is equivalent to the time-dependent Schrödinger equation (2.1) and has the formal solution:

$$
\begin{aligned}
\hat{\rho}(t) &= e^{\mathcal{L}_0 t}\hat{\rho}(0) =: \hat{\Upsilon}\,\hat{\rho}(0) \quad , \qquad (2.7) \\
\text{with:} \qquad \mathcal{L}_0 &= -\frac{i}{\hbar}[\hat{H}, \circ]
\end{aligned}
$$

where $\circ$ stands for the operator the Liouvillian superoperator will operate on. The propagator $\hat{\Upsilon}$ maps the density matrix at time t_0 on the density matrix at time $t_0 + t$. The practical solution of Eq.(2.7), however, requires the propagation of a density matrix rather than state vectors. This disadvantage of density matrix theory is only in certain cases outweighed by the advantage that both the time evolution of mixed and pure states can be considered with a single propagation. In contrast, to treat e.g. a thermal ensemble within the Schrödinger equation, a wave packet propagation has to be done separately for each of the pure states contributing to it.

Obvious advantages of density matrix theory whereas arise from its use in *open system* quantum dynamics where the coupling to the environment allows for energy and phase relaxation of the system. If the system and the bath are initially separable, it can be shown that the system is described by the *"reduced density operator"* $\hat{\rho}_s$, which statisfies the dissipative (non-Markovian) Liouville - von Neumann equation [33]

$$
i\hbar\frac{\partial}{\partial t}\hat{\rho}_s = i\hbar\,\mathcal{L}\hat{\rho}_s(t) = [\hat{H}_s, \hat{\rho}_s(t)] + \int_0^t d\tau \mathcal{L}_D(t,\tau)\{\hat{\rho}_s(\tau)\} \qquad (2.8)
$$

in which the bath can be left out of the dynamics, but its effects on the system are reproduced indirectly in this equation of motion. The reduced density operator $\hat{\rho}_s$ is the trace of the total density over the bath modes and depends only on a limited

number of relevant system degrees of freedom:

$$\hat{\rho}_s(t) := Tr_B\{\hat{\rho}(t)\} = \sum_\alpha \langle\alpha|\hat{\rho}(t)|\alpha\rangle \quad , \tag{2.9}$$

where $|\alpha\rangle$ are eigenstates of the bath Hamiltonian $\hat{H}_B$. The unobserved environment now enters solely as a dissipative correction to the Hamiltonian evolution. The Hamiltonian is also indicated with $\hat{H}_s$ to stress that it only refers to the system. It is an effective Hamiltonian because even though it depends only on the system modes, it includes the static (averaged) distortion of the system dynamics that is due to the environmental degrees of freedom.

The dissipative part $\int_0^t d\tau \mathcal{L}_D(t,\tau)\{\hat{\rho}_s(\tau)\}$ depends on the fluctuations of the bath variables. It accounts for energy and phase relaxation, i.e., the modification of the distribution Eq.(2.2). In general, the time evolution of the density operator is *"non-Markovian"* meaning that the density operator at time t depends on all previous states at all times τ; the system develops a memory because the relative "answer of the environment" depends on how the relevant system behaved in the past.

To have the dynamics local in time, the so-called *Markov approximation* has to be made. It is valid when the environment needs much less time to go back to the equilibrium than the system to change significantly, i.e. when the correlation time of the bath is much smaller than the characteristic time scale of the system. The Markov approximation breaks down if the bath correlation times are long, e.g. when the environment is represented by slowly moving solvent molecules or low frequency phonons. Under the Markov approximation, i.e., when memory effects are neglected, Eq.(2.8) turns into [33]:

$$\frac{\partial}{\partial t}\hat{\rho}_s = \mathcal{L}\hat{\rho}_s(t) = -\frac{i}{\hbar}[\hat{H}_s, \hat{\rho}_s(t)] + \mathcal{L}_D\hat{\rho}_s(t) \quad . \tag{2.10}$$

Here $\mathcal{L}_D\hat{\rho}_s(t)$ is a function of $\hat{\rho}_s$ at time t only and is usually linear.

For the proper choice of this dissipative part one has several possibilities [2]. Within the Markov approximation, the Redfield theory [38] and the dynamical

[2]How to choose the actual form form of $\mathcal{L}_D$ is still a matter of dispute!

semigroup approach by Lindblad and Kossakowski [50, 51] are the most widely used alternatives. In Redfield theory, one starts from the complete system and eliminates the environmental degrees of freedom by projector operator techniques. This is combined with perturbation theory to treat the system-bath coupling microscopically. However, Redfield theory is known to violate *complete positivity*, which makes it impossible to generally interpret the diagonal elements of the density matrix as probabilities.

The Lindblad formalism is more phenomenological and preserves complete positivity by construction. Within this approach, the dissipative part of Eq.(2.10) becomes

$$\mathcal{L}_D\hat{\rho}_s = \sum_{k=1}^{K}(\hat{C}_k\hat{\rho}_s\hat{C}_k^\dagger - \frac{1}{2}[\hat{C}_k^\dagger\hat{C}_k, \hat{\rho}_s]_+) \tag{2.11}$$

with $\hat{C}_k$ being the so called Lindblad operators. They determine "what" dissipates "how fast" in each of the K dissipative channels k; $[\ \ ]_+$ denotes the anti-commutator. The operators $\hat{C}_k$ are often chosen to fit selected experimental data, e.g. vibrational lifetimes.

In this work, the Lindblad form is used in all the dissipation models, because the interest in small (desorption) probabilities demands a strict positive density matrix. Furthermore, the complexity of the systems studied (with electron-hole pairs, phonons and multiple electronic surfaces) makes it almost impossible to derive sensible dissipation operators microscopically.

2.2 Numerical realization of the time propagation

How to represent the operators necessary to portray the phenomena under study and how to approximate the time evolution determined by the dissipative Liouville - von Neumann equation are essential points in the treatment of realistic systems.

For the time evolution of a density matrix, there are two main approaches:

(i) a *direct* strategy, where Eq.(2.8) or Eq.(2.10) is solved by propagating the

density operator, or

(ii) *indirect* schemes, where many different wave packets are propagated and the observables are computed via incoherent averaging.

The direct approaches are usually general, being equally applicable to Redfield or Lindblad types of dissipation, as well as to non-Markovian forms. A disadvantage of the direct methods is their unfavourable memory requirement, which scales at least as L^2 (the size of the density matrix is LxL) where L is the size of the Hilbert space of the system. The wave packet based indirect methods usually offer considerable savings, because only L component vectors (wave functions) have to be propagated. However, this has to be done N times to compute the observables via incoherent summation. In cases where $N < L$, not only memory can be saved, but even a speed-up in computational time relative to the direct method is possible.

2.2.1 The Newton interpolation – a direct method

In the direct methods, a single density matrix is propagated forward in time; in the Markovian case

$$\hat{\rho}_s(t) = e^{\mathcal{L}\,t}\hat{\rho}_s(0) \quad . \tag{2.12}$$

The total Liouvillian $\mathcal{L} = \mathcal{L}_0 + \mathcal{L}_D$ is not Hermitian and the eigenvalues $\{\lambda_l\}$ in the eigenvalue equation

$$\mathcal{L}\hat{E}_l = \lambda_l \hat{E}_l \tag{2.13}$$

are complex. Eq.(2.12) can be generally defined by spectral decomposition and for a restricted, discrete spectrum be formulated as follows [34]:

$$\hat{\rho}_s(t) = \sum_i e^{\lambda_i\,t}\,\hat{E}_i\,Tr\{\hat{E}_i^{\dagger}\hat{\rho}_s(0)\} \quad . \tag{2.14}$$

If the eigenvalues $\{\lambda_i\}$ and the eigenoperators $\{\hat{E}_i\}$ are known, the time evolution is given analytically. However, the solution of the eigenvalue problem Eq.(2.13) is

not only costly (for L basis functions a $L^2 \times L^2$ matrix has to be diagonalised), but sometimes even impossible.

Alternatively, the function $f(x) := f(\mathcal{L}t) = e^{\mathcal{L}t}$ can be exactly represented by a Lagrange polynomial $I_l(x) = \sum_{i=0}^{l} f(\lambda_i t) \cdot \Lambda_i(x)$, when the $l+1 = L^2$ eigenvalues λ_i of $\mathcal{L}$ are used

$$\begin{aligned} e^{\mathcal{L}t} &= \sum_{i=0}^{l} f(\lambda_i t) \cdot \Lambda_i(\mathcal{L}t) \qquad (2.15) \\ &= \sum_{i=0}^{l} e^{\lambda_i t} \cdot \frac{(\mathcal{L} - \lambda_l \hat{\Im}) \cdots (\mathcal{L} - \lambda_{i+1}\hat{\Im})(\mathcal{L} - \lambda_{i-1}\hat{\Im}) \cdots (\mathcal{L} - \lambda_0 \hat{\Im})}{(\lambda_i - \lambda_l) \cdots (\lambda_i - \lambda_{i+1})(\lambda_i - \lambda_{i-1}) \cdots (\lambda_i - \lambda_0)} \end{aligned}$$

with $\Im$ being the identity superoperator. Eq.(2.15) is equivalent to Eq.(2.14), hence

$$\prod_{k \neq i} \frac{(\mathcal{L} - \lambda_k \Im)}{(\lambda_i - \lambda_k)} = \hat{E}_i \, Tr\{\hat{E}_i^{\dagger} \circ\} \quad . \qquad (2.16)$$

The function $f(\mathcal{L}t)$ can also be exactly represented by a Newton polynomial

$$e^{\mathcal{L}t} = \sum_{j}^{l} c_j \cdot N_j(\mathcal{L}t) \qquad (2.17)$$

with

$$c_j = f(\lambda_0, \lambda_1, \ldots, \lambda_j) \cdot t^{-j} \qquad (2.18)$$

and

$$N_j(\mathcal{L}t) = (\mathcal{L} - \lambda_{j-1}\Im)(\mathcal{L} - \lambda_{j-2}\Im) \cdots (\mathcal{L} - \lambda_0 \Im) t^j \quad . \qquad (2.19)$$

Unfortunately, Eq.(2.17) still requires knowledge of $\{\lambda_i\}$. To avoid the diagonalisation of $\mathcal{L}$, one can approximate the propagator by using

$$e^{\mathcal{L}t} \approx \sum_{j=0}^{M} \tilde{c}_j \cdot \tilde{N}_j(\mathcal{L}t) \quad . \qquad (2.20)$$

The coefficients are now functions of the sampling points $\{z_j\}$

$$c_j = f(z_0, z_1, \ldots, z_j) \cdot t^{-j} \quad \text{with } j = 0, 1, \cdots, M \quad . \qquad (2.21)$$

The sampling points are still complex, but not identical to $\{\lambda_l\}$ and the number $m = M+1$ of sampling points is smaller than the number of eigenfunctions, l. With

the approximated polynomial Eq.(2.20) the propagator $e^{\mathcal{L}t}$ becomes

$$\begin{aligned} e^{\mathcal{L}t} \approx\ & \check{c}_0\hat{\Im} + \check{c}_1(\mathcal{L} - z_0\hat{\Im}) + \check{c}_2(\mathcal{L} - z_1\hat{\Im})(\mathcal{L} - z_0\hat{\Im}) + \cdots \\ & + \check{c}_m(\mathcal{L} - z_{m-1}\hat{\Im})(\mathcal{L} - z_{m-2}\hat{\Im}) \cdots (\mathcal{L} - z_0\hat{\Im}) \end{aligned} \tag{2.22}$$

where

$$\check{c}_j := \tilde{c}_j \cdot t^j = f(z_0, z_1, \ldots, z_j) \quad . \tag{2.23}$$

The eigenvalue spectrum of $\mathcal{L}$ is located in the left half of the complex plane. The complex sampling points are located on a rectangle extending from $-i/\hbar\,\varepsilon_{max}$ to $+i/\hbar\,\varepsilon_{max}$ along the imaginary axis, and from 0 to $-W_{max}$ on the real axis, where ε_{max} is the Hamiltonian energy maximum and W_{max} the maximum dissipative rate. Because $f(z_0, z_1, \ldots, z_j)$ is an analytical function, it is uniquely defined by its function values on the "domain boundary"[52] and it was shown by Berman et al. [34] that one obtains "nearly" optimal interpolation polynomials, if the sampling points $\{z_j\}$ are uniformly distributed on the domain boundary. If the domain is the unit circle, this regular distribution is given by

$$z_k = e^{i\varphi_k} = e^{i2\pi k/m} \qquad \text{with } k = 0, 1, ..., M \quad . \tag{2.24}$$

There are conformal mapping schemes for domains of other shape. If the target is a polygon (e.g. a 4-polygon like a rectangular defined around the eigenvalue spectrum of $\mathcal{L}$), the mapping can be done with the help of Schwarz-Christoffel conformable mapping [53]. Alternatively, especially for higher polynomial orders, one can determine the sampling points via the so-called Leja algorithm [54].

By using the Newton interpolation scheme, one avoids the prohibitively expensive and memory-consuming diagonalisation of a four index Liouvillian matrix. Only three $L \times L$ matrices have to be kept in central memory and only actions of type $\mathcal{L}\hat{\rho}_s$ are required. The Newton algorithm for density matrix propagation can be summarised as follows:

1. Initiation

- choose basis for operator representation
- calculate matrix elements
- construct initial density matrix $\hat{\rho}_s(0)$

2. Propagation

- define domain in complex plane
- determine sampling points [3]
- calculate $\mathcal{L}\hat{\rho}_s$ in each time step of the propagation cycle

3. Final analysis

Details about the representation and the propagation parameters will be given in the application sections.

2.2.2 Stochastic wave packet methods

As an alternative to the direct solution of the Liouville - von Neumann equation (2.10) described in the previous chapter 2.2.1, one can use indirect, wave packet based methods. These methods are not always general and the methods described below were known only for dissipative models of Lindblad form [55] in the first place. However, there are recent extensions of stochastic wave packet methods for Redfield dissipation [56, 57] and even non-Markovian dissipation [58].

A stochastic method in which the dissipation is taken into account by random quantum jumps is the widely used *Monte Carlo Wave Packet Method* (MCWP), developed by Mølmer and co-workers [55, 59]. Here, the density matrix is replaced by an ensemble of wave functions whose dynamics follows a non-Hermitian time-dependent Schrödinger equation. In each time step, a random number is generated, which determines whether a quantum jump occurs or not (see section 2.2.2.1).

[3] Within this work, the Schwarz-Christoffel conformable mapping was used.

An interesting alternative is the "jumping wave packet and weighted averaging scheme", developed by Gadzuk et al. [42]. For simple forms of dissipation, the distribution of the MCWP probabilities can be determined analytically [42] or semi-analytically [60]. The wave functions are then propagated with the time-dependent Schrödinger equation and undergo jumps out of a time distribution. The observables are finally computed via incoherent averaging. The method is described in detail in section 2.2.2.2 and 2.2.2.3.

2.2.2.1 Monte Carlo wave packet approach

The MCWP algorithm can be summarised as follows:

1. Preparation: Definition of an effective, non-Hermitian Hamiltonian $\hat{H}'$ with

$$\hat{H}' = \hat{H} - \frac{i\hbar}{2}\sum_{k}^{K}\hat{C}_k\hat{C}_k^{\dagger} \quad ; \tag{2.25}$$

   where the $\hat{C}_k$ are the Lindblad operators from Eq.(2.11). Specify the initial wave function $|\Psi(0)\rangle$, e.g. as the vibrational ground state wave function $|0_g\rangle$ if the temperature $T = 0$ or $|v_g\rangle$ with probability $w_v(T)$ for finite temperature, where $w_v(T)$ is the Boltzmann weight of state $|v_g\rangle$.

2. Propagation: Generation of N quantum trajectories n. In each time step, the wave packet $|\Psi(t)\rangle$ is propagated according to

$$|\Psi'(t+\Delta t)\rangle = e^{-i/\hbar\hat{H}'\Delta t}|\Psi(t)\rangle \tag{2.26}$$

   to time $t + \Delta t$, giving a perturbed wave packet $|\Psi'(t+\Delta t)\rangle$. Since $\hat{H}'$ is non-Hermitian, there will be a loss of norm δp:

$$\delta p = 1 - \langle\Psi'(t+\Delta t)|\Psi'(t+\Delta t)\rangle \quad . \tag{2.27}$$

   In each time step, a random number $\epsilon \in [0,1]$ is drawn. If $\epsilon \leq \delta p$, a quantum jump occurs, i.e., the wave packet is transfered instantaneously to any of the K modes k defined in Eq. (2.25) with a probability $w_k = \delta p_k/\delta p$. Thereby,

δp_k is the loss of norm due to dissipative channel k. If a jump was made, the new wave packet $|\Psi(t+\Delta t)\rangle$ is taken to be

$$|\Psi(t+\Delta t)\rangle = \frac{\hat{C}_k|\Psi(t)\rangle}{\sqrt{\langle\hat{C}_k|\Psi(t)|\hat{C}_k|\Psi(t)\rangle}} \quad . \tag{2.28}$$

If $\epsilon > \delta p$, no quantum jump occurs and the propagated wave packet is simply renormalised to give $|\Psi(t+\Delta t)\rangle$, which is then used for the propagation to a finite time t_f. This procedure is repeated for many different realisations n and different operator expectation values $\hat{A}$ are obtained from

$$A_n(t) = \langle\Psi_n(t)|\hat{A}|\Psi_n(t)\rangle \quad . \tag{2.29}$$

3. Final analysis: Averaging. After performing N realisations of this type, the final expectation value is obtained by arithmetic averaging:

$$\langle\hat{A}\rangle(t) = \frac{1}{N}\sum_{n}^{N}\hat{A}_n(t) \quad . \tag{2.30}$$

As shown in [55], if $N \to \infty$ and if the dissipation is of Lindblad form, then $\langle\hat{A}\rangle(t)$ obtained via Eq.(2.30) becomes identical to the corresponding quantity obtained via the direct solution of a Liouville - von Neumann equation of Lindblad form. In practice, N is finite and stochastic convergence to the exact result is observed. However, if the results are dominated by statistically rare events, the convergence can be very poor.

2.2.2.2 The Gadzuk "jumping wave packet" method

Gadzuk's "jumping wave packet" method [42] for the treatment of DIET processes is based on a 4-step algorithm and involves two electronic states:

1. vertical excitation of a ground state wave packet from the electronic ground state potential to the excited state at time $t = 0$;

2. propagation of the wave packet in the excited state for a period $0 < t \leq \tau_R$;

3. instantaneous relaxation back to the ground state at τ_R;

4. propagation in the ground state up to a final propagation time t_f.

With $\hat{H}_g$ and $\hat{H}_e$ being the nuclear Hamiltonians of the ground and excited state, an initial wave function $|v_g\rangle$ evolves in time according to:

$$|\Psi(t;\tau_R;v_g)\rangle = e^{-i\hat{H}_g(t-\tau_R)/\hbar}|g\rangle\langle e|e^{-i\hat{H}_e\tau_R/\hbar}|e\rangle\langle g|v_g\rangle \tag{2.31}$$

where $|v_g\rangle$ is a vibrational wave function of the electronically unexcited adsorbate. The "upward operator" $|e\rangle\langle g|$ models the excitation step, which is assumed to be incoherent and sudden, leaving the initial wave function undistorted. After time τ_R, a "downward operator" $|g\rangle\langle e|$ transfers the wave function to $|g\rangle$, where it evolves to some final propagation time t_f. The expectation value of an operator $\hat{A}$ for a single quantum trajectory with a residence time τ_R on the upper surface is obtained as:

$$A(t;\tau_R;v_g) := \langle\Psi(t;\tau_R;v_g)|\hat{A}|\Psi(t;\tau_R;v_g)\rangle \quad . \tag{2.32}$$

Several "excitation-deexcitation" quantum trajectoriesare run according to Eq.(2.31), corresponding to different residence times τ_R and the final expectation values are obtained as a weighted and normalised average over the single realisations:

$$\begin{aligned}\langle\hat{A}\rangle(t;v_g) &= \frac{\int_0^\infty e^{-\tau_R/\tau}A(t;\tau_R;v_g)d\tau_R}{\int_0^\infty e^{-\tau_R/\tau}d\tau_R} \\ &= \int_0^\infty w(\tau_R)A(t;\tau_R;v_g)\,d\tau_R \quad ,\end{aligned} \tag{2.33}$$

where

$$w(\tau_R)d\tau_R = e^{-\tau_R/\tau}d\tau_R/\int_0^\infty e^{-\tau_R/\tau}d\tau_R \tag{2.34}$$

is the probability that the resonance decays between τ_R and $\tau_R + d\tau_R$, and $w(\tau_R)$ is a probability density.

The lifetime τ of a single state is introduced in the Gadzuk algorithm by the weighting factors $w(\tau_R)$ in Eq.(2.33). They represent the survival probability of the excited state and averaging with them results in an exponential decay of the norm

of the nuclear wave packet on the excited state surface. According to Eq.(2.33), the norm on the upper surface develops in time as

$$\langle N_e \rangle(t) = \frac{\int_0^\infty e^{-\tau_R/\tau} \langle \Psi_e(t,\tau_R) | \Psi_e(t,\tau_R) \rangle d\tau_R}{\tau} \tag{2.35}$$

where the integration in the denominator has been performed. Since the square of the norm $\langle \Psi_e(t,\tau_R) | \Psi_e(t,\tau_R) \rangle$ in the excited state is 1 for $t \leq \tau_R$ and 0 for $t > \tau_R$, Eq.(2.35) becomes:

$$\langle N_e \rangle(t) = \frac{\int_t^\infty e^{-\tau_R/\tau} d\tau_R}{\tau} \quad , \tag{2.36}$$

which yields, after integration, the exponential decay

$$\langle N_e \rangle(t) = e^{-t/\tau} \quad . \tag{2.37}$$

In practice, the residence times τ_R can be chosen on a discrete time grid according to $\tau_{Rn} = \tau_{R0} + n\Delta\tau_R$, resulting in a discrete version of Eq.(2.33):

$$\langle \hat{A} \rangle(t) = \sum_{n=1}^{N} w_n A_n(t) \quad , \tag{2.38}$$

where

$$A_n(t) = \langle \Psi(t;\tau_{Rn}) | \hat{A} | \Psi(t;\tau_{Rn}) \rangle \quad , \tag{2.39}$$

and the weighting factor w_n is given by

$$w_n = \frac{e^{-\tau_{Rn}/\tau}}{\sum_{n=1}^{N} e^{-\tau_{Rn}/\tau}} \quad . \tag{2.40}$$

One may also use a non-equidistant residence time grid, $\tau_{Rn} = \tau_{R0} + n\Delta\tau_{Rn}$, in which case the weighting coefficients w_n in Eq.(2.40) have to be replaced by

$$w_n = \frac{e^{-\tau_{Rn}/\tau} \Delta\tau_{Rn}}{\sum_{n=1}^{N} e^{-\tau_{Rn}/\tau} \Delta\tau_{Rn}} \quad . \tag{2.41}$$

As shown in [61, 62], the Gadzuk algorithm is rigorously equivalent to the solution of the Liouville -von Neumann equation (2.10), if the dissipation is of Lindblad form and a DIET process is described in a single-dissipative channel model (deexcitation-only limit) with coordinate-independent quenching. The number N of quantum trajectories one has to compute to obtain converged properties of interest is usually small ($N < 100$) [61], making the Gadzuk method a very efficient alternative in the cases it can be applied.

2.2.2.3 The "generalised Gadzuk method"

An extension of Gadzuk's jumping wave packet method to DIET processes with coordinate-dependent relaxation was developed by Finger and Saalfrank [60]. It presents a simplification of the MCWP method for two possible states and one dissipative channel and is equal to a Gadzuk algorithm with numerically determined weighting coefficients. The strategy is as follows:

1. First, the probabilities for the quantum jumps are determined. For this, the initial wave function is propagated only on the excited state surface to obtain the probability $p(t_m)$ of a quantum jump to occur at time t_m. The wave packet is propagated with the non-Hermitian Hamiltonian $\hat{H}'$ of Eq.(2.25) for all time steps and normalised. At each time step t_i, the loss of norm $\delta p(t_i)$ is calculated. This loss is equal to the probability of a quantum jump Eq.(2.27) in the MCWP method. Thus, the survival probability $p_a(t_m)$, i.e. the probability that no quantum jump occurs until time $t_m = m\delta t$, is given as the product of the survival probabilities at each time step:

$$p_a(t_m) = \prod_{i=1}^{m}(1 - \delta p(t_i)) \quad . \tag{2.42}$$

   The probability $p_b(t_m)$ for a quantum jump to occur at time t_m is given as the product of the probability that the wave packet has survived in the initial state up to time t_{m-1} and the loss of norm at time t_m:

$$p_b(t_m) = p_a(t_{m-1})\delta p(t_m) \quad . \tag{2.43}$$

2. As in the original Gadzuk method, then N quantum trajectories with different residence times τ_{Rn} are computed. For $t < \tau_{Rn}$, the wave packet is propagated again with the non-Hermitian Hamiltonian $\hat{H}'$ of Eq.(2.25) and renormalised in every time step. After time $t = \tau_{Rn}$, a quantum jump to the ground state potential occurs. The following evolution of the wave function obtained in this way (Eq.(2.28)) up to some final propagation time in the ground state is dissipation-free (if vibrational relaxations are neglected).

3. The final expectation values of operators $\hat{A}$ are then computed as the average of those of the N single quantum trajectories n, weighted by the probability of their occurrence and normalised:

$$\langle \hat{A} \rangle(t) = \sum_{n}^{N} w_n \langle \Psi(t; \tau_{Rn}) | \hat{A} | \Psi(t; \tau_{Rn}) \rangle \tag{2.44}$$

where the weighting coefficient w_n is here

$$w_n = \frac{p_b(\tau_{Rn})}{\sum_n^N p_b(\tau_{Rn})} \tag{2.45}$$

As it is shown elsewhere [62], this algorithm converges for $\tau_{R0} = 0$ and $\Delta\tau_R \to \delta t$ towards the ordinary MCWP result, which itself is equivalent to the direct solution of the Liouville -von Neumann equation [55]. It can be shown also that for the special case of coordinate-independent excitation quenching the original version of the Gadzuk scheme with exponential weights is regained [62].

Chapter 3

STM induced desorption of H/D from Si(100)-(2x1)[63, 64]

3.1 General aspects

The scanning tunneling microscope (STM) can not only used for imaging [8, 65] and spectroscopy [66] of bare and adsorbate-covered surfaces, but it is also a very versatile tool for the active manipulation of substrates and adsorbates on an atomic scale.

The STM consists of a sharp metal tip held in close proximity to a conducting substrate by feedback electronics [5]. A bias voltage is applied between the sample and the tip, inducing a coupling between the electronic states of the STM tip and the surface. The exponential dependence of the magnitude of the resulting tunneling current on the tip-sample distance for a fixed voltage difference can be used to compute spatially resolved images of the surface. The imaging can be combined with inducing chemistry, making the STM a very powerful tool for the study of (excited state) surface chemistry.

The miscellaneous possibilities for the modification of adsorbate and surface systems originate in the different mechanistic routes along which the STM can act as

manipulative tool. Strong electric fields (in the order of 1 V/Å) can be achieved with the STM because of the close proximity of the tip to the surface. They are comparable in magnitude to the field that electrons experience in atoms or molecules, thus perturbing chemical bonds. The coupling of the electric field to molecular, permanent or induced (transition) dipoles of the adsorbate can be exploited to enforce molecular motion [67, 68]. When the bias voltage exceeds the work function of the tip (4.5 eV for W), field emission of electrons occurs. Modifications with field-emitted electrons are not confined to atomic dimensions, because the comparably large tip-sample distance (10 - 20 Å) leads to the irradiation of a significantly larger area ($\sim$ 50 - 100 Å^2) and so a less selective modification cross-section. Although atomically resolved modifications on the surface are achievable by exploiting atomic forces or the electric field, control and induction of bond selective chemistry is best achieved with tunneling electrons, where the initial excitation is confined to atomic dimensions $<$ 1Å.

The key feature of the STM is the very large current density which can be obtained in the tunneling junction – up to $\sim 10^{12}$ electrons per second through an area of atomic dimensions. Depending on the energy of the electrons, two important regimes of electron related mechanisms can be distinguished. When the electron energies are larger than a threshold to form a short-lived electronically excited intermediate (resonance) this can lead, for instance, to the breaking of the adsorbate-surface bond. If the electron energy is below the electronic threshold, desorption is still possible through "vibrational ladder climbing" in the electronic ground state (see sections 1.2 and 3.4). The vibrational excitation of the inelastically tunneling electrons can be due to a dipole mechanism, where the field produced by the incident electrons interacts with the transition dipole moment of the vibrational mode. Another excitation channel is via a resonance phenomenon, where incident electrons are temporarily trapped in an unoccupied or partially unoccupied adsorbate level (resonance) [14, 29].

Hydrogen on silicon has long been used as a model system for the study of

chemisorption on semiconductor surfaces [69, 70] and is a system of significant scientific and technological importance. Understanding the adsorption and desorption of hydrogen from silicon is crucial because hydrogen atoms influence the structure, diffusion and chemical reactivity at the surface. Hydrogen is used extensively to chemically and electrically passivate surfaces and interface dangling bonds [3, 71].

3.2 Desorption in the "above threshold" limit

3.2.1 Review of experimental results and previous theoretical treatment

Recent STM desorption experiments on Si(100)-(2x1):H/D by Avouris and co-workers [17, 18, 29, 72, 73] showed desorption to occur with high probability if the electron energy exceeds a threshold of $\sim$ 6 eV. Even if the electron energy is higher, the desorption yield remains nearly constant at $\sim 2.4\times10^{-6}$ atoms per electron and is independent of both voltage and current. While hydrogen and deuterium show the same desorption threshold, a strong isotope effect is observed in the desorption yield, which is about 50 times lower for deuterium. The experimentally observed electronic threshold is consistent with electron energy loss spectra of Si(100) monohydride by Maruno et al. [74] in which a transition with maximum at $\sim$ 8 eV and onset of $\sim$ 6 eV was observed. This was interpreted as the σ(SiH) bonding to σ^*(SiH) anti-bonding transition. Desorption yield and isotope effect for both isotopes were largely unaffected when the surface was cooled from 300K to 11K.

Avouris and co-workers have constructed, based on Multi-Configuration Self-Consistent Field (MCSCF) cluster calculations [29], potential energy curves for the electronic ground and excited states, corresponding to the σ and σ^* states. The excited state has strong repulsive character with a slope in the Franck-Condon region of $\sim$ 6.5 eV/Å. The potentials were used to treat the dynamics of the hydrogen/deuterium abstraction from Si(100) in the "above threshold" regime theoreti-

cally by a Menzel-Gomer-Redhead (MGR) type model (see section 1.4, Fig.1.1) and semiclassical Gaussian wave packet propagation for a surface temperature $T_s = 0$ K [29]. A complex excited state potential was included to account for the electronic quenching process which is assumed to be ultrafast, due to tunneling of the excited electron to empty Si conduction band states.

3.2.2 Open system density matrix approach to the desorption process

In this work, open system density matrix theory is applied as a more rigorous quantum mechanical approach to describe the STM-induced bond breaking dynamics. In addition to the comparison of "exact" quantum dynamical with classical mechanics, the importance of coordinate-dependent resonance decay is addressed and effects of a finite surface temperature are investigated.

As suggested by Avouris and co-workers, a 2 state - 1 mode MGR type model (Fig.1.1) is used to describe the STM induced desorption in the Si(100)-(2x1):H/D system. In the single excitation DIET limit, an initial, singular Franck-Condon type transition from the electronic ground state $|g\rangle$ to the electronically excited state $|e\rangle$ is assumed. The excited adsorbate then evolves on the excited-state potential and at the same time relaxes back to the ground state $|g\rangle$ on an ultrashort timescale (fs). The strongly repulsive excited state and the ultrashort quenching process imply that the desorption will occur via a "hot ground state" mechanism: when enough kinetic energy has accumulated in the excited state to overcome the remaining binding energy in the ground state, desorption occurs. Indeed, for all cases studied below, desorption from the excited state plays no role.

Choosing a dissipative Lindblad ansatz for the treatment of the electron induced DIET within open system density matrix theory (see chapter 2), a Liouville-von Neumann equation of the type

$$\dot{\hat{\rho}}_s(t) = -\frac{i}{\hbar}\left[\hat{H}_s, \hat{\rho}_s\right] + \hat{C}\hat{\rho}_s\hat{C}^\dagger - \frac{1}{2}\left[\hat{C}^\dagger\hat{C}, \hat{\rho}_s\right]_+ \quad , \tag{3.1}$$

has to be solved. Just one Lindblad operator $\hat{C}$ is considered, counting for electronic energy relaxation as the only dissipative channel. Other dissipative channels, such as pure electronic dephasing or vibrational energy relaxation are not included. In the Lindblad DIET model used here, no direct (Hamiltonian) couplings are assumed, i.e., the time evolution of the coherences $\hat{\rho}_s^{eg}$ and $\hat{\rho}_s^{ge}$ are decoupled from the diagonal blocks of the density matrix. Thus, pure electronic dephasing cannot play any role in this model. Also, vibrational energy relaxation of the SiH bond –which is known to proceed on the nanosecond time scale [75]– is neglected here, because it is long on the time scale of the bond breaking, which takes place in less than a picosecond (see below).

The system Hamiltonian $\hat{H}_s$ in Eq.(3.1), which accounts for the Hamiltonian evolution of the isolated system, is taken to be

$$\hat{H}_s = \hat{H}_g|g\rangle\langle g| + \hat{H}_e|e\rangle\langle e| \quad , \tag{3.2}$$

and the density operator can be written as

$$\hat{\rho}_s = \hat{\rho}_s^e|e\rangle\langle e| + \hat{\rho}_s^g|g\rangle\langle g| + \hat{\rho}_s^{eg}|e\rangle\langle g| + \hat{\rho}_s^{ge}|g\rangle\langle e| \quad . \tag{3.3}$$

The Hamiltonians for the two electronic states considered, $\hat{H}_l$ $(l = g, e)$, are given in a one-mode model by

$$\hat{H}_l = -\frac{\hbar^2}{2m}\frac{d^2}{dZ^2} + V_l(Z) \quad , \tag{3.4}$$

where Z is the displacement of the adsorbed atom from its ground state equilibrium position, and m the mass of the hydrogen isotope under investigation. For the ground and excited state potential curves, a Morse function

$$V_g(Z) = D \cdot [1 - e^{-\alpha z}]^2 - D \quad , \tag{3.5}$$

and a simple exponential are used,

$$V_e(Z) = A \cdot e^{-\beta z} \tag{3.6}$$

respectively (see Fig.3.1). The potential parameters are based on the ab initio cluster calculations of Avouris (see above) and are given in Table 3.1.

Eq. (3.1) is solved subject to the initial condition

$$\hat{\rho}_s(0) = |e\rangle\langle e| \otimes \sum_v w_v(T_s)|v_g\rangle\langle v_g| \quad , \tag{3.7}$$

where $|v_g\rangle$ is the v-th vibrational wave function in the electronic ground state ($\hat{H}_g|v_g\rangle = \varepsilon_{vg}|v_g\rangle$) and

$$w_v = e^{-(\varepsilon_{vg}-\varepsilon_{0g})/k_BT_s} / \sum_v e^{-(\varepsilon_{vg}-\varepsilon_{0g})/k_BT_s} \tag{3.8}$$

is the Boltzmann weight of state $|v_g\rangle$ at surface temperature T_s.

By Eq.(3.7), an incoherent, sudden Franck-Condon transition of the ground state thermal ensemble to the electronic excited state is enforced, serving as a crude model for the STM–induced excitation process. The Lindblad operator $\hat{C}$ accounting for the electronic energy relaxation is taken to be

$$\hat{C} = \sqrt{\Gamma_{ge}(Z)}|g\rangle\langle e| \quad , \tag{3.9}$$

where $\Gamma_{ge}(Z)$ is the coordinate-dependent rate for the decay of the excited state resonance. To consider the fact that the electronic quenching proceeds faster at smaller adsorbate-surface distances and is very unlikely to happen at larger Z, an exponential ansatz for Γ_{ge} is chosen:

$$\Gamma_{ge} = \Gamma_0 \cdot e^{-\gamma z} \quad . \tag{3.10}$$

Since a dissociative continuum has to be dealt with, Eq.(3.1) was solved by representing all operators on a discrete coordinate grid. The Fast Fourier Transform (FFT) algorithm was used to evaluate the kinetic energy commutator locally in momentum space [34], and the time-evolution superoperator was approximated by a Newton polynomial expansion (see section 2.2.1). The propagation parameters for this "direct" (i.e., density *matrix* propagation) approach are also given in Table 3.1.

Additionally, the more economic "indirect", wave packet-based method of Gadzuk (see section 2.2.2.2) was used for the DIET process with coordinate-independent quenching ($\Gamma_{ge}(Z) := \Gamma_0 = \text{const.}$ in Eq.(3.10)). An initial wave function $|v_g\rangle$, here the vibrational SiH eigenstates, was propagated according to Eq.(2.31) and the final observables of interest were then obtained using Eq.(2.38).

The generalized Gadzuk method (section 2.2.2.3) was used for the treatment of coordinate-dependent quenching. In both the "jumping wave packet" methods, the surface temperature effects were introduced through a second, incoherent averaging scheme according to

$$\langle \hat{A} \rangle(t; T_s) = \sum_v w_v(T_s) \cdot \langle \hat{A} \rangle(t; v_g) \quad , \tag{3.11}$$

where the w_v are the Boltzmann weights Eq.(3.8) introduced above.

The solution of Eq.(2.31) was accomplished by representing the wave functions on a discrete coordinate grid and by using the Fast Fourier Transform method to evaluate the kinetic energy operator [76]. The split-operator propagator of Feit and Fleck [77] was used for the wave packet propagation (see also appendix A). All computational parameters for the wave packet based treatment are also given in Table 3.1.

Potential parameters	
Ground state potential	
Morse well depth	$D = 0.11724$ $E_h = 3.2$ eV
Morse well location at	$Z = 0$
Morse exponent	$\alpha = 0.8123$ a_0^{-1}
Excited state potential	
Exponential prefactor	$A = 0.15326$ $E_h = 4.2$ eV
Exponential range parameter	$\beta = 0.693$ a_0^{-1}
Propagation parameters (Gadzuk Method)	
Grid parameters	
Grid spacings (Gadzuk method)	$\Delta_Z = 0.09$ a_0 (for H)
	$\Delta_Z = 0.065$ a_0 (for D)
Grid spacings (direct method)	$\Delta_Z = 0.09$ a_0 (for H and D)
Nb. of grid points (Gadzuk method)	$N_Z = 1024$
Nb. of grid points (direct method)	$N_Z = 512$
Grid starts at	$Z_a = -2.872$ a_0
Wave packet considered desorbed for	$Z_{des} > 8.3$ a_0
Split operator propagation parameters	
Time step	$\Delta t = 2.42 \times 10^{-3}$ fs
Total propagation time	$t_f = 125$ fs
Newton interpolation propagation parameters	
Time step	$\Delta t = 2.5$ fs
Total propagation time	$t_f = 125$ fs
Polynomial order	$M = 16$
Lifetime averaging parameters	
"Residence time grid" starts at	$\tau_{R0} = 0.1$ fs
"Residence time grid" spacing	$\Delta_R = 0.1$ fs (for $\tau_R \leq 1$ fs)
	$\Delta_R = 0.5$ fs (for $\tau_R > 1$ fs
Number of residence times considered	$N = 32$

Table 3.1: *STM-induced DIET on Si(100)-(2×1):H(D): Numerical parameters for the potentials, for wave packet propagation and analysis, using the "jumping wave packet" algorithm and for the direct density matrix propagation.*

3.2.3 Desorption with coordinate-independent electronic quenching

In a first approach, it was assumed that the electronic decay rate is coordinate-independent ($\gamma = 0$ in Eq.(3.10)) and that the substrate temperature $T_s = 0$ [63].

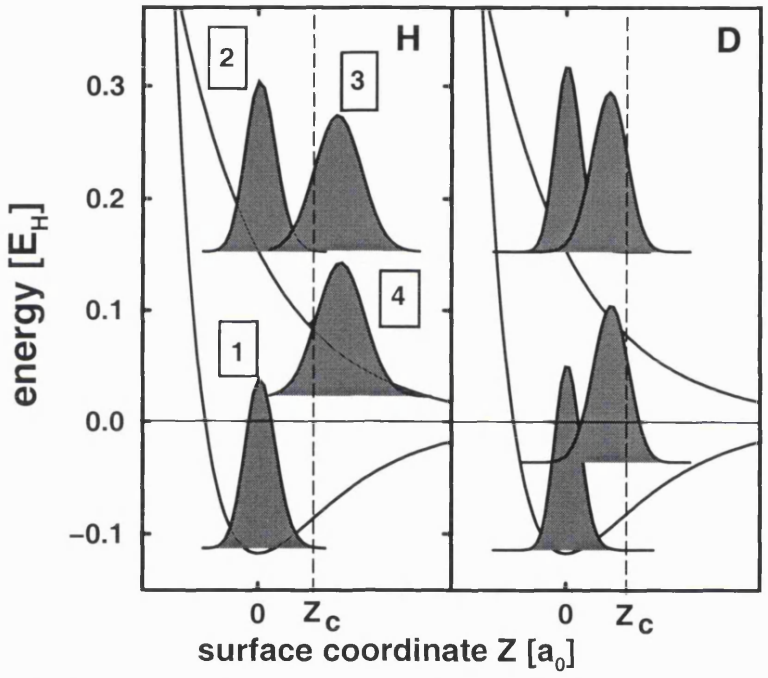

Figure 3.1: *STM-induced DIET of H and D from Si(100)-(2x1):H/D. Representation of the ground and excited state potentials for H(D)/Si(100) with "snapshots" of the single quantum trajectory wave packets* $|\psi(t;\tau_R;v_g)\rangle$ *(left for H, right for D) when the residence time* τ_R *is 5.5 fs and* $v_g = 0$. Z_c *denotes the critical distance, which a classical particle must reach to desorb. As explained in the text, the major part of the H wave packet will desorb after return from the excited state, while D will be dominantly retrapped.*

In Fig.3.1, the potential energy curves are shown and the desorption process within Gadzuk's jumping scenario is illustrated via "snapshots" of the wave packets,

for the cases of Si:H (left panel) and Si:D (right panel) and a residence time τ_R of 5.5 fs. The four wave packets in each panel correspond to the initial wave packet before (1) and immediately after electronic excitation (2), and to the propagated wave packet immediately before (3) and after (4) the sudden quenching process occurring at τ_R. The baselines of the wavefunctions are chosen to be equal to their total energies. It is seen that after electronic relaxation, the hydrogen wave packet moves further outward and has finally a positive energy. In contrast, the more inertial deuterium wave packet travels less far in the same time and its final average energy is negative. As a consequence, most part of the H wave packet will desorb, while the D wave packet will be mainly retrapped, which qualitatively explains the strong isotope effect observed in the experiments.

The wave packet propagations up to some final time t_f are repeated for different residence times τ_R. It is found that the entire "reaction" proceeds on the sub-ps timescale and a choice $t_f = 125$ fs is sufficient.

The obtained desorption probability $P_{des}(\tau_R)$ is shown for a quantum trajectory with residence time $\tau_r = 5.5$ fs in Fig.3.2 for hydrogen (full line) and deuterium (dashed line). It can be seen that for hydrogen $P_{des}(\tau_R)$ increases continuously from 0 to 1, with a quantum "critical residence time" τ_{Rc}^q (for which $P_{des}(\tau_R) = 0.5$) of $\tau_{Rc}^q \approx 4.8$ fs. Qualitatively, the same is observed for deuterium for which, however, $\tau_{Rc}^q \approx 7.0$ fs. For the situation studied in Fig.3.1 with $\tau_R = 5.5$ fs, a high desorption probability for hydrogen is found indeed ($P_{des}(\tau_R) = 0.79$), while D is dominantly retrapped ($P_{des}(\tau_R) = 0.05$). Additionally, (approximate) classical step curves are shown in Fig.3.2, with zero desorption probability for $\tau_R < \tau_{Rc}$ and unit probability for $\tau_R > \tau_{Rc}$:

$$P_{des}(\tau_R) = h(\tau_R - \tau_{Rc}) \tag{3.12}$$

with $h(x) := 1$ for $x > 0$ and 0 otherwise. τ_{Rc} is the time required for a classical atom of mass m to reach the critical distance Z_c on the excited potential, at which the kinetic energy gained equals the remaining binding energy in the ground state.

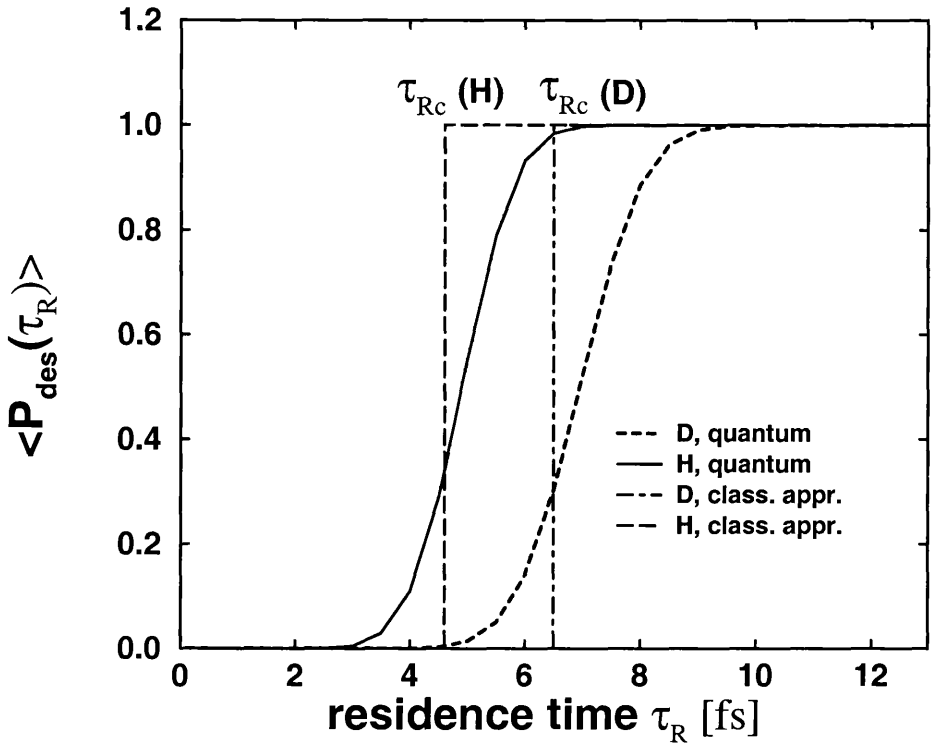

Figure 3.2: *Desorption probability $P_{des}(\tau_R)$ for H and D in STM-induced DIET from Si(100)-(2x1):H/D as a function of residence time on the excited state, τ_R, assuming a coordinate-independent quenching process and $T_s = 0$ K. The step functions are approximate classical results, while the smooth curves are the quantum results obtained by the Gadzuk algorithm.*

With the potentials Eq.(3.5) and Eq.(3.6), the critical distance Z_c is given by

$$A(1 - e^{-\beta Z_c}) = D - D(1 - e^{-\alpha Z_c})^2 \quad . \tag{3.13}$$

On the left hand side of the equation is the amount of kinetic energy gained on V_e at $Z = Z_c$ and on the right hand side is the corresponding remaining ground state binding energy. The solution of Eq.(3.13) gives $Z_c = 1.045$ a_0, as it is indicated in Fig.3.1 as vertical line. One sees that after relaxation the centre-of-gravity of the H wave packet is at a distance larger than the critical distance Z_c, while for the deuterium wave packet $Z < Z_c$ is found. This finding implies that the quantum wave packet also has to pass Z_c to obtain a high desorption yield.

The critical time τ_{Rc} a classical particle has to remain on the upper surface to reach Z_c and desorb can be determined by numerical integration of the classical equations of motion. Alternatively, an approximate classical result (the one used above) can be obtained analytically by assuming that the force and hence the acceleration of a classical particle in the excited state is constant in time. Assuming that this force is given by the gradient of the excited state potential at the "Franck–Condon point" ($Z = 0$), the acceleration is given by

$$a = -\frac{1}{m}\frac{dV_e}{dz}|_{z=0} = \frac{\beta A}{m} \quad . \tag{3.14}$$

It follows for the particle velocity

$$v = \int_0^t a dt' = \frac{\beta A}{m} t \quad , \tag{3.15}$$

and thus for the critical distance

$$Z_c = \int_0^{\tau_{Rc}} v dt = \frac{\beta A}{2m} \tau_{Rc}^2 \quad , \tag{3.16}$$

which implies

$$\tau_{Rc} = \sqrt{\frac{2mZ_c}{\beta A}} \quad . \tag{3.17}$$

With Eq.(3.17), one obtains $\tau_{Rc}(H) = 4.6$ fs and $\tau_{Rc}(D) = 6.5$ fs. The ratio of the residence times, $\tau_{Rc}(H)/\tau_{Rc}(D)$ correlates to the mass relation of the two isotopes $\sqrt{m_H/m_D} = \sqrt{2}$. This is in reasonable agreement with the quantum "critical residence times" τ_{Rc}^q and also with the exact, classical critical residence times obtained by numerical integration of the classical equations of motion, which are $\tau_{Rc}(H) = 4.7$ fs and $\tau_{Rc}(D) = 6.8$ fs.

As shown in Fig.3.1, the main quantum effect is the broadening of the $P_{des}(\tau_R)$ curves which arises from the finite extension of the quantum wave packet both in position and momentum space. Further, the assumption of a constant force in the excited state is a good one, which allows for insightful, though approximate, analytical classical treatment of the desorption process.

To account for the continuous, exponential resonance decay and to obtain the "true" desorption probability $\langle P_{des} \rangle(\tau, v_g)$ at $T_s = 0$ K, the average of the desorption probabilities $P_{des}(\tau_R)$ obtained for each quantum trajectory has to be evaluated according to Eq.(2.33) with the "true" lifetime τ of the excited state. Defining the isotope effect in the desorption probability as

$$I_{des}(v_g) = \frac{\langle P_{des} \rangle(H; v_g)}{\langle P_{des} \rangle(D; v_g)} \quad , \tag{3.18}$$

a lifetime dependence of I_{des} is finally obtained as shown in Fig.3.3 for $v_g = 0$, corresponding to a surface temperature $T_s = 0$ K. The isotope effect as a function

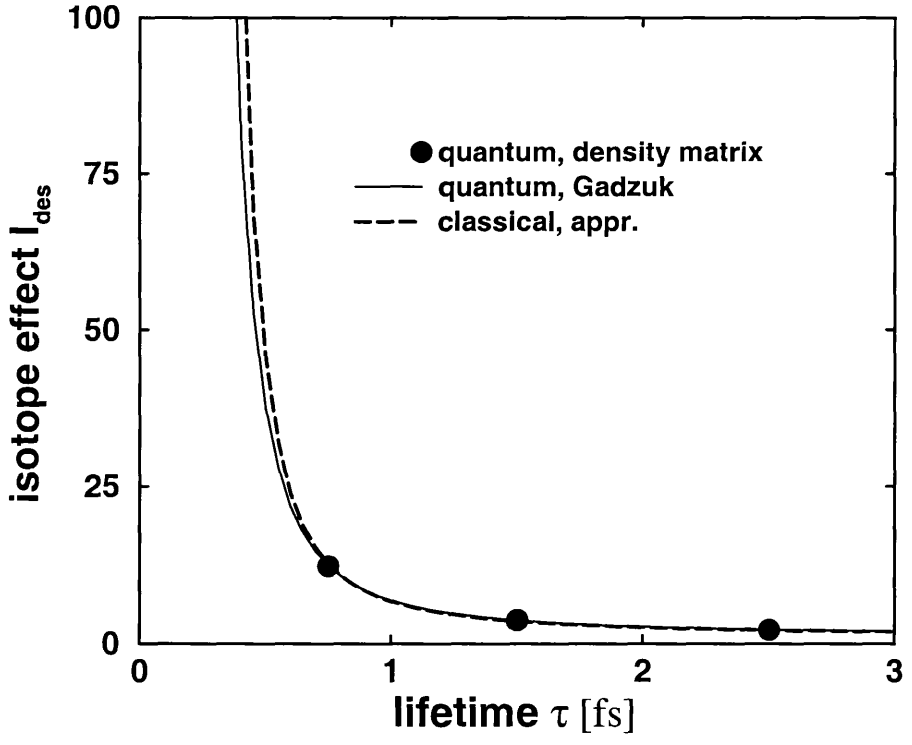

Figure 3.3: *Isotope effect I_{des} in the desorption probability of STM-induced DIET of H and D from Si(100)-(2×1) as a function of the excited state lifetime τ for T_s = 0 K and a coordinate-independent quenching process. The solid line represents the results obtained with Gadzuk's method, while the dashed line is for the classical result. Selected results obtained by direct density matrix propagation are shown as bullets.*

of the lifetime τ behaves asymptotically as $\lim_{\tau\to 0} I_{des} = +\infty$ and $\lim_{\tau\to\infty} I_{des} = 1$. For only large enough τ, both the desorption probabilities of H and D will become 1 and so I_{des} also becomes 1. At short lifetimes, the averaged desorption probabilities decrease, and the decrease for the heavier isotope is faster for the reasons discussed above. The experimentally observed isotope ratio of $\approx$ 50 is consistent with a lifetime of the excited state of $\tau = 1/\Gamma_0 \approx 0.45$ fs, which is in good agreement with the semiclassical estimate of Avouris et al. [29]. The absolute values of the desorption probability are also consistent both with the experimental yield [18] and the semiclassical theory [29]: For $\tau = 0.45$ fs, one obtains $\langle P_{des}\rangle(H; v_g = 0) = 9.90$ x 10^{-5} and $\langle P_{des}\rangle(D; v_g = 0)$ =1.88 x 10^{-6}, respectively.

The bullets in Fig.3.3 represent the results obtained by direct density matrix propagation. The perfect agreement between these results and those obtained by the "jumping wave" algorithm not only gives confidence in the numerical procedures, but also demonstrates once again the equivalence between the two approaches. Also shown in Fig.3.3 is the isotope effect obtained by the approximate classical calculations (dashed line). The classical picture allows for an easy understanding of the isotope ratio. With the step function Eq.(3.12), the integral Eq.(2.33) is given analytically as

$$\langle P_{des}\rangle(v_g = 0; \tau) = e^{-\tau_{Rc}/\tau} \quad . \tag{3.19}$$

Making the additional approximation of a constant force acting on the particle in the exciting state (Eq.(3.17)), the isotope effect now becomes

$$I_{des}(v_g = 0) = e^{-\frac{1}{\tau}\sqrt{\frac{2Z_c}{\beta A}}(\sqrt{\mu_H}-\sqrt{\mu_D})} \quad , \tag{3.20}$$

implying an exponential decrease of the isotope effect with increasing lifetime τ. Further, the steeper the excited state potential at the "Franck–Condon point" $Z = 0$, i.e., the larger βA, the smaller is the expected isotope effect.

The approximate classical curve (Eq.(3.20)) agrees well with the quantum results over the entire interval shown in Fig.3.3. The absolute values for the (averaged) desorption probability at a given τ agree up to $\tau = 3$ fs to within 2% for hydrogen and

within better than 1 % for deuterium with the classical approximations Eq.(3.19) and Eq.(3.17). The surprisingly good agreement between quantum and classical results can be understood from an observation of Brenig and coworkers [78], who showed that the leading corrections to the classical path of a particle moving in a complex potential involve the first derivative of its imaginary part. For coordinate–independent quenching the first derivative is zero and hence quantum effects are expected to be small. However, for the treatment of a coordinate-dependent decay process (see section 3.2.4), a quantum treatment is clearly more appropriate.

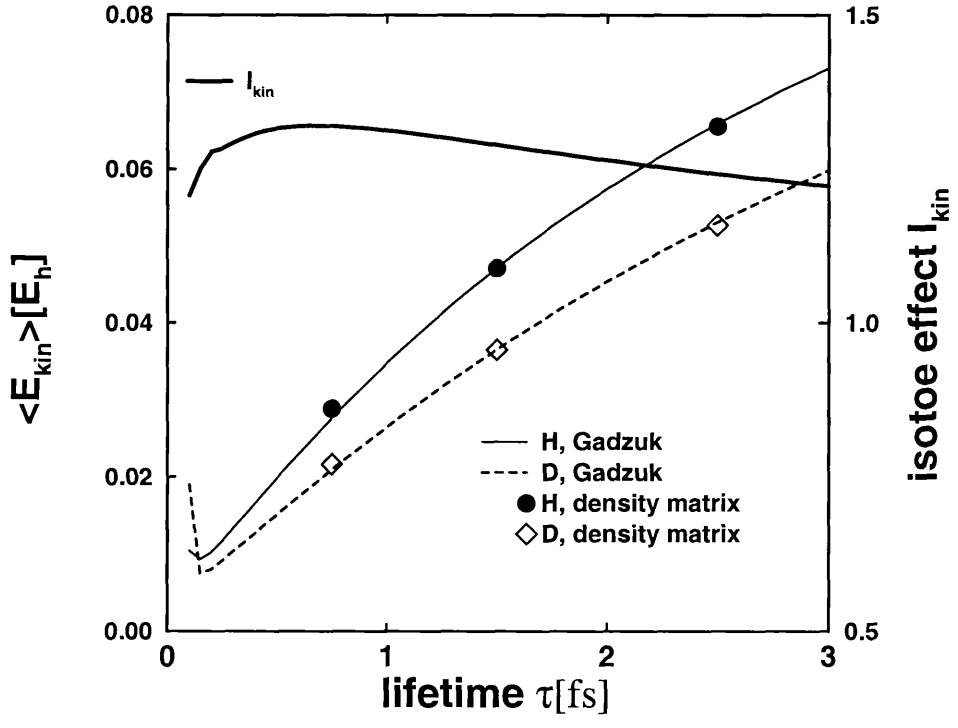

Figure 3.4: *STM-induced DIET of H and D from Si(100)-(2× 1):H/D. Averaged kinetic energies* $\langle E_{kin} \rangle$ *of desorbing H and D atoms, as a function of the excited state lifetime* τ *(left scale). Both the wave packet ("Gadzuk") and direct density matrix results (bullets and diamonds) are shown. The thick, solid curve (right scale) gives the isotope effect in the kinetic energies,* I_{kin}*. Again, coordinate-independent electronic quenching and* $T_s = 0$ *K is assumed. The values at* $\tau < 0.2$ *fs are numerically unsafe.*

Shown in Fig.3.4 is the (averaged) kinetic energy per desorbed hydrogen (solid line) and deuterium (dashed line). For both isotopes, $\langle E_{kin} \rangle$ increases monotonically with the lifetime τ. Eventually, for $\tau \rightarrow \infty$, all particles desorb and their kinetic energies will approach approximately the limit $A = 0.15326\ E_H$, i.e., the potential energy after the initial Franck-Condon excitation. A small isotope effect in the kinetic energy per desorbing atom

$$I_{kin}(v_g = 0) = \frac{\langle E_{kin} \rangle (H; v_g = 0)}{\langle E_{kin} \rangle (D; v_g = 0)} \quad , \tag{3.21}$$

is predicted, but was not observed experimentally so far. For smaller τ, an isotope effect > 1 is expected, while for $\tau \rightarrow \infty$ the isotope ratio (3.21) will be 1 for reasons discussed above. $I_{kin} > 1$ corresponds to faster H atoms, in agreement with the expectations from the MGR model. However, over the range of Fig.3.4 (up to $\tau = 3$ fs), the isotope effect is small (≈ 1.3) and varies only slowly with τ. Also shown in Fig. 3.4 are a few kinetic energies obtained with the direct density matrix scheme (represented by bullets and diamonds).

3.2.4 The effects of coordinate-dependent electronic relaxation

The effects of a coordinate-dependent electronic decay have been examined with the generalized Gadzuk method (see section 2.2.2.3) and some selected direct density matrix calculations [63]. So far, a strictly exponential resonance decay has been considered. Now, a range parameter $\gamma > 0$ is allowed for the rate Γ_{eg}, Eq.(3.10).

First, the range γ is varied, while Γ_0 is fixed at $\Gamma_0 = 1/0.45$ fs^{-1}. Since, in this way, the same local quenching rate at $Z = 0$ is chosen, the resonance decay is quasi-exponential in all cases, with an approximately equal lifetime of $\approx 1/\Gamma_0 = 0.45$ fs. The results for the absolute desorption probability $\langle P_{des} \rangle (\tau, v_g = 0)$ and the corresponding isotope effect I_{des} are given in the upper half of Table 3.2. For $\gamma = 0$, the results are discussed in section 3.2.3 above.

Γ_0	range parameter γ	isotope	$\langle P_{des} \rangle$	I_{des}
$1/0.45$ fs^{-1}	0.0 a_0^{-1}	H	$9.90 \cdot 10^{-5}$	
		D	$1.88 \cdot 10^{-6}$	52.2
$1/0.45$ fs^{-1}	0.5 a_0^{-1}	H	$4.26 \cdot 10^{-4}$	
		D	$1.46 \cdot 10^{-5}$	29.3
$1/0.45$ fs^{-1}	1.0 a_0^{-1}	H	$1.41 \cdot 10^{-3}$	
		D	$9.65 \cdot 10^{-5}$	14.7
$1/0.45$ fs^{-1}	2.0 a_0^{-1}	H	$3.06 \cdot 10^{-3}$	
		D	$5.86 \cdot 10^{-4}$	5.2
$1/0.35$ fs^{-1}	1.0 a_0^{-1}	H	$3.30 \cdot 10^{-4}$	
		D	$1.13 \cdot 10^{-5}$	29.2
$1/0.29$ fs^{-1}	1.0 a_0^{-1}	H	$9.35 \cdot 10^{-5}$	
		D	$1.78 \cdot 10^{-6}$	52.5

Table 3.2: *Influence of coordinate-depending electronic decay on the desorption probability of H and D from Si(100).*

For finite γ, it is found that the absolute desorption probabilities increase both for H and D, by factors of up to 300. This is associated with the fact that in the MGR scenario those parts of the excited wave packet have the best chance to desorb which are initially at larger Z, while those parts closer to the surface are retrapped more easily. Coordinate-dependent relaxation leads to less efficient electronic quenching at larger adsorbate-surface distances Z, as sketched in Fig.3.5. So, if $\gamma > 0$, the large–Z wing of the wave packet moving *outward* will desorb with even enhanced probability. The effect is the larger the larger γ is, i.e., the faster $\Gamma(Z)$ falls off. In

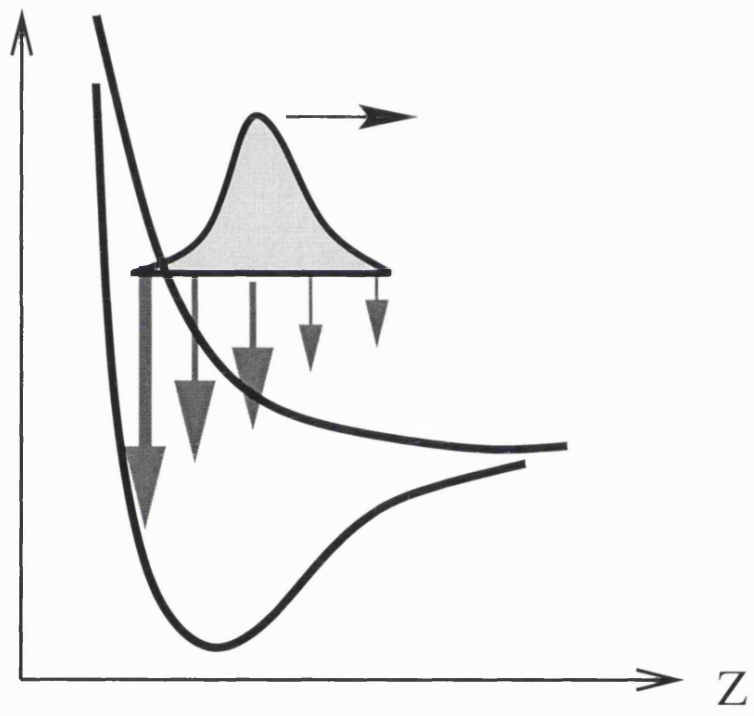

Figure 3.5: *Coordinate-dependent electronic quenching in the MGR model. Coordinate-dependent relaxation leads to less efficient electronic relaxation at larger adsorbate-surface distances Z and thus large Z wing of the wave packet moving* outward *will desorb with higher probability.*

a simple tight–binding model, Γ should depend approximately quadratically on the hopping integral between the adsorbate acceptor orbital and the substrate orbitals

[78, 79], while $V_e(Z)$ depends approximately linear on this integral [78]. Therefore, one can expect roughly $\gamma = 2\beta \approx 1.4$ a_0 in the present case, which is well in the range considered.

It is seen from Table 3.2 that the isotope effect in the desorption probability decreases with increasing γ. This is because the increase of the deuterium desorption probability is faster than the increase of the H probability. Therefore, a slightly smaller lifetime τ corresponding to a higher pre-factor Γ_0 was chosen for finite γ to reproduce the experimentally observed isotope effect. In the lower half of Table 3.2 the results for the variation of Γ_0 at fixed $\gamma = 1.0\,a_0$ are shown. With this choice for the range parameter the computed isotope effect in the desorption yield becomes ≈ 52 for $\Gamma_0 = 1/0.29$ fs^{-1}, again in agreement with experiment and previous semiclassical work [29].

3.2.5 Surface temperature effects

For the study of finite temperature effects, thermal averaging of individual wave packet runs were carried out according to Eq.(3.11). Both coordinate-independent electronic quenching ($\gamma = 0$ a_0^{-1}, $\Gamma_0 = 1/0.45$ fs^{-1}) and coordinate-dependent energy relaxation ($\gamma = 1$ a_0^{-1}, $\Gamma_0 = 1/0.29$ fs^{-1}) were considered, because these parameters produce the experimentally observed isotope effect of ≈ 52 at $T_s = 0$ K (see Table 3.2). The thermal averaging (3.11) was done for up to $T_s = 1000$ K, for which the inclusion of the first seven vibrational levels of the SiH(D)- system proved to be sufficient.

Considering the desorption probability $P_{des}(\tau_R; v_g)$ as a function of the residence time τ_R in the electronically excited state and the initial vibrational quantum number v_g, it can be seen that for $v_g > 0$ the curves are broadened with a distinctive step-like structure. This is demonstrated in the upper panel of Fig.3.6 for deuterium and a coordinate-independent quenching rate. The number of steps in each curve is equal to v_g. By taking the derivative of $P_{des}(\tau_R)$ with respect to τ_R (lower panel of

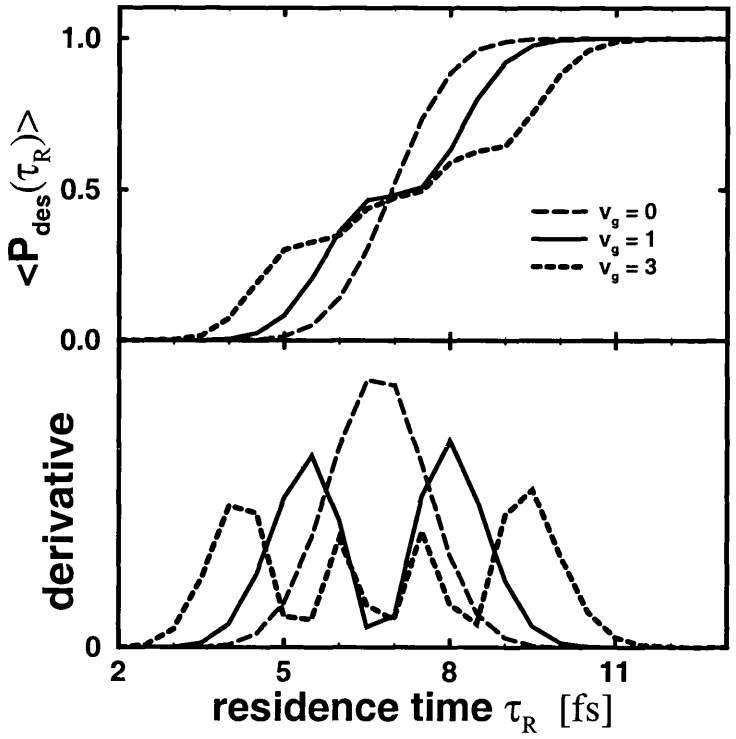

Figure 3.6: *The desorption probability $P_{des}(\tau_R)$ for D as a function of residence time τ_R in the excited state, for initial states, $|v_g\rangle = |0_g\rangle, |1_g\rangle, |3_g\rangle$ is demonstrated in the upper panel. In the lower panel, the derivatives of the $P_{des}(\tau_R; v_g)$ curves with respect to τ_R are shown on an arbitrary scale. They reflect the nodal structure of the initial vibrational wave functions (see text). A coordinate–independent lifetime of $\tau = 0.45$ fs is assumed.*

Fig.3.6), a "desorption rate" as a function of τ_R can be computed. It is found that the individual steps correspond to the individual wave packet lobes, which make up the vibrational wave functions. With increasing τ_R, successively the first, the second, third ... lobe of the wave function reaches the critical distance Z_c and "desorbs" (see also Fig.3.1).

Since for small τ_R the desorption probability appears to increase with increasing v_g, it is expected that vibrational excitation, e.g. by temperature, should lead to enhanced desorption probabilities. This is exactly in keeping with observations made and explanations given in the early days of DIET [80]. In Fig.3.7 the desorption

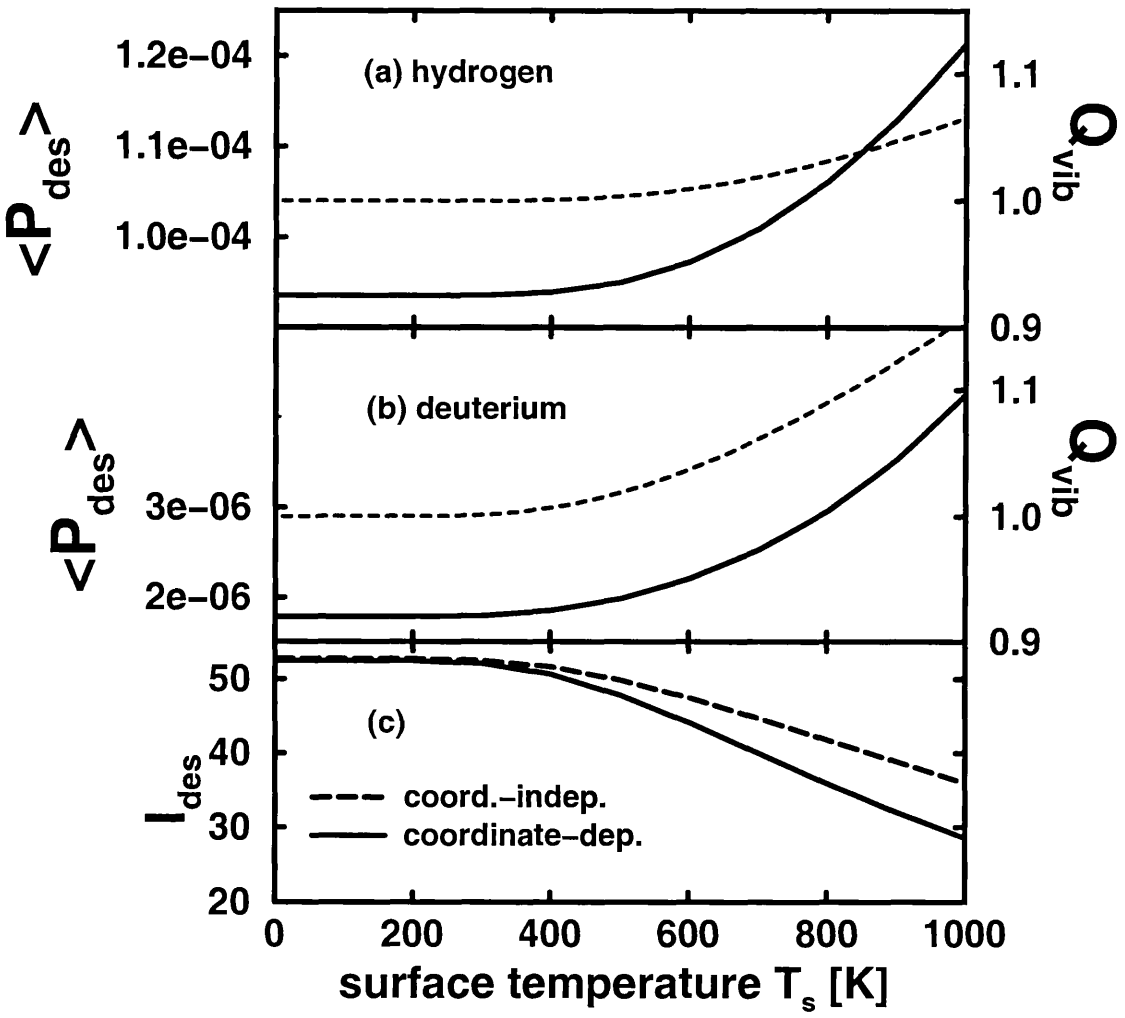

Figure 3.7: *Dependence of the desorption probability of H and D from Si(100) on the surface temperature T_s. In (a) and (b) the (averaged) desorption probabilities $\langle P_{des} \rangle$ are shown for H and D as solid curves (left scale) for an assumed coordinate-dependent quenching process ($\Gamma_0 = 1/0.29$ fs^{-1}, $\gamma = 1.0$ a_0^{-1}). Also given are the vibrational partition functions Q_{vib} as dashed curves (right scale). The isotope effect in the desorption yield, I_{des}, is shown in panel (c). The solid curve is for coordinate-dependent quenching, the dashed one for coordinate-independent quenching (with $\Gamma_0 = 1/0.45$ fs^{-1}, $\gamma = 0$).*

probabilities $\langle P_{des} \rangle$ for H (Fig.3.7(a), left scale, solid line) and D (Fig.3.7(b), left scale, solid line) for coordinate-dependent relaxation are shown as a function of the surface temperature T_s. The isotope effect in the desorption probability is presented, both for coordinate-independent (dashed line) and for coordinate-dependent decay (solid line), in Fig.3.7(c). From Fig.3.7(a),(b) it can be seen that the desorption probability of both isotopes is almost independent of the substrate temperature T_s up to $\approx$ 300K. Only beyond this temperature, the expected increase of $\langle P_{des} \rangle (T_s)$ sets in. This can be understood by considering the vibrational partition functions

$$Q_{vib} = \sum_v e^{-(\varepsilon_{vg} - \varepsilon_{0g})/k_B T_s} \tag{3.22}$$

(dashed lines, right scales in Fig.3.7(a),(b)), which are a measure for the number of vibrational states populated at temperature T_s. It is seen that the partition functions follow closely the computed desorption probabilities. Because of the large vibrational level spacing of the SiH bond ($\hbar\omega \approx 0.25$ eV) and SiD ($\hbar\omega \approx 0.18$ eV), only the vibrational ground state is significantly populated at low temperatures. Thus, the partition functions remain almost constant at $Q_{vib} \approx 1$. As soon as higher levels are significantly populated, however, this immediately translates into higher desorption yields because the $\langle P_{des} \rangle (v_g)$ entering Eq.(3.11) increase rapidly with increasing v_g. For hydrogen and coordinate-depending energy relaxation, for example, it is found

$$\langle P_{des} \rangle (0) = 9.35 \cdot 10^{-5}, \quad \langle P_{des} \rangle (1) = 4.64 \cdot 10^{-4},$$
$$\langle P_{des} \rangle (2) = 1.39 \cdot 10^{-3}, \quad \langle P_{des} \rangle (3) = 3.20 \cdot 10^{-3}.$$

Closer inspection shows that the partition functions exceed the value $Q_{vib} = 1.001$ only above $T_s = 405$ K (H) and $T_s = 285$ K (D). These temperatures can be taken as a crude measure for the width of the plateau region above which the desorption yields increase significantly. The ratio of the "critical temperatures" is $405/285 \approx \sqrt{2}$, sensibly reflecting the ratio of the fundamental frequencies for SiH and SiD.

As a consequence of the weak temperature dependence of the desorption probability, the isotope effect in $\langle P_{des} \rangle$ also appears to be approximately constant up to

$T_s \approx 300$ K (see Fig.3.7c). This statement holds for coordinate-dependent electronic quenching as well as for coordinate-independent relaxation. These observations are in good agreement with the experimental results of Foley at al. [72], who found no temperature dependence of the desorption yield or isotope effect for DIET in the temperature interval between 11 K and 300 K.

However, no corresponding experiments at $T_s > 300$ K have so far been reported. The theoretical results suggest that at temperatures above 300 K, the expected increase in the desorption yields for both isotopes should become observable (see Fig.3.7(a),(b)). Since the vibrational quantum for the SiD vibration is smaller than that for SiH, the relative increase of the desorption probability with temperature is larger for deuterium than for hydrogen. As a consequence, the isotope effect in the yields must eventually decrease with increasing T_s. The theoretical model predicts this to be the case slightly above $T_s \approx 300$ K (see Fig.3.7(c)). For $T_s = 1000$ K, for example, the isotope effect is expected to decrease by about 30 - 50 %, depending on the choice of γ. It should be possible, to observe this reduction experimentally, although thermal desorption also plays a role at higher surface temperatures.

3.2.6 STM-induced desorption at negative sample bias

In the previous discussion, only STM experiments in which the desorption was induced at positive sample bias, i.e., where electrons are travelling from the STM tip to the sample, were considered. Recently, Stokbro et al. desorbed hydrogen from a Si(100) surface at *negative* sample bias [30]. There have been theoretical predictions that mechanisms related to the ones at positive sample bias may operate at negative bias as well [81], where a tunneling hole travels from tip to sample, rather than an electron.

The experiments at negative sample bias show a distinctive suppression of the desorption yield after heating the surface from 300 K to 610 K [30, 82]. In contrast to the experiments at positive sample bias, a DIMET like scaling of the desorption

yield with the current ($\sim I^n$ with $n \approx 6$) was observed for all voltages. Stokbro and co-workers modelled the desorption process by assuming the vibrational heating of hydrogen caused by inelastic scattering of tunneling holes with the SiH 5σ hole resonance [30], i.e. the desorption follows the "below threshold" mechanism (see section 1.2. To investigate the temperature dependence of the desorption yield, two temperature effects were included. Both are based on the T_s dependence of the lifetime of electronic and vibrational excitations, respectively. Stokbro at al. found that up to a sample bias of - 5 V the temperature dependence of the desorption yield is related to the lifetime of the vibrational excitation, which is similar to the results reported by Foley et al. [72] for positive sample bias in the "below threshold" regime (see also section 3.4). However, at higher negative bias, the T_s dependence of the yield is too weak to explain the experimental data and the temperature dependence is dominated by the lifetime τ of the 5σ hole resonance. According to the model of Stokbro et al., the decrease of the electronic lifetime τ with increasing T_s is due to the enhanced coupling of the 5σ hole resonance to both the electrons and the phonons of the silicon substrate.

It was found in the previous section 3.2.5 that the desorption probability in the "above threshold" limit at positive sample bias increases with increasing surface temperature T_s because of the "Boltzmann effect". To investigate if the "Boltzmann effect" also dominates the temperature dependence of DIET at negative sample bias and the influence of a potential temperature dependence of the electronic lifetime on the desorption probability, a hypothetical "DIET-hole-experiment" was modelled here.

In [82], the temperature dependence of the excited state lifetime is assumed as

$$\tau^{-1} = \Gamma_{ge} = a + b(e^{c/T_s} - 1)^{-1} \quad , \tag{3.23}$$

with the reciprocal intrinsic lifetime $1/\tau_0 = a = 1/0.67$ fs, $b = 1/0.91$ fs and c = 402 K. With this parametrisation $\tau(0\text{ K}) = 0.67$ fs, $\tau(300\text{ K}) = 0.53$ fs and $\tau(600\text{ K}) = 0.38$ fs is obtained. These values of τ are within the same order of magnitude

as the excited state lifetimes obtained in the previous chapter 3.2.3 about STM-induced DIET at positive sample bias, but they are now temperature dependent – the higher the substrate temperature, the smaller the lifetime and thus the smaller the desorption probability per excitation event.

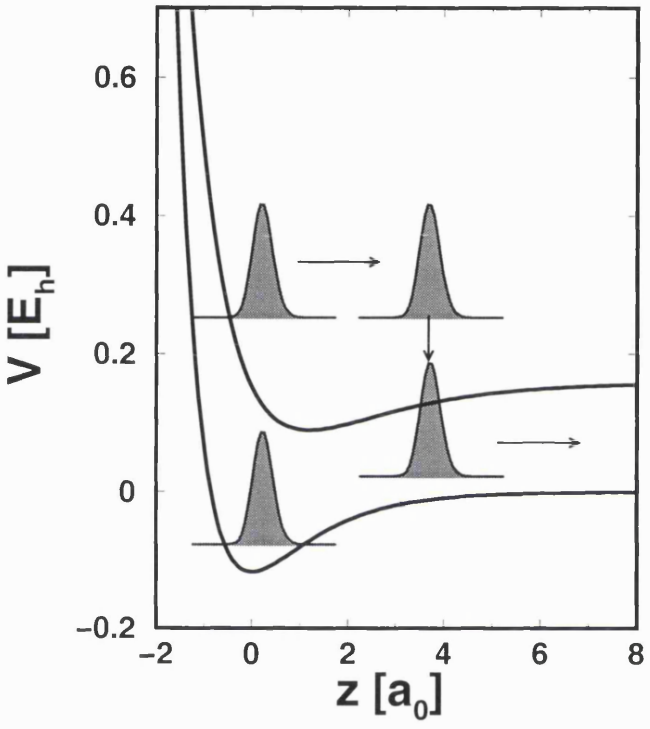

Figure 3.8: *Potential energy curves for the Si(100)-(2x1):H electronic ground state and for an excited state which is assumed to be a "hole resonance". After excitation, the wave packet will move initially away from the surface, as it is the case in the MGR model.*

To model the temperature dependence of a STM DIET process at negative bias, the same open system density matrix approach was adopted as in section 3.2.2 for the desorption at positive bias. The difference to the previous model lies in the shape of the electronically excited state. As long as the hole resonance state is not stabilised by image charges, which is a reasonable assumption for silicon, this excited state is expected to remain bound, but with a larger bond length than in the electronic ground state. Out of these considerations, an approximate excited

state potential can be constructed, which is still of the MGR type in the sense that the initially excited wave packet will still move outward (see Fig.3.8) With this model excited state potential it should be possible to investigate the influence of the two temperature effects, namely the "Boltzmann effect" and the "electronic lifetime effect" at least qualitatively.

In the hole resonance model, the electronic ground state potential $V_g(Z)$ should still be the same as for the $\sigma \rightarrow \sigma^*$ model in section 3.2.2. However, the excited state potential is now a displaced and shifted Morse oscillator:

$$V_e(Z) = D_+[1 - e^{-\alpha_+(Z-z_+)}]^2 + K \tag{3.24}$$

with $D_+ = 0.0694\,E_h$, $\alpha_+ = 0.557\,a_0^{-1}$, $Z_+ = 1.2\,a_0$ and $K = 0.207\,E_h$. This parametrisation is based on an idea by Jennison et al. [83], who constructed a hole resonance state for the dissociation of SiH bonds in the bulk, exploiting an analogy with the formation of H_2^+ from H_2 by "hole attachment". For the H_2 molecule, the equilibrium bond length increases by a factor of 1.418, the binding energy decreases by a factor of 1.69 as does the vibrational frequency by a factor of 1.895, when going from H_2 to H_2^+.

Assuming that the same scaling applies to the SiH bond when ionised and using the harmonic approximation to relate the Morse exponents to vibrational frequencies, the potential parameters listed above are obtained, as is the excited state potential shown in Fig.3.8. K is determined such that the energy difference $V_e(0) - V_g(0)$ matches the experimental resonance energy of 0.257 E_h [82]. This modified MGR model with the temperature-dependent, bound excited state is henceforth denoted as "MGR-2", in contrast to the $\sigma \rightarrow \sigma^*$ situation, denoted "MGR-1". The numerical parameters for the calculation are the same as in Table 3.1.

Within both models, the desorption probability shows a strong increase with increasing resonance lifetime τ, as shown in Fig.3.9, upper panel. For realistic lifetimes ($\tau < 1$ fs), the hole model MGR-2 (solid lines), predicts desorption yields at a given τ that are slightly larger than for the $\sigma \rightarrow \sigma^*$ MGR-1 model (dot-dashed

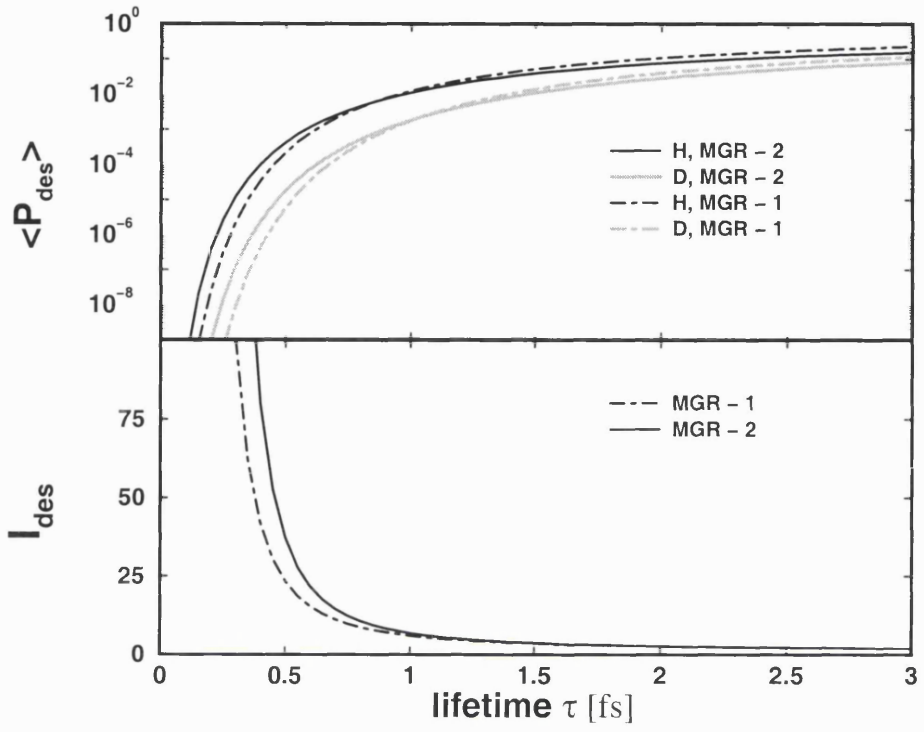

Figure 3.9: *Desorption probability of H (black) and D (grey) for Si(100):H(D) in the DIET regime, as obtained with MGR model 2 for desorption at negative sample bias (bound excited state, solid lines) and with MGR-1 for positive bias (repulsive excited state, dot-dashed lines) .*

lines). This is mainly because the slope of the excited state at the Franck-Condon point, $|V_e'(0)| = |\frac{dV_e}{dz}|_0$ is larger for the former (Fig.3.8) than for the latter (Fig.3.1).

The desorption yields translate into the isotope effects I_{des} as given in the lower panel of Fig.3.9. I_{des} decays exponentially with τ, as already discussed in section 3.2.3. For a given lifetime, the isotope ratio is smaller for the MGR-2 hole model than for MGR-1 situation. This follows from the simple rule that high yields correspond to small isotope effects and vice versa.

In Fig.3.10, finite temperature effects are considered. For the hole resonance model MGR-2, Ref.[82] gives information about the dependence of the excited state lifetime on the substrate temperature T_s. With the parametrisation Eq.3.23, a

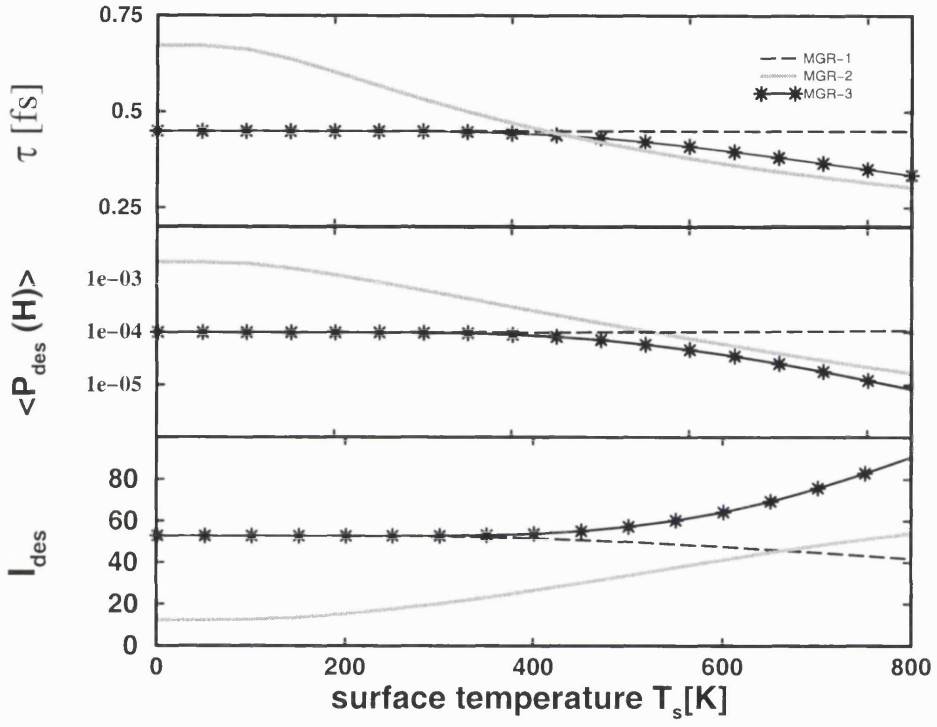

Figure 3.10: *Surface temperature effects in the STM "above threshold" desorption regime. In the upper panel, the excited state lifetime τ is shown for the 3 different MGR models (see text). The grey line represents the temperature dependence of the excited state lifetime for the MGR-2 hole model, as obtained with the parametrisation of Ref.[82]. The solid line is $\tau(T_s)$ as assumed to be reasonable for the $\sigma \rightarrow \sigma^*$ resonance (MGR-3, see text), while the T_s independent $\tau = 0.45$ fs of MGR-1 is shown as horizontal, dashed line. In the middle panel, the H desorption probabilities obtained with the 3 different models are given, while in the lower panel the corresponding isotope ratios I_{des} are shown.*

lifetime τ is obtained as indicated in the upper panel of Fig.3.10 as grey line. With this information, both the "Boltzmann effect" and the "electronic lifetime effect" can be included. To obtain the temperature dependence of $\langle P_{des} \rangle$ no new propagations for different surface temperatures are necessary, but Eq.(3.11) has to be generalised to a include the temperature dependence of the lifetime τ:

$$\langle \hat{A} \rangle (t; T_s) = \sum_v w_v(T_s) \cdot \frac{\int_0^\infty e^{-\tau_R/\tau(T_s)} A(t; \tau_R; v_g)\, d\tau_R}{\int_0^\infty e^{-\tau_R/\tau(T_s)}\, d\tau_R} \quad . \tag{3.25}$$

The computed final desorption probability is shown as grey line in the middle panel of Fig.3.10 for hydrogen and compared with the MGR-1 model, where just the "Boltzman effect" was included (dashed line).

The experimentally observed temperature suppression of the desorption yield in case of negative sample bias occurs as a consequence of the decreasing electronic lifetime. Quantitatively, the hydrogen desorption probability decreases by a factor of ≈ 10 when increasing the substrate temperature from 0 K to $T_s = 450$ K. In the experiments of Stokbro et al. for STM DIMET at negative sample bias [82], the desorption rate became ≈ 200 times smaller when the system was heated from 300 K to 450 K (for a sample bias of -7 eV and a tunneling current $I = 2$ nA). The proposed simple MGR-2 open system density matrix model implies qualitatively comparable observations for DIET at negative sample bias. The theoretical model predicts further that the isotope ratio I_{des} should increase significantly with substrate temperature, simply because the yields become smaller, thus favouring larger isotope effects.

In the previous sections, an opposite temperature effect was predicted for the $\sigma \rightarrow \sigma^*$ scenario, corresponding to the experiments at positive sample bias by Avouris et al. [72]. Here, I_{des} should decrease for temperature $T_s > 300$ K, because $\langle P_{des} \rangle$ starts to increase. However, the calculations considered so far did not account for a possible temperature dependence of the σ^* resonance lifetime - only the Boltzmann averaging (Eq.(3.11)) was done. The reason for the increase of the desorption probability in the MGR-1 model is that only at higher T_s are higher vibrational states of H and

D significantly populated, hence I_{des} diminishes with increasing T_s. In Fig.3.10, this is illustrated as dashed lines in the middle and lower panel for a temperature independent lifetime of $\tau = 0.45$ fs respectively.

To examine what might happen when possible additional, but opposite effects due to a T_s dependent resonance lifetime are taken into account, test-calculations for an assumed temperature dependent σ^* state were done, henceforth denoted MGR-3. Unfortunately, the variation of τ on T_s is not known for the $\sigma \rightarrow \sigma^*$ resonance. $\tau =$ 0.45 fs is the lifetimes which reproduces the correct isotope effect in the MGR-1 model. This was exploited for a new parametrisation of Eq.(3.23), resulting in $a =$ 0.45 fs^{-1}. A "reasonable" temperature dependence should allow one to reproduce the experimentally observed T_s *-independent* desorption probabilities and isotope effect for up to $T_s = 300$ K. For this, the remaining parameters were chosen to be $b =$ 1/0.07 fs and c = 2500 K and the results are shown in Fig.3.10 as solid lines. A look at the desorption probabilities (shown for H in the middle panel) reveals that the second, yield-diminishing effect dominates over the "Boltzmann effect" also in this case. As a consequence, the isotope effect I_{des} would increase rather than decrease with surface heating.

However, because conclusive evidence on the T_s dependence of τ is lacking for the MGR-3 scenario, it can only be predicted here that there should be a measurable change in the desorption probabilities and thus in the isotope ratio for substrate temperatures $T_s > 300$ K. If I_{des} decreased with increasing T_s, this would indicate that, even at temperatures above 300 K, the lifetime of the $\sigma \rightarrow \sigma^*$ resonance is fairly independent of the substrate temperature. Conversely, if I_{des} goes up with T_s, a strong decrease of τ with T_s is (tentatively) predicted, comparable to the hole resonance situation of Ref.[82].

3.2.7 Summary and conclusions

The STM induced desorption of hydrogen and deuterium from Si(100) in the "above electronic threshold" region was investigated using an open system density matrix description and 2 states - 1 mode Menzel-Gomer-Redhead (MGR) type DIET models. For zero temperature, the experimental desorption probabilities and the isotope effect in the desorption at positive sample bias could be reproduced, indicating an excited state lifetime $\tau < 1$ fs.

Additionally, the temperature effects during STM DIET were investigated for excitation via a repulsive σ^* a bound σ hole resonance respectively, corresponding to experiments at positive and negative sample bias. It was found that two major sources contribute to the possible strong temperature dependence of the desorption dynamics - a "Boltzmann" and an "electronic lifetime effect". The first one favours, the second one suppresses desorption. A priori, it is not clear which of these effects dominates for a specific system. For desorption via a hole resonance (corresponding to negative sample bias) it was found that the yield diminishing "electronic lifetime effect" dominates over the yield enhancing "Boltzmann effect", resulting in decreasing desorption probabilities and increasing isotope ratios with increasing surface temperature, as was already experimentally observed for STM DIMET at negative sample bias.

In the case of desorption via the $\sigma \rightarrow \sigma^*$ resonance (positive sample bias), the experimentally observed insensitivity of the desorption dynamics on the substrate temperature for T_s up to room temperature is assumed to be due to the fact the vibrational level spacing for SiH(D) is comparatively large, such that vibrational levels with $v_g > 0$ are not significantly populated up to $T_s \approx 300$ K. Above this temperature, desorption probabilities and the corresponding isotope ratio will vary strongly with the substrate temperature. However, because the temperature dependence of the electronic lifetime on the surface temperature T_s is not known for the $\sigma \rightarrow \sigma^*$ resonance, detailed predictions about the magnitude of the variation with

T_s above 300 K are not yet possible. In summary, the temperature dependence of the desorption dynamics appears to be a potentially rich source for the microscopic clarification of non-adiabatic processes at solid surfaces.

3.3 The effects of the external electric field

An important perturbation that the STM tip can exert on the sample is provided by the electric field due to the applied voltage between tip and sample. During "normal" STM imaging, this field is in the order of 0.1 V/Å. Higher fields, of the order of 1V/Å, can be produced by applying voltage pulses without changing the tip-sample distance. Such fields can be used to break strong covalent bonds such as SiSi bonds [84], to move atoms laterally on surfaces [21] and to induce field-desorption [85]. The electric fields produced by the STM can cause changes in the occupation of molecular orbitals, strengthening or weakening the adsorbate-surface bond [86]. For atomic-scale modification schemes utilizing the STM current-induced excitation of adsorbates, the role of the electric field is primarily through the Stark shift of the excitation energy. It has been suggested [67, 86] that this shift can play an important role in determining the resolution of the modification process.

The effects of an external electric field of magnitude comparable to the one present in the STM on the bond strength and the vibrational frequency of H adsorbed on Si(111) were recently examined by Akpati et al. [67] by local density functional theory. They found that the SiH bond is weakened and breaks at high fields, but that the effect of the field is much stronger when the field direction is in the opposite direction than the bond dipole.

To obtain a conceptual understanding of the influence of the external electric field on the Si(100):H system, the effects on the bond strength and vibrational frequencies were examined here as well. To simplify the problem, field-inhomogeneities are neglected and the field $\vec{F}$ is assumed to be parallel to the SiH bond, $\vec{F} \rightarrow F_z := F$.

Under the influence of the external electric field F, the system Hamiltonian $\hat{H}_s$

becomes

$$\hat{H}_s = \hat{H}_0 + \hat{H}_1 \tag{3.26}$$

$$\hat{H}_0 = -\frac{\hbar^2}{2m}\frac{d^2}{dZ^2} + V(Z)$$

$$\hat{H}_1 = -\left(\mu_0(Z) + \frac{\alpha(Z)}{2}F\right) \cdot F \quad . \tag{3.27}$$

The total dipole moment μ^{tot} is defined as the sum of the permanent dipole moment μ^{perm} of the SiH bond and the induced dipole moment μ^{ind} of the system in a uniform field $\hat{F}$:

$$\mu^{tot}(Z) = \mu^{perm} + \mu^{ind} = \mu_0(Z) + \alpha(Z) \cdot F \quad . \tag{3.28}$$

To examine the modifications of the equilibrium structure and the bond strength, the dipole function $\mu_0(Z)$ and $\alpha(Z)$, which represents the α_{zz}-component of the polarizability tensor, were computed by a cluster calculation (the cluster contains one H and one Si atom) using a gradient corrected hybrid density functional (B3LYP) and a 6-31G** basis set [87, 88]. The result is shown in Fig.3.11.

Using the Morse potential $V(Z) = V_g(Z)$ from Eq.(3.5), the eigenstates and eigenenergies of the field influenced system were calculated by direct diagonalisation of the Hamiltonian Eq.(3.27) represented by a sinc function *discrete variable representation* (DVR) [89] (see appendix A.1). Fig.3.12 shows the potential energy curves, $V(Z) = V_g(Z) - \mu_0 \cdot F - \frac{\alpha}{2} \cdot F^2$, of the SiH system for electric field values ranging from - 1 V/Å to + 1 V/Å [1].

Apparent from the potential energy curves are the variations in the dissociation energy and the bond length of the system as a function of the field strength and direction. For positive fields, i.e., fields directed from Si to H, the potential curves show a steady broadening of the potential well and a decrease of the potential energy barrier for the SiH bond dissociation with increasing field strength up to $F = 1$ V/Å, then a steady increase in the barrier height. In Table 3.3 the equilibrium bond

[1] It is convention, that the field is referred to as "positive" if the sample represents the positive electrode, i.e., the current is directed from the STM tip to the sample.

F [V/Å]	$Z_0[a_0]$	$D[E_h]$	$\omega_0[eV]$	N_b
-2.0	-0.11	0.1049	0.262	31
-1.5	-0.08	0.1252	0.261	29
-1.0	-0.05	0.1218	0.258	26
-0.8	-0.05	0.1207	0.255	26
-0.6	-0.05	0.1197	0.252	25
-0.4	-0.05	0.1187	0.249	25
-0.2	0.00	0.1179	0.245	25
0.0	0.00	0.1172	0.240	25
+0.2	0.00	0.1167	0.235	26
+0.4	0.05	0.1163	0.231	27
+0.6	0.05	0.1161	0.222	28
+0.8	0.05	0.1160	0.214	29
+1.0	0.05	0.1164	0.205	30
+1.5	0.19	0.1178	0.176	33
+2.0	0.35	0.1216	0.128	38

Table 3.3: *Calculated equilibrium bond displacement Z_0, dissociation energy D, vibrational frequency ω_0 and the number of bound states N_b for the SiH cluster for field values ranging from -2 V/Å to +2 V/Å.*

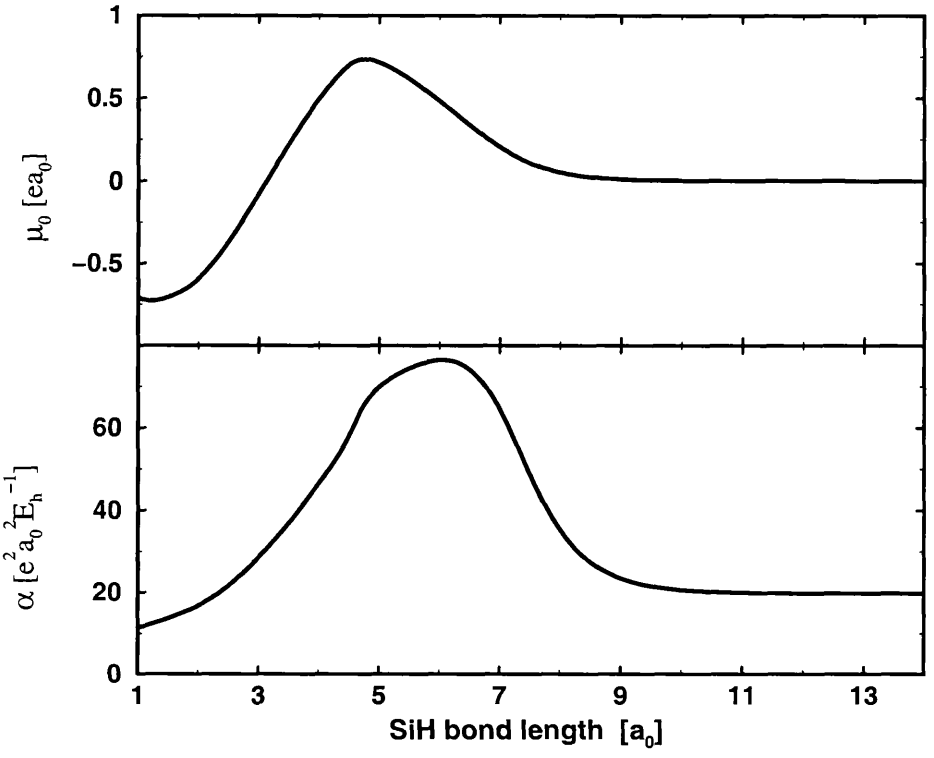

Figure 3.11: *Computed dependence of the dipole function $\mu_0(Z)$ and the α_{zz}-component of the polarizability tensor on the SiH bond length. The functions were calculated using a gradient corrected hybrid density functional (B3LYP) and a 6-31G** basis set [87, 88].*

displacement, the dissociation energy, the vibrational frequency $\omega_0 = \varepsilon_{1g} - \varepsilon_{0g}$ and the number of bound states, N_b, are given as a function of the external field for field strengths between - 2 V/Å and + 2 V/Å. It can be seen that the broadening of the potential well leads to a significant increase of the number of bound states with increasing field strength. This is important for the theoretical treatment of the STM-induced desorption in the "below threshold" limit, as it is shown in the section 3.4.

For negative fields (directed from H to Si), the changes in the characteristics are generally less pronounced. With increasing negative field strength, the dissociation energy now shows a steady increase up to -2 V/Å. The equilibrium bond

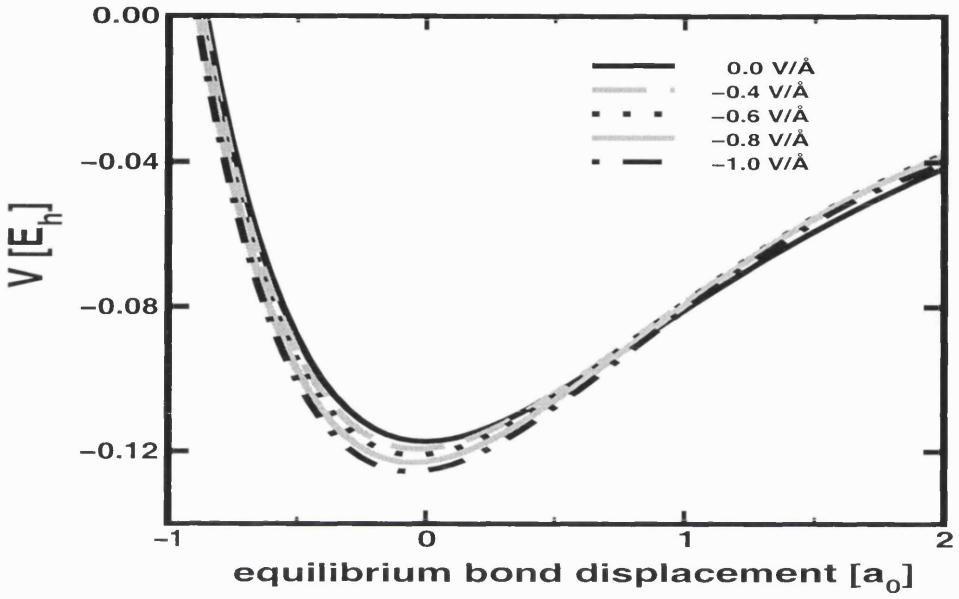

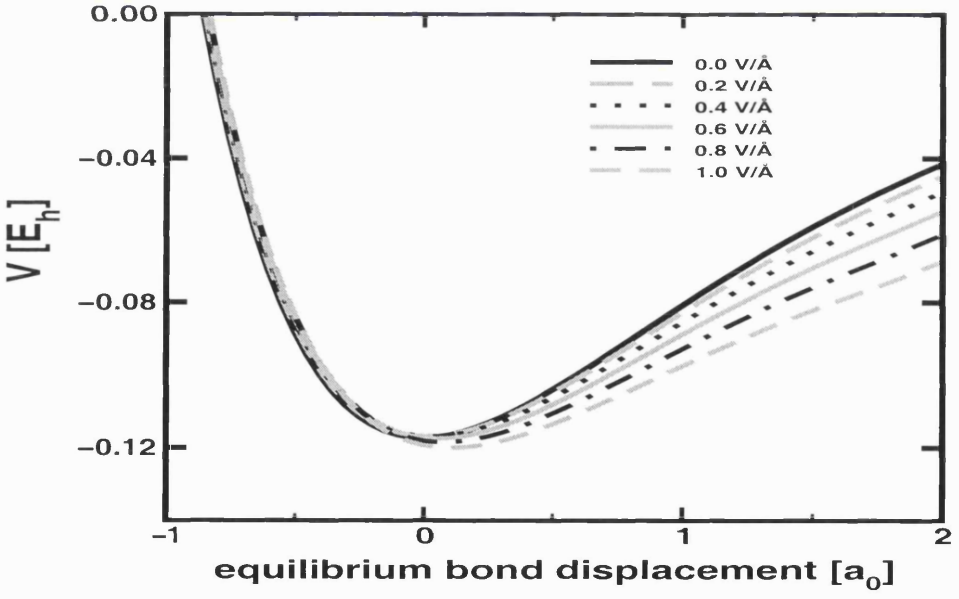

Figure 3.12: *Potential energy curves,* $V(Z) = V_g(Z) - \mu_0 \cdot F - \frac{\alpha}{2} \cdot F^2$, *of the SiH cluster in a homogene electric field for negative (upper panel) and positive electric field values (lower panel) ranging from - 1 V/Å to + 1 V/Å.*

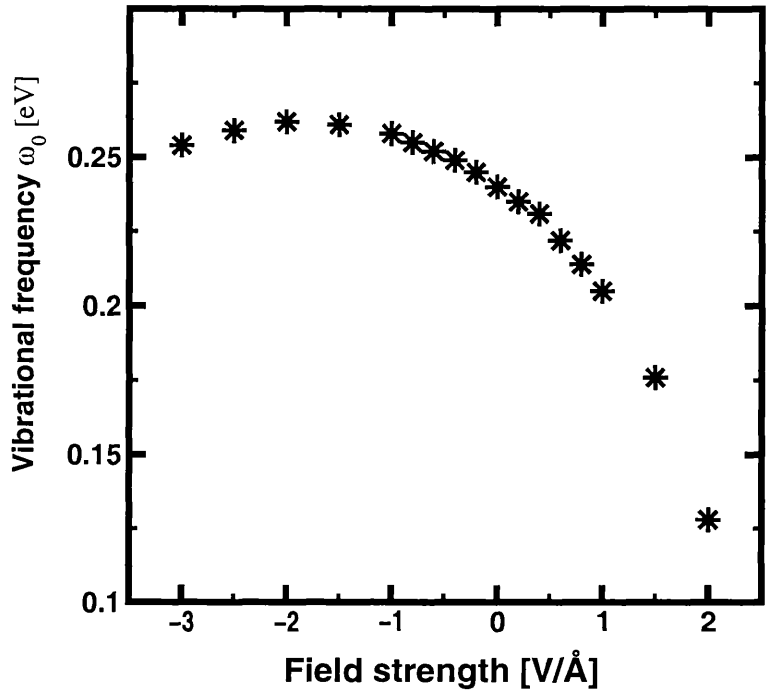

Figure 3.13: *Vibrational frequencies for SiH as a function of the applied electric field, for F ranging from -3 V/Å to 2 +V/Å.*

displacement Z_0 decreases with F, reflecting the strengthening of the SiH bond by the electric field –in contrast to positive fields, where Z_0 increases steadily with the field strength– as shown in Fig.3.12.

In Fig.3.13, the variation of the SiH stretch vibrational frequency as a function of the electric field strength and direction is shown. The curve indicates a maximum around - 2 V/Å, in good agreement with density functional calculations by Akpati et al. for the Si(111):H system [67]. This extremum (as well the the minimum in the bond length distribution, Table 3.3) can be explained with the help of a simple tight-binding model, as it was shown by Persson and Avouris [86]. They assumed that the adsorbate-surface bond involves the interaction of an orbital $|a\rangle$ on the adsorbate with a substrate orbital $|b\rangle$ [2]. Persson and Avouris found that for a given pair of energy levels, ε_a and ε_b, the frequency as a function of F maximises when both levels are in resonance, since at resonance the SiH bond is strongest and

[2]In the case of H on Si, $|a\rangle$ will be the hydrogen 1s orbital and $|b\rangle$ will be a Si sp^3 orbital.

therefore the bond length minimal. Both on the right and the left of the extremum, the vibrational frequency decays monotonically, as is also indicated in Fig.3.13. This is the same behaviour as also found in first-principles calculations [90].

The calculations for the vibrational frequency indicate that the vibrational Stark shift for fields present in the STM experiments are large enough to significantly influence the vibrational dynamics. For example, a typical field for STM induced H desorption experiments of ≈ 0.5 V/Å leads to a Stark shift of ≈ 11 meV. This shift is larger than than the dispersion width of about 1.2 meV [91]. According to the results in Ref.[86], this shift can significantly reduce the energy transfer rate to surrounding adsorbates and thus allow local activation of surface dynamical processes.

As it was shown by Akpati et al. for the Si(111):H system [67], the consideration of a larger cluster does not lead to a generally different field dependence of the characteristics, but the effects are somehow reduced. The Stark shift, for example, is diminished from 12 meV for the SiH cluster to ≈ 4.5 meV for a $Si_{10}H$ cluster ($F = 0.5$ V/Å), but still this shift is sufficient to reduce the energy transfer rate.

3.4 Desorption in the "below threshold" limit

3.4.1 Review of experimental results and previous theoretical treatment

Avouris and co-workers observed in their STM desorption experiments (positive sample bias) that excitation of the Si(100)-(2x1):H system by electrons with energies below those needed for electronic excitation can still lead to H desorption, albeit with a much lower yield [18]. Furthermore, the desorption characteristics are very different from those of the desorption process above the electronic threshold. A strong dependence of the desorption yield on the tunneling current I is observed ($\propto I^{\eta}$ with $\eta \sim$ 10-13) and there is a remarkable enhancement of desorption, ~ 300 times, when cooling from 300 K to 11K. Furthermore, deuterium desorption in the

tunneling regime is only achievable at 11 K [3] [17, 18, 29, 72, 73].

The strong current dependence indicates that many electrons might be involved in the excitation-desorption process. It was assumed that because of the extremely high current densities present in the STM (as high as 1×10^6 A cm^{-1}) and the long vibrational lifetime ($\sim$ ns) of the SiH mode [75], the inelastic tunneling can cause multiple vibrational excitation and subsequently desorption [17]. A simple model of a truncated harmonic oscillator where the tunneling current and thermal phonon processes induce transitions between the quantum levels of the oscillator was used for the description of the desorption process (see below) and the temperature dependence of the desorption yield was found to origin mainly from a temperature dependence of the vibrational lifetime of the SiH bond [72, 26, 19].

3.4.2 General aspects of the STM-induced desorption in the multiple excitation limit

The possibility of overcoming a potential barrier via "vibrational heating", i.e., multiple vibrational excitations by laser-excited hot electrons or inelastic scattering STM electrons for example, has been investigated by various groups [92, 93, 94, 81, 95, 96, 97, 30, 19]. A universal feature of the vibrational heating mechanism leading to DIMET is the perturbation of the adsorbate-surface bond by successive electron scattering at a rate comparable to vibrational relaxation. The resulting increase in vibrational temperature leads to an enhanced desorption probability due to electronic re-excitation from vibrationally excited states (see Fig.3.14). Furthermore, this "vibrational ladder climbing" mechanism allows desorption to occur even if the electronic excitation energy is below the threshold for the direct excitation discussed in the previous section 3.2.

The degree of vibrational heating induced depends on the balance between vibrational excitation and relaxation processes (see Fig.3.14). With the STM, inelas-

[3] So far, to my knowledge, experiments were performed at 11 K and 300 K only.

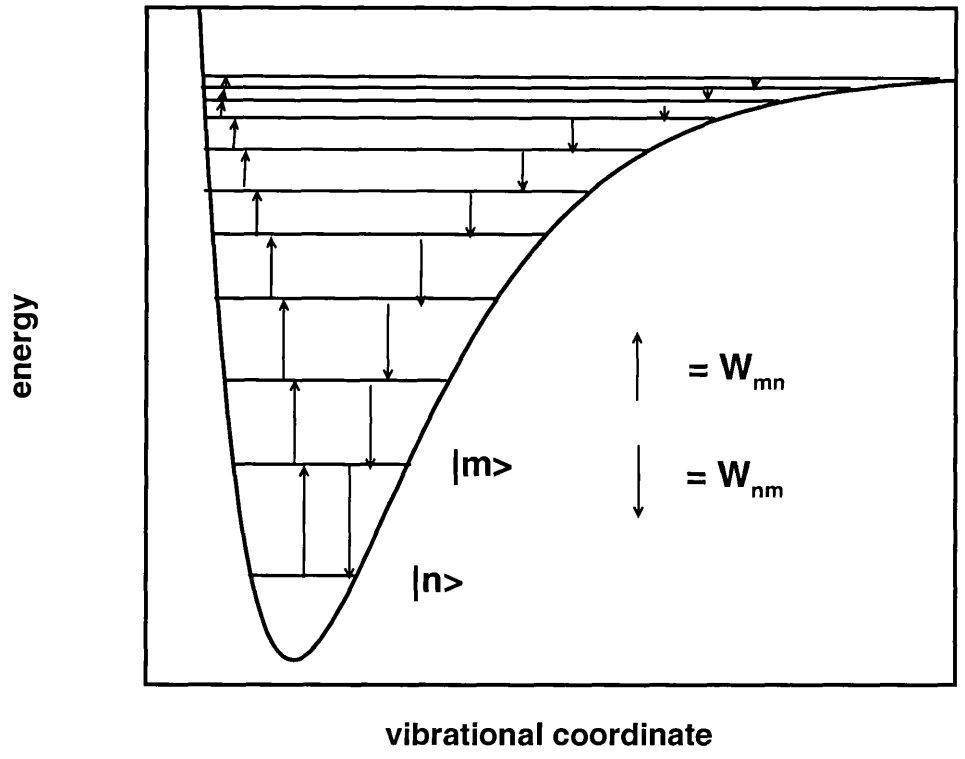

Figure 3.14: *Sketch of the "vibrational ladder climbing" mechanism ($\Delta_{nm} \geq 1$). Desorption will occur if the "ladder" can be climbed high enough to overcome the desorption barrier.*

tically scattering tunneling electrons excite transitions from vibrational quantum states $|v_n\rangle$ to states $|v_m\rangle$ ($\Delta_{nm} \geq 1; m > n$) with a rate $W_{m,n}^{inel}$ proportional to the tunnel current while both the dipole and the resonance mechanism (see section 3.1 and below) contribute

$$W_{m,n}^{inel} = \frac{I}{e} \cdot (W_{m,n}^{inel,dip} + W_{m,n}^{inel,res}) \quad . \tag{3.29}$$

At finite temperature the system can also absorb thermal energy from the substrate. To account for the vibrational excitation as consequence of this thermal heating, $W_{m,n}^{inel}$ has to be combined with a rate $W_{m,n}^{therm}$ to obtain a total "upward rate"

$$\Gamma_{m,n}^{\uparrow} = W_{m,n}^{inel} + W_{m,n}^{therm} \quad . \tag{3.30}$$

In order for the excitation to induce bond-breaking, it has to remain localized at the particular site for an appropriate time period. However, competing with

the excitation process are energy transfer processes to the substrate by coupling to phonons (excitation quenching) and to surrounding adsorbates (excitation delocalisation, Förster type energy transfer [98]). Additionally, interaction with the tunneling electrons scattering inelastically can also lead to energy relaxation from vibrational states $|v_m\rangle$ to $|v_n\rangle$ of the system so that one obtains a total "downward" transition rate

$$\Gamma^{\downarrow}_{n,m} = W^{inel}_{n,m} + W^{diss}_{n,m} + W^{F}_{n,m} \quad . \tag{3.31}$$

Here, $W^{F}_{n,m}$ accounts for the Förster transfer and $W^{diss}_{n,m}$ is the dissipative vibrational decay (quenching) rate.

If all the excitation and de-excitation rates are known, the microscopic dynamics of DIMET processes can be described with a kinetic model for the vibrational heating mechanism. In this model, the vibrational response of a local bond to the multiple electronic perturbation is described by the probability distribution among the vibrational eigenstates, whose evolution is determined by a Pauli master equation, or rate equation (see below). How to choose the individual "up" and "down" rates is discussed in the next section in detail.

3.4.3 Excitation and relaxation rates

3.4.3.1 Contributions from inelastically scattering tunnel electrons

STM DIMET at positive sample bias is caused by tunneling electrons from the tip which scatter inelastically on the surface-adsorbate system. The fraction f_{in} of STM electrons scattering inelastically arises from two different excitation mechanisms, namely the dipole and the resonance mechanism, i.e., $f_{in} = f^{dip}_{in} + f^{res}_{in}$.

Inelastic tunneling from a metal tip was investigated theoretically by Persson and co-workers within the harmonic limit, assuming that all the tunneling electrons derive from one single tip atom [96, 99]. For the contribution of the dipole mechanism, where the electric field of a tunneling electron near an adsorbate is thought of as interacting with the transition dipole moment μ_{if} of an excitation from an initial

adsorbate state $|i\rangle$ to a final state $|f\rangle$, the authors estimated the magnitude of f_{in}^{dip}, e.g. for a typical $|v_0\rangle \rightarrow |v_1\rangle$ vibrational transition, to be approximately [96]

$$f_{in}^{dip} \approx \left(\frac{\mu_{01}}{ea_0}\right)^2 = \left(\frac{\langle v_0|\mu(Z)|v_1\rangle}{ea_0}\right)^2 \quad , \tag{3.32}$$

where e is the electron charge and a_0 the Bohr radius. Expanding the dipole function $\mu(Z)$ up to the linear term around the equilibrium position $Z_0 = 0$ of the vibrational coordinate

$$\mu(Z) \approx \mu(0) + \frac{d\mu}{dZ}|_0 \cdot Z = \mu(0) + \mu'(0) \cdot Z \tag{3.33}$$

gives for the transition dipole matrix elements

$$\langle v_n|\mu(Z)|v_m\rangle \approx \langle v_n|\mu(0)|v_m\rangle + \langle v_n|\mu'(0) \cdot Z|v_m\rangle = \mu'(0)\langle v_n|Z|v_m\rangle \quad . \tag{3.34}$$

If $|v_n\rangle$ and $|v_m\rangle$ are eigenfunctions of the harmonic oscillator, the matrix elements $\langle v_n|Z|v_m\rangle$ are given analytically

$$\begin{aligned} \langle v_n|Z|v_{n+1}\rangle &= \sqrt{\frac{\hbar}{2M\omega_0} \cdot (n+1)} \\ \langle v_n|Z|v_{n-1}\rangle &= \sqrt{\frac{\hbar}{2M\omega_0} \cdot n} \\ \langle v_n|Z|v_m\rangle &= 0 \quad \text{for} \quad \Delta_{nm} > 1 \end{aligned}$$

where M is the reduced mass and ω_0 the frequency of the oscillator. Thus Eq.(3.32) simplifies to

$$f_{in}^{dip} \approx \left(\frac{\mu'(0)}{ea_0}\right)^2 \cdot \frac{\hbar}{2M\omega_0} \quad , \tag{3.35}$$

which gives the share of tunneling electrons scattering inelastically due to dipole interaction in harmonic-linear approximation. With the derivative of the dipole moment calculated for SiH in section 3.3, $\mu'(0) \approx 1.5$ D a_0^{-1}, it is possible to give an estimate of $f_{in}^{dip} \approx 0.01$ for the SiH system ($\hbar/2M\omega_0^{\mathrm{SiH}} \approx 0.03\, a_0$). However, as discussed in section 3.3, the dipole function calculated in this work for a two-atomic cluster might be over-estimated. Recently, more accurate calculations on the dipole function were done by Stokbro [100]. By using density functional theory within the

generalized gradient approximation and a slab with 12 Si atoms and 6 H atoms, he obtained a much smaller dipole derivative, namely $\mu'(0) = 0.3$ D a_0^{-1}. With this, a much smaller fraction $f_{in}^{dip} \approx 2 \times 10^{-3}$ is obtained.

The temporary trapping of the incident tunnel electron causes a change of the internuclear potential which induces an excitation (or relaxation) of the adsorbate-surface bond. The corresponding contribution f_{in}^{res} of this resonance mechanism to the inelastic current was also determined by Persson and co-workers [99]. For a $|v_0\rangle \rightarrow |v_1\rangle$ vibrational excitation, for example, it is

$$f_{in}^{res} \approx \frac{|V'_{res}(0)\langle v_0|Z|v_1\rangle|^2}{(V_{res}(0) - V_g(0) - eV)^2 + (\frac{\hbar\gamma(0)}{2})^2} \cdot \frac{[V_{res}(0) - V_g(0) - eV + \hbar\omega_0]^2 - (\frac{\hbar\gamma(0)}{2})^2}{[V_{res}(0) - V_g(0) - eV + \hbar\omega_0]^2 + (\frac{\hbar\gamma(0)}{2})^2} \quad . \tag{3.36}$$

Here, V_{res} is the resonance level and V_g the harmonic ground state potential and ω_0 is, as above, the vibrational frequency of the harmonic oscillator. $\hbar\gamma(0)/2$ is the half width of the resonance $V_e(Z)$ at $Z = Z_0 = 0$. The influence of the applied electric field on the energy levels is included by the factor $-eV$, where V is the (positive) sample bias. If field effects are neglected and the assumption $\hbar\gamma(0) <<$ excitation/de-excitation energy is made, Eq.(3.36) simplifies drastically to

$$f_{in}^{res} \approx \frac{\hbar}{2M\omega_0} \cdot \frac{|V'_{res}(0)|^2}{|V_{res}(0) - V_g(0)|^2} \quad . \tag{3.37}$$

Recent density functional calculations by Stokbro et al. showed that the negative ion resonance involved in the SiH DIMET process considered here is centred at $\approx$ 4.6 eV while the force acting along the vibrational coordinate, $-V'_{res} = -\frac{dV_{res}}{dZ}$, was calculated to $\approx$ 3.12 eV/Å at $Z_0 = 0$ [19]. Thus, $f_{in}^{res} \approx 0.02$ can be estimated, which implies that the resonance contribution is about 10 times higher [4]. A general dominance of the resonance mechanism over the dipole contribution was also found earlier by Persson and Baratoff [99].

[4] With regard to the higher accuracy of the slab-calculated dipole moment and the so obtained f_{in}^{dip}

Finally, the transfer rates arising from the inelastic tunnel fraction are proportional to the total tunnel current I. For transitions between harmonic oscillator states $|v_n\rangle$ and $|v_m\rangle$ with $\Delta_{nm} = \pm 1$, for example, the total "up" and "downward" rates arising from the inelastic scattering of tunneling electrons are thus given by

$$W^{inel}_{n,n-1} = W^{inel,dip}_{n,n-1} + W^{inel,res}_{n,n-1} = \frac{I}{e} \cdot f_{in} \cdot n \tag{3.38}$$

$$W^{inel}_{n,n+1} = W^{inel,dip}_{n,n+1} + W^{inel,res}_{n,n+1} = \frac{I}{e} \cdot f_{in} \cdot (n+1) \tag{3.39}$$

with $f_{in} = f^{dip}_{in} + f^{res}_{in}$. Note that if f^{res}_{in} and f^{dip}_{in} are estimated from a harmonic-linear model (Eqs.(3.35) and (3.37)), the sample bias is not longer explicitly included, which means that the energy of the tunneling electrons, i.e. the excitation energy, is neglected.

3.4.3.2 Energy dissipation and vibrational lifetime

One of the main factors that controls the desorption yield is the vibrational energy decay rate, caused by coupling to substrate phonons and neighbouring adsorbates. $W^{diss}_{0,1}$ is the rate for the relaxation of system from its first vibrational excited state to its ground state and equal to the reciprocal (temperature dependent) vibrational lifetime

$$W^{diss}_{0,1}(T_s) = \frac{1}{\tau_{vib}(T_s)} \quad . \tag{3.40}$$

In a harmonic-linear excitation picture, relaxations of higher neighbouring vibrational states are proportional to $W^{diss}_{0,1}$, e.g.,

$$W^{diss}_{n,n+1}(T_s) = W^{diss}_{0,1}(T_s) \cdot (n+1) \quad . \tag{3.41}$$

Efficient bond-breaking via vibrational excitation becomes only possible for the SiH system because of the long lifetime τ_{vib} of the SiH stretch frequency. The long lifetime ($\sim$ ns) is a result of a vibrational quantum far above the Si phonon spectrum and too low for a coupling with electron-hole excitations. Thus the energy can only be transferred via a multi-phonon process [26].

Thermal heating is also due to a substrate phonon coupling mechanism. Because dissipative energy decay and thermal heating are reversible microscopically, $W_{m,n}^{therm}$ and $W_{n,m}^{diss}$ are related through the principle of detailed balance

$$W_{m,n}^{therm}(T_s) := W_{m,n}^{diss}(T_s) = W_{n,m}^{diss}(T_s) \cdot e^{-(\epsilon_m - \epsilon_n)/k_B T_s} \quad . \tag{3.42}$$

Energy and phase relaxation times for Si(100)-(2×1):H/D were measured by Guyot-Sionnest and co-workers, using time-resolved sum frequency generation (SFG) [75]. At 300 K, the measured lifetime τ_{vib} of the symmetric SiH stretching mode is around 1.2 ns. At 100 K, τ_{vib} appears to be longer than 6 ns, but the experiments show that surface defects seem to dominate the relaxation dynamics because the individual measured values varied with the quality of the sample between 1.3 ns and 8 ns. This is not the case for Si(100)-(2×1):D where the short vibrational lifetime of about 250 ps shows consistency from sample to sample and only weak temperature dependence (τ_{vib}(100 K) = 260 ps, τ_{vib}(300 K) = 225 ps).

3.4.3.3 Stark shift and Förster type energy dissipation

The probability of multiple vibrational excitation in the silicon-hydrogen system might be enhanced by an excitation localization mechanism suggested by Persson and Avouris [86]. The lateral coupling between the SiH surface oscillators generates a band of propagating SiH phonon modes, promoting the spatial energy dissipation (Förster transfer). If the STM tip is centred over a certain SiH bond, the local electric field under the tip might shift the SiH vibrational frequency (Stark shift) outside the band of propagating adsorbate phonons [86]. In the experiments considered, the electric field under the tip is estimated to be $\leq$0.5 V/Å [17]. Actually, this is too weak to induce field desorption, but high enough to produce a Stark shift leading to a vibrational state mainly localized in the adsorbate under the STM tip. Lowering the substrate temperature leads to further reduction of Förster type vibrational energy transfer, because the dephasing rate of the SiH modes decreases, has been

measured by IR spectroscopy [101]. This increases the localization of the vibrational energy and enhances the probability for multiple excitation and desorption.

The SiH vibrational modes of the Si(100):H and Si(111):H system have been studied by various spectroscopic methods [75, 91]. Lateral coupling between the SiH oscillators on the Si(111) surface generates a band of propagating SiH phonon modes with a measured bandwidth $\Delta\omega \approx 10$ cm^{-1} and a similar bandwidth is expected for the Si(100):H system [75, 91]. If now an STM tip is placed over the SiH bond, the local electric field under tip will cause a Stark shift of the SiH frequency from frequency ω_0 to ω_F. Density functional theory calculations on SiH clusters (assuming a one-atom tip symmetry) showed that a potential difference of a few volt between the tip and the substrate gives Stark shifts of ≈ 50 cm^{-1} which shift the resonance frequency ω_F outside the band of adsorbate phonon modes [86, 67]. If thus $|\omega_F - \omega_0|$ is larger than the bandwidth $\Delta\omega$, a localized vibrational state in the Stark-shifted SiH oscillator under the tip is created. However, the lifetime of this state is not infinite. The decay rate of the localized state under the STM tip is given by the Förster formula which in the case of $|v_0\rangle \rightarrow |v_1\rangle$ relaxation takes the form [86]:

$$W_{0,1}^{F}(T_s) = \frac{\kappa \cdot \theta \cdot \Delta\omega^2}{(\omega_F - \omega_0)^2 + 4\theta^2} \quad . \tag{3.43}$$

κ has to do with the adsorbate symmetry and is 0.23 for Si(100) [26]. The temperature dependence of the linewidth θ has been measured using IR spectroscopy and is well described by [101]:

$$\theta = \theta_0 \cdot e^{\hbar\omega_s/k_B T_s} \cdot (e^{\hbar\omega_s/k_B T_s} - 1)^{-2} \tag{3.44}$$

where $\theta_0 = 1.4$ cm^{-1} for the Si(100)-H system and $\omega_s \approx 200$ cm^{-1}.

The bond anharmonicity U of the SiH vibrational mode (difference $|v_0\rangle \leftarrow |v_1\rangle$ and $|v_1\rangle \leftarrow |v_2\rangle$ transition energies) was measured to be $U \approx 80$ cm^{-1} [102]. So it is likely that for vibrational quantum states $n > 1$ the bond anharmonicity will strongly reduce the lateral energy transfer, as it was also found theoretically [86, 26].

3.4.4 Truncated oscillator model

A simple model that allows an insight into the factors that affect vibrational heating is provided by the truncated harmonic oscillator model (see Fig.3.15). In the

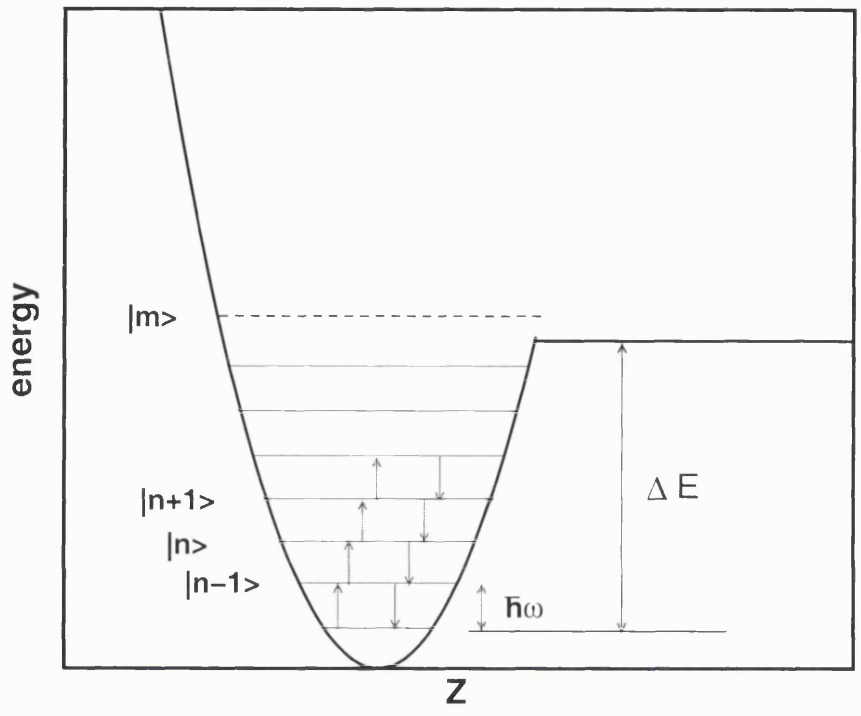

Figure 3.15: *The truncated harmonic oscillator model.*

truncated harmonic oscillator description of the energy transfer, the adsorbate vibrational motion is assumed to be harmonic and the energy transfer is assumed to occur irreversibly as soon a vibrational level $|v_m\rangle$ with energy $(m+1/2)\hbar\omega_0$ just above the barrier height ΔE is reached. The transitions among the different vibrational levels can be described by a Pauli master equation

$$\begin{aligned} \frac{dP_n}{dt} &= (n+1)\cdot\Gamma^{\downarrow}_{0,1}\cdot P_{n+1} + n\cdot\Gamma^{\uparrow}_{1,0}\cdot P_{n-1} \\ &\quad -[n\cdot\Gamma^{\downarrow}_{0,1} + (n+1)\cdot\Gamma^{\uparrow}_{1,0}]\cdot P_n \end{aligned} \tag{3.45}$$

where $P_n(t)$ is the probability to find the system at time t in the vibrational state $|v_n\rangle$ of the harmonic oscillator and $\Gamma^{\downarrow}_{0,1}$ and $\Gamma^{\uparrow}_{1,0}$ are linear excitation and relaxation rates for vibrational states $|v_0\rangle$ and $|v_1\rangle$.

The truncated harmonic oscillator model and the rate equation (3.45) were used by Avouris and co-workers to model the STM-induced bond-breaking in the "below threshold" domain for the Si(100):H system [72, 26]. With dissipative energy decay rates formulated analogous to Eq.(3.41), the corresponding "upward" rate is given, due to the principle of detailed balance, as

$$W^{diss}_{n+1,n}(T_s) = W^{diss}_{n,n+1}(T_s) \cdot e^{-\hbar\omega_0/k_BT} \quad . \tag{3.46}$$

Using additionally the harmonic-linear expressions for the inelastic tunneling rates, Eq.(3.38) and Eq.(3.39), Avouris et al. obtained for the total excitation rate $|v_{n-1}\rangle \rightarrow |v_n\rangle$

$$\Gamma^{\uparrow}_{n,n-1}(T_s) = n \cdot \left[\frac{I}{e} \cdot f_{in} + W^{diss}_{0,1}(T_s) \cdot e^{-\hbar\omega_0/k_BT_s}\right] \tag{3.47}$$

while for the de-excitation, $|v_{n+1}\rangle \rightarrow |v_n\rangle$, the rates in the harmonic-linear excitation model are given by

$$\Gamma^{\downarrow}_{n,n+1} = (n+1) \cdot \left[\frac{I}{e} \cdot f_{in} + W^{diss}_{0,1}(T_s)\right] \quad . \tag{3.48}$$

To obtain the temperature dependent energy decay rate $W^{diss}_{0,1}$, the authors evaluated the temperature dependence of the vibrational lifetime τ_{vib} theoretically under the assumption of a multi-phonon decay process and estimated τ_{vib} to be about 10 ns at room temperature and about 18 ns at 100 K [72]. Avouris et al. found an exponentially decrease of the decay rate $W^{diss}_{0,1}(T_s) = 1/\tau_{vib}(T_s)$ over the temperature range considered, as it is shown in Fig.3.16.

Inserting these "up" and "down" rates in the kinetic equation Eq.(3.45), they finally obtained the following expression for the desorption rate [72]

$$R_{des} = \lambda \cdot W^{diss}_{0,1} \cdot \frac{\Delta E}{\hbar\omega_F} \cdot \left[\frac{(I/e)f_{in} + W^{diss}_{0,1} \cdot exp(-\hbar\omega_F/k_BT_s)}{(I/e)f_{in} + W^{diss}_{0,1}}\right]^{\Delta E/\hbar\omega_F} \quad . \tag{3.49}$$

Here, $\hbar\omega_F$ is the quantum of vibrational energy in the presence of the tip-induced electric field F ($\approx$ 0.25 eV) and ΔE is the effective barrier that needs to be surmounted for desorption to take place (see Fig.3.15). Avouris and co-workers chose

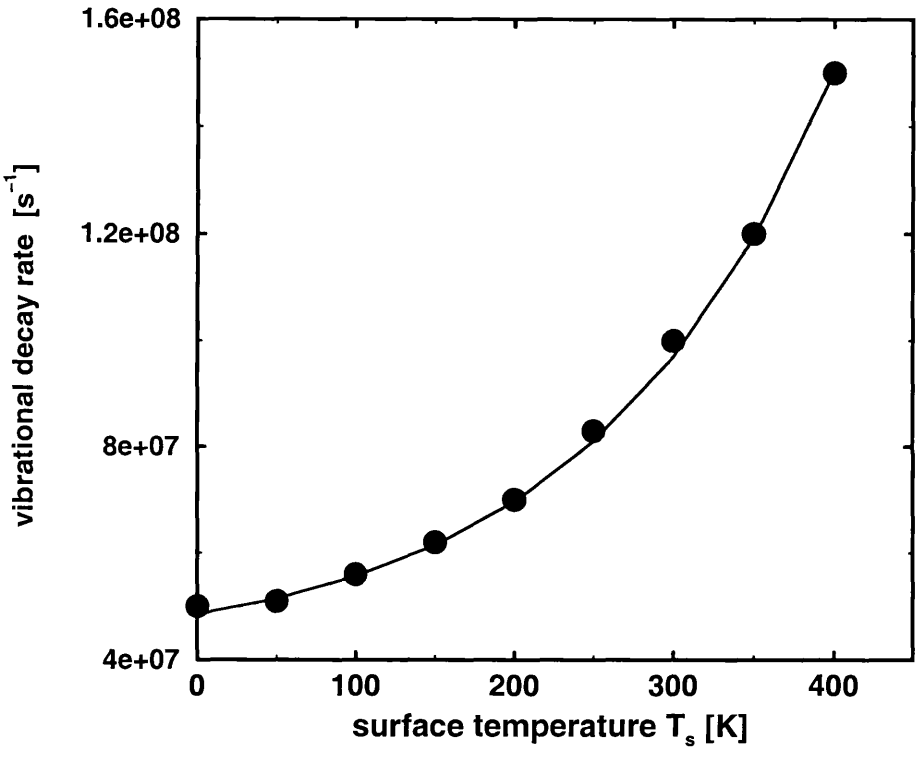

Figure 3.16: *The energy relaxation rate* $W_{0,1}^{diss}(T_s) = 1/\tau_{vib}(T_s)$ *of the SiH mode as calculated by Avouris et al. [72], showing an exponential temperature dependence. The vibrational quenching rates correspond to* $\tau_{vib} = 10$ *ns at 300 K and* $\tau_{vib} = 18$ *ns at 100 K.*

the effective barrier to be slightly lower ($\approx D - \hbar\omega_0/2$) than the bond dissociation energy D, because they considered the process not as typical desorption but atom transfer over a barrier and tunneling to a potential well associated with the tip. Their choice of $\Delta E = 3$ eV [18] corresponds to ≈ 12 bound states in the truncated harmonic oscillator.

The parameter λ in Eq.(3.49) is a "reduction" factor which is caused by the Förster transfer and ≤ 1. Both the vibrational quenching rate and the lateral energy diffusion rate are temperature-dependent (see above). Calculations of the energy transfer rate show a change of λ by less than a factor of 2 upon cooling for a typical Stark shift of 50 cm^{-1} of the SiH frequency [26, 72]. Therefore, the main factor that controls the temperature dependence of the desorption yield is the vibrational decay rate $W_{n,m}^{diss}(T_s)$.

While a nonlinear dependence of the desorption rate on the tunnel current ($\propto I^\eta, \eta > 1$) naturally arises from Eq.(3.49), the experimentally observed voltage dependence of the desorption yield should be accounted for by the fraction f_{in} of tunneling electrons scattering inelastically. Avouris et al. fitted the inelastic fractions f_{in} to the experimental desorption yields (e.g. $f_{in} = 7.6 \times 10^{-4}$ at 2 V and $f_{in} = 2.8 \times 10^{-3}$ at 3 V [18]) and found good agreement between the desorption rate computed with Eq.(3.49), shown in Fig.3.17, and the experimentally observed desorption yield. [18, 72].

3.4.5 Beyond the harmonic-linear approximation

Despite the success of the harmonic-linear model for the description of the STM-induced desorption in the "below threshold" limit, the process is virtually neither "harmonic" nor "linear". In a quantum mechanical wave packet description, an excited wave packet typically splits into parts, of which some reach the continuum and desorb while others remain trapped in the potential well. The trapped parts will vibrationally relax, while parts in the continuum (or very high on the vibra-

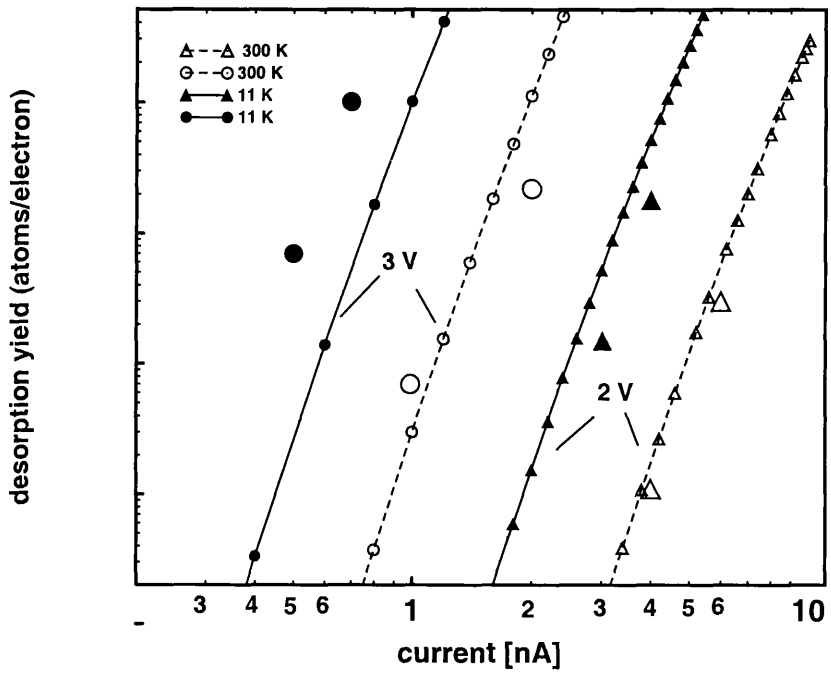

Figure 3.17: *STM induced DIMET of H form Si(100). Current dependence of the desorption yield for hydrogen with sample bias 2 and 3 V for* T_s *= 11 and 300 K. The lines are obtained by a truncated harmonic oscillator model with Eq.(3.49) and fitted values for the inelastic tunnel fractions:* $f_{in} = 7.6 \times 10^{-4}$ *at 2 V and* $f_{in} = 2.8 \times 10^{-3}$ *at 3 V [18]. The theoretical values are in good agreement with experimental data, represented by large circles (3 V, 300 K), bullets (3 V, 11 K) and triangles (2 V, filled for 11 K).*

tional "ladder") hardly feel the dissipative influence of the substrate. Therefore, the system-bath coupling has to be nonlinear at least in the system modes. Also, to allow for bond-breaking to occur, the system coordinates have to be anharmonic.

Thus, for a more rigorous description of the STM-induced desorption in the "below threshold" limit, an anharmonic (Morse) potential for the electronic SiH ground state and mostly nonlinear models to determine all transition rates numerically were chosen in this work. Furthermore, the sample bias, i.e., the applied electric field, has been implicitly included in the excitation/deexcitation rates and the fractions f_{in}^{dip} and f_{in}^{res} were determined numerically with generalised versions of Eqs.(3.32) and (3.36), rather than being fitted.

3.4.5.1 Inelastic tunneling rates

With generalised versions of Eqs.(3.32) and (3.36) for the fractions f_{in}^{dip} and f_{in}^{res}, the total energy transfer rate $W_{n,m}^{inel}$, which arises from inelastic scattering STM electrons, is given, according to Eq.(3.29), by

$$\begin{aligned} W_{n,m}^{inel} &= W_{m,n}^{inel} \\ &= \frac{I}{e} \cdot \left[\left(\frac{\langle v_n|\mu(Z)|v_m\rangle}{ea_0} \right)^2 + \frac{|V'_{res}(0)\langle v_n|Z|v_m\rangle|^2}{(V_{res}(0) - V_g(0) - eV)^2 + (\frac{\hbar\gamma(0)}{2})^2} \right. \\ &\quad \left. \cdot \frac{[V_{res}(0) - V_g(0) - eV + (\varepsilon_m - \varepsilon_n)]^2 - (\frac{\hbar\gamma(0)}{2})^2}{[V_{res}(0) - V_g(0) - eV + (\varepsilon_m - \varepsilon_n)]^2 + (\frac{\hbar\gamma(0)}{2})^2} \right] \quad . \end{aligned} \tag{3.50}$$

To get the transition rates $W_{n,m}^{inel}$ beyond the harmonic approximations, the matrix elements $\langle v_n|\mu(Z)|v_m\rangle$ and $\langle v_n|Z|v_m\rangle$ were computed numerically with $|v_n\rangle$ and $|v_m\rangle$ now being the vibrational eigenfunctions of the field-perturbed Hamiltonian Eq.(3.27).

To obtain the transition rates $W_{n,m}^{inel,res}$, the parameters $V_{res}(0)$ and $V'_{res}(0)$ were taken from Ref.[19] (see Table 3.4), as was also done for the estimate in section 3.4.4. In Eq.(3.36), the width of the resonance level is accounted for in the parameter γ,

which was also calculated by Stokbro et al. to $\gamma(0) = 1$ eV [19]. Because $|v_n\rangle$ and $|v_m\rangle$ are no longer eigenfunctions of the harmonic oscillator, the harmonic frequency $\hbar\omega_0$ has to be replaced by the difference $\varepsilon_m - \varepsilon_n$ of the vibrational energy levels of the Morse oscillator Eq.(3.5) as computed with the Hamiltonian Eq.(3.27).

No linear approximation was made for the dipole moment $\mu(Z)$ and the dipole function as given in Eq.(3.28) was used with the ab initio calculated permanent dipole moment μ_0 and the polarizability α (see section 3.3). Thus, the applied electric field, i.e. the sample bias, is explicitly included in the inelastic tunneling fraction f_{in}^{dip}. However, in regard to the more accurate calculations by Stokbro [100] and the most likely over-estimated dipole function calculated here (see section 3.4.3), the dipole function is from now on considered to be $\tilde{\mu}(Z) := 1/4 \cdot \mu(Z)$.

With the Morse potential given in Eq.(3.5), a SiH bond dissociation energy of $\sim$ 3.2 eV is obtained, which implies 25 bound states in the potential well (field-free case). As discussed in section 3.3, dissociation energy and number of bound states varies with the field strength. However, replacing μ by $\tilde{\mu}$ in the perturbation Hamiltonian Eq.(3.27) leads to less pronounced field effects so that N_b, the number of bound states, remains 26 for all bias investigated here. Additionally to the bound vibrational states, 69 continuum states were computed with the sinc function DVR method as in section 3.3 (for grid parameters see Table 3.4). Finally, transitions between non-nearest neighbour states were allowed.

As expected from the estimate in section 3.4.3, replacing μ by the more accurately calculated $\tilde{\mu}$ diminishes the transition rate $W_{n,m}^{inel,dip}$ drastically, but does not alter the "shape" of $W_{n,m}^{inel,dip}$ as function of the vibrational quantum number. This can be seen in Fig.3.18, exemplary for a sample bias of 2 V and a current $I = 1$ nA for transitions between states $|v_{n+1}\rangle$ and $|v_n\rangle$. The function shows a distinctive minimum around quantum number $n = 18$, which is due to the fact that the eigenfunctions with $n \approx 18$ are centred around a coordinate Z_k for which $\frac{d\mu(Z)}{dZ}|_{Z_k} \approx \frac{d\tilde{\mu}(Z)}{dZ}|_{Z_k} \approx 0$. This finding means that the desorption rate arising from the dipole mechanism would be zero if the selection rules would apply strictly, because no population could climb

high enough on the "vibrational ladder" to reach the continuum, i.e. desorb.

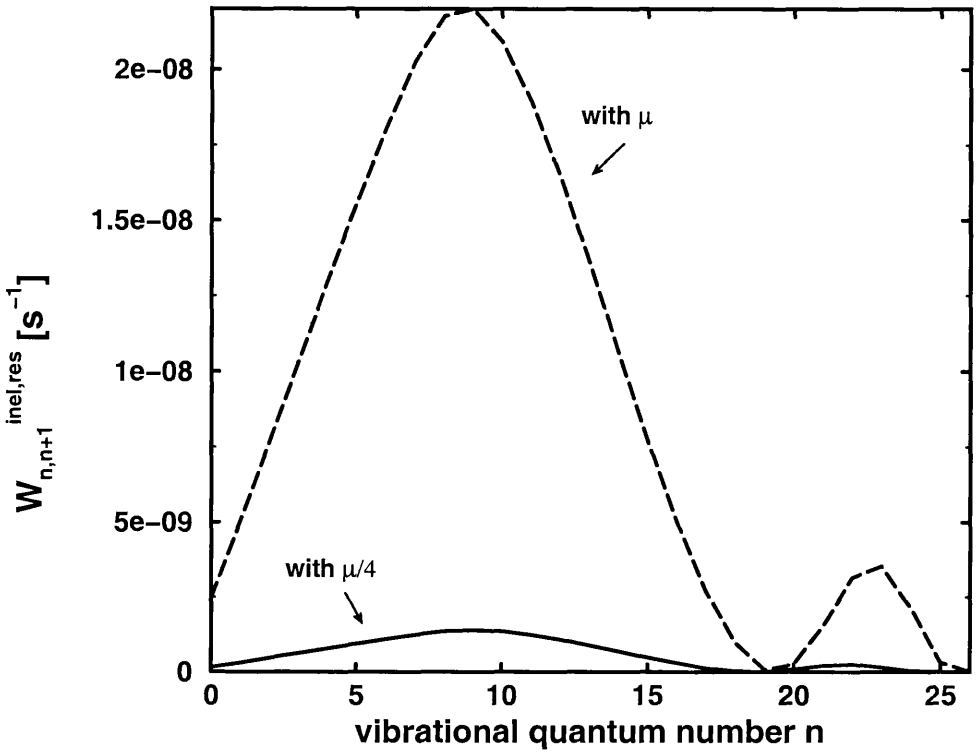

Figure 3.18: *The transition rate* $W^{inel,dip}_{n,n+1}$ *originate from tunneling electrons scattering inelastically due to the dipole mechanism, as obtained with Eq.(3.32) in the anharmonic-nonlinear model as a function of quantum number* n *for bias* $= 2V$ *and* $I = 1$ *nA. The values represented by the dashed line were obtained with the dipole function* $\mu(Z)$*, while the solid line shows* $W^{inel,dip}_{n,n+1}$ *as obtained with* $\tilde{\mu}(Z)$ *(see text).*

Grid parameters for sinc function DVR	
Grid spacings	$\Delta_Z = 0.05$ a_0 (for H and D)
Nb. of grid points	$N_Z = 1089$
Parameters for rate calculations [19, 26]	
Number of vibrational states considered	95
Resonance centered at	$V_{res}(0) = 4.6$ eV
Force $-dV_{res}/dZ\|_0$	$V'_{res}(0) = -3.12$ eV/Å
Resonance width	$\gamma(0) = 1$ eV
Parameters for Förster formula Eq.(3.43)	$\theta_0 = 1.4$ cm^{-1}
	$\kappa = 0.23$
	$\Delta\omega = 10$ cm^{-1}
	$\omega_s = 200$ cm^{-1}
Propagation parameters	
Number of vibrational states included	27
Newton interpolation propagation parameters	
Time step	$\Delta t = 2.4$ ps
Total propagation time	$t_f = 363$ ns
Polynomial order	$M = 16$

Table 3.4: *STM-induced DIMET on Si(100)-(2×1):H(D): Numerical parameters for the DVR grid, the excitation rates and for the direct density matrix propagation.*

The resulting rates $W_{n,m}^{inel,res}$ are shown in the lower panel of Fig.3.19 for bias 2 and 3 V (I = 1 nA) and transitions between states $|v_n\rangle$ and $|v_{n+1}\rangle$. They show a much stronger voltage dependence than the corresponding rates $W_{n,n+1}^{inel,dip}$, shown in the upper panel of Fig.3.19, and are much higher than those, consistently with the estimates made in section 3.4.4. In contrast to the inelastic dipole rates, the transition rates arising from the resonance mechanism increase monotonously up to $n = 23$, before $W_{n,n+1}^{inel,res}$ becomes negligible small.

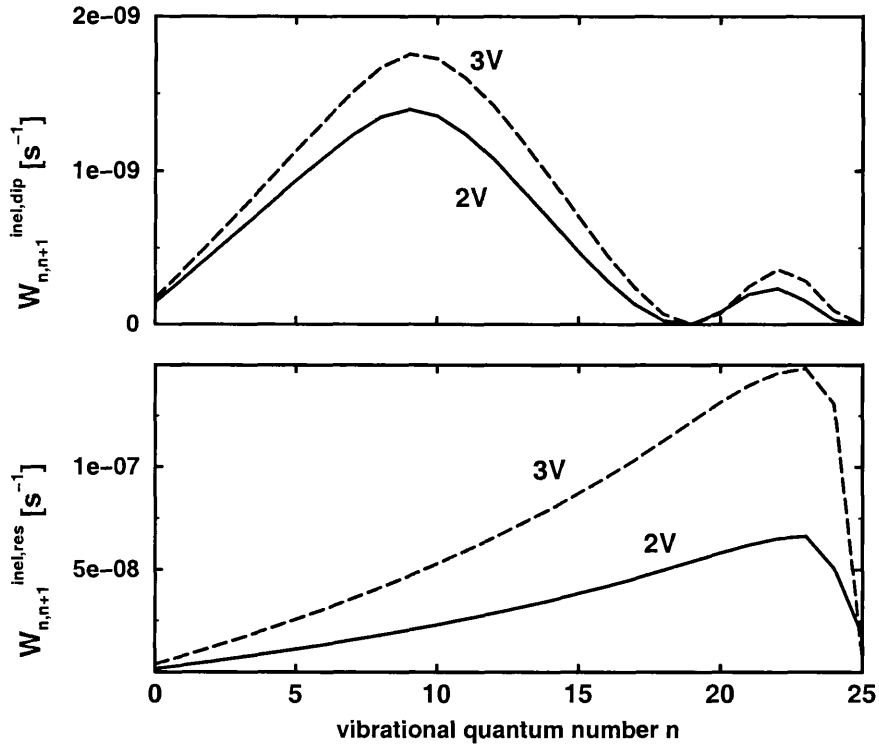

Figure 3.19: *The transition rates $W_{n,n+1}^{inel,dip}$ (upper panel) and $W_{n,n+1}^{inel,res}$ (lower panel) origin from inelastically scattering tunneling electrons, as obtained in the anharmonic model for a current I =1 nA and sample bias 2 V (solid lines) and 3 V (dashed lines). The transition rates arising from the resonance mechanism are much higher and show a stronger field (bias) dependence.*

In Fig.3.20, the total rates $W_{n,m}^{inel}$ origin from inelastically tunneling STM electrons are shown for vibrational transitions between $|v_n\rangle$ and $|v_{n+1}\rangle$ as a function of

vibrational quantum number n for bias 2 and 3 V ($I = 1$ nA). Because the contribu-

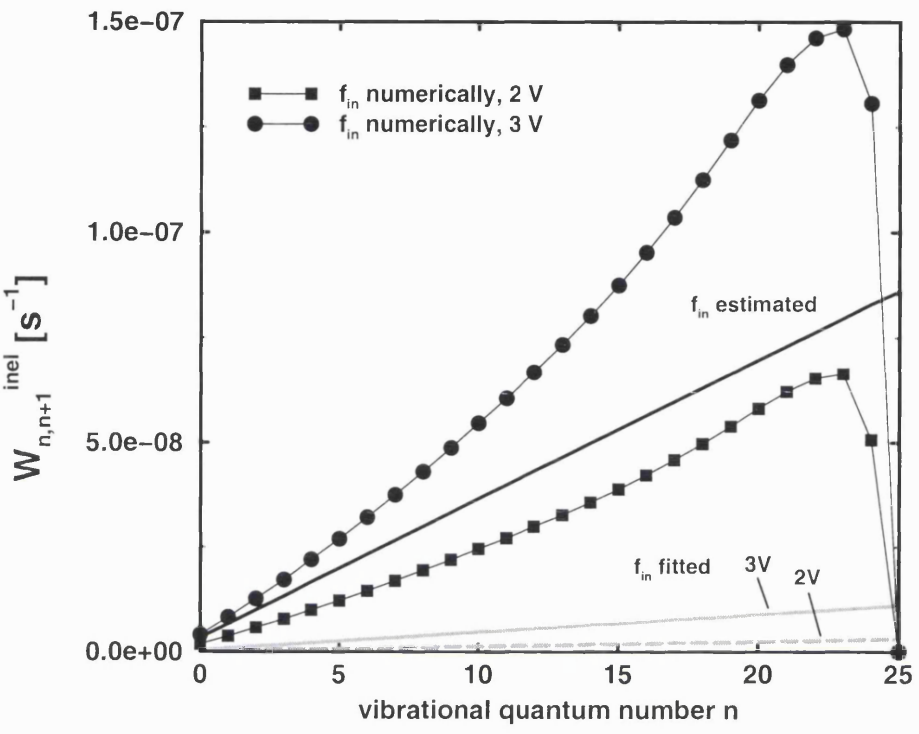

Figure 3.20: *The total anharmonic-nonlinear inelastic transition rates $W^{inel}_{n,n+1}$ as functions of vibrational quantum number n for bias 2 (squares) and 3 V (bullets) and current $I = 1$ nA. The grey lines represent harmonic-linear results with the fractions f_{in} in Eq.(3.39) fitted to experimental desorption curves (2 V: $f_{in} = 7.6 \times 10^{-4}$, dashed line; 3 V: $f_{in} = 2.8 \times 10^{-3}$ [18], solid line). The solid black line also gives harmonic-linear results, but with $f_{in} = 0.022$, as estimated in linear approximation (see section 3.4.3), presenting a good "average" of the anharmonic-nonlinear transition rates $W^{inel}_{n,n+1}$.*

tion from the resonance mechanism is so much higher than the dipole contribution, hardly any difference can be seen between the total rates $W^{inel}_{n,n+1}$ and the resonance rates $W^{inel,res}_{n,n+1}$ and the influence of $W^{inel,dip}_{n,n+1}$ looks negligible. To compare with the harmonic-linear models, different corresponding harmonic-linear rates are shown in Fig.3.20 as well. The grey lines correspond to $W^{inel}_{n,n+1}$ obtained with the truncated

harmonic oscillator and f_{in} fitted to the experimental results, as it was done by Avouris and co-workers (see section 3.4.4). These rates are notedly smaller than the inelastic rates $W^{inel}_{n,n+1}$ computed here and also much smaller than the harmonic rates $W^{inel}_{n,n+1}$ calculated with $f_{in} = 0.022$ as estimated in linear approximation in section 3.4.3 (solid black line). Those "estimated" $W^{inel}_{n,n+1}$, however, represents a good "average" of the anharmonic-nonlinear transition rates $W^{inel}_{n,n+1}$.

3.4.5.2 Dissipative rates

To model the vibrational energy decay due to substrate phonon coupling, an approach suggested by Nest and Saalfrank [103, 104] was used, which accounts for system anharmonicity and nonlinear system-bath coupling. Starting from a well established harmonic model with bilinear system-bath coupling [5], the authors replaced the harmonic creation and annihilation operators involved by the corresponding operators of a Morse potential and obtained the following expression for the vibrational decay rate

$$W^{diss}_{n-1,n} = W^{diss}_{0,1} \cdot \frac{\varepsilon_n - \varepsilon_0}{\hbar\omega_0} \quad . \tag{3.51}$$

$W^{diss}_{0,1}$ is the rate for the relaxation of system from its first vibrational excited state to its ground state and equal to the reciprocal, temperature dependent vibrational lifetime

$$W^{diss}_{0,1}(T_s) = 1/\tau_{vib}(T_s) \quad . \tag{3.52}$$

For the calculations, the vibrational lifetimes of SiH/SiD measured for 100 and 300 K by Guyot-Sionnest et al. [75] (see section 3.4.3) were taken rather than the much higher theoretical values of Avouris et al. (see section 3.4.4) and exponentials were fitted to get $W^{diss}_{0,1}(T_s)$ over the complete temperature interval [0 K, 400 K], as it was suggested in Ref.[72]. Because the measurements of τ_{vib} at 100 K were

[5] I.e., only terms linear in the SiH "system" and the Si(100) "bath" modes occur in the coupling operator $\hat{H}_{SB}$.

inconsistent, three different lifetimes were considered for the SiH vibrational mode at 100 K, namely $\tau_{vib} = 2.8$, 6.6 and 8.1 ns, while for 300 K $\tau_{vib} = 1.2$ ns was chosen. For SiD vibrational mode $\tau_{vib}(11\text{ K}) = 270$ ps was estimated from the experimental data (see section 3.4.3).

The resulting decay rates $W_{0,1}^{diss}$ for hydrogen as functions of the surface temperature T_s can be seen in the upper panel of Fig.3.21; they respectively correspond to $\tau_{vib} = 3.4$, 8.6 and 20 ns at $T_s = 11$ K. For comparison, $W_{0,1}^{diss}$ as obtained by Avouris (see also Fig.3.16) is marked as dashed grey line; indicating a much smaller vibrational decay rate.

In the lower panel of Fig.3.21, the dissipative decay rates $W_{n,n+1}^{diss}$ for surface temperature $T_s = 11$ K are shown (field-free case). As given by Eq.(3.51), the smaller the vibrational lifetime τ_{vib} and the higher the energy gap $(\varepsilon_n - \varepsilon_0)$, i.e., the higher the vibrational excitation, the higher the decay rate $W_{n,n+1}^{diss}$. An energy quenching rate proportional the vibrational quantum numbers n is also found in the harmonic-linear model (see Eq.(3.41)). However, the anharmonic-nonlinear rates level off for higher excited states, reflecting the fact the the coupling to the substrate phonons weakens with increasing distance to the surface. The straight dotted line in Fig.3.21 correspond to $W_{n,n+1}^{diss}$ as obtained by the harmonic-linear model with $W_{0,1}^{diss}(11\text{ K}) = 1/8.1$ ns. For small vibrational quantum numbers n, where the harmonic approximation is justifiable, the harmonic-linear rates $W_{n,n+1}^{diss}$ are in good agreement with $W_{n,n+1}^{diss}$ as calculated with the anharmonic-nonlinear model. The weakness of the harmonic-linear coupling model, however, lies in the prediction of a continual increase of the decay rates. This corresponds to a continual increase of the coupling strength, i.e. the further away from the surface the stronger the coupling to the substrate, a clearly unphysical behaviour.

Because the external electric field, i.e. the applied bias, only enters indirectly in Eq.(3.51) in the form of the eigenfunctions of the Hamiltonian Eq.(3.27), the field dependence of the dissipative decay rate is generally weak, as it is shown in Fig.3.22.

This is qualitatively different from what was found for the Förster transfer rate

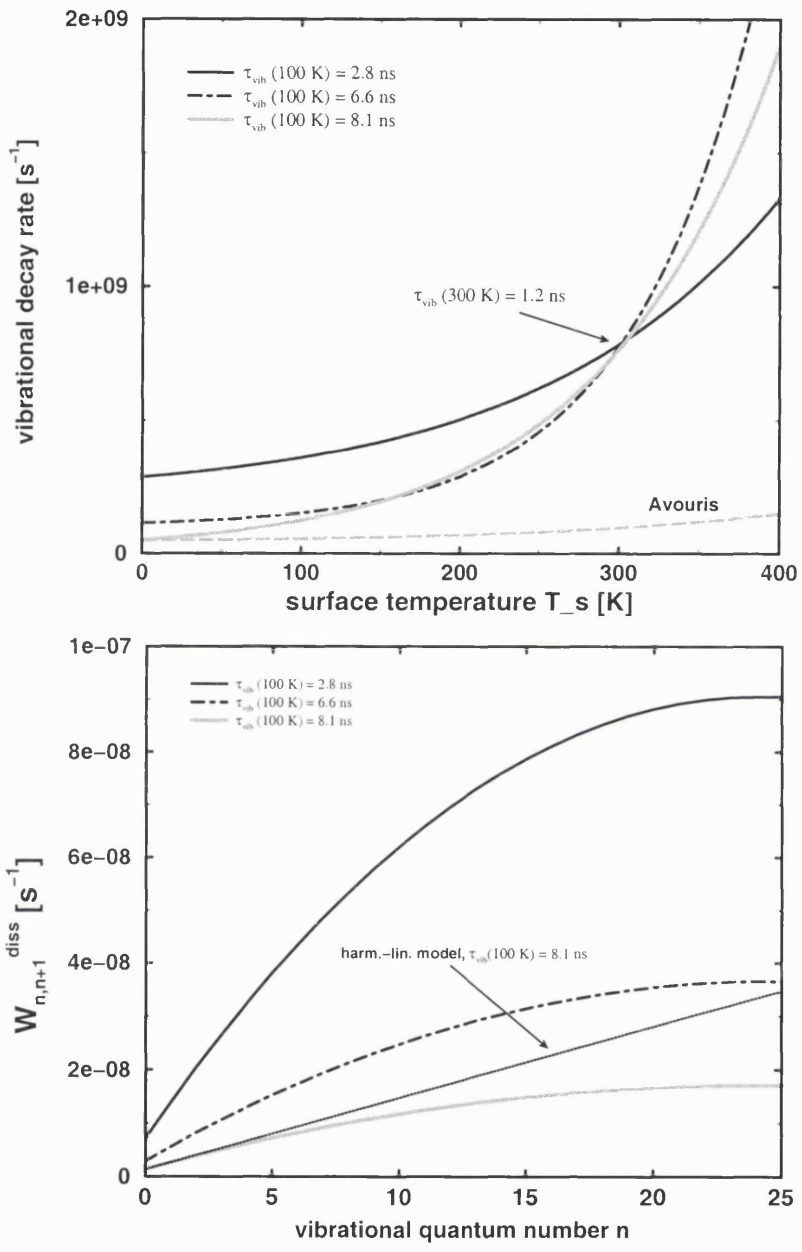

Figure 3.21: *The relaxation rates $W^{diss}_{0,1}$ for hydrogen as a function of the surface temperature T_s (upper panel). $\tau_{vib}(300\ K) = 1.2$ ns was chosen according to experimental results [75]. Three different lifetimes were considered for the SiH vibrational mode at 100 K (see text). For the thus resulting lifetimes at 11 K, $\tau_{vib} = 3.4$, 8.6 and 20 ns, the resulting total decay rates $W^{diss}_{n,n+1}(11K)$ are shown in the lower panel as functions of vibrational quantum number n, together with the harmonic-linear result for $\tau_{vib} = 8.6$ ns.*

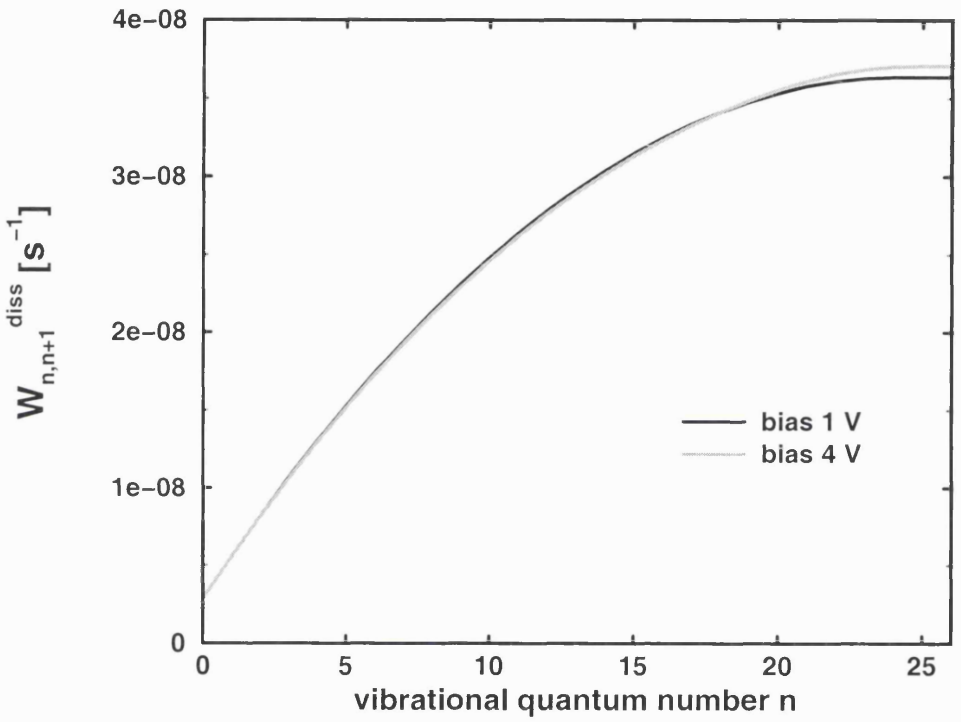

Figure 3.22: *Dissipative decay rate $W^{diss}_{n,n+1}$ for sample bias 1 (black line) and 4 V (grey line). Because the influence of the external field enters only through the eigenfunctions of the Hamiltonian Eq.(3.27), a weak voltage dependence of the dissipative decay rate is observed.*

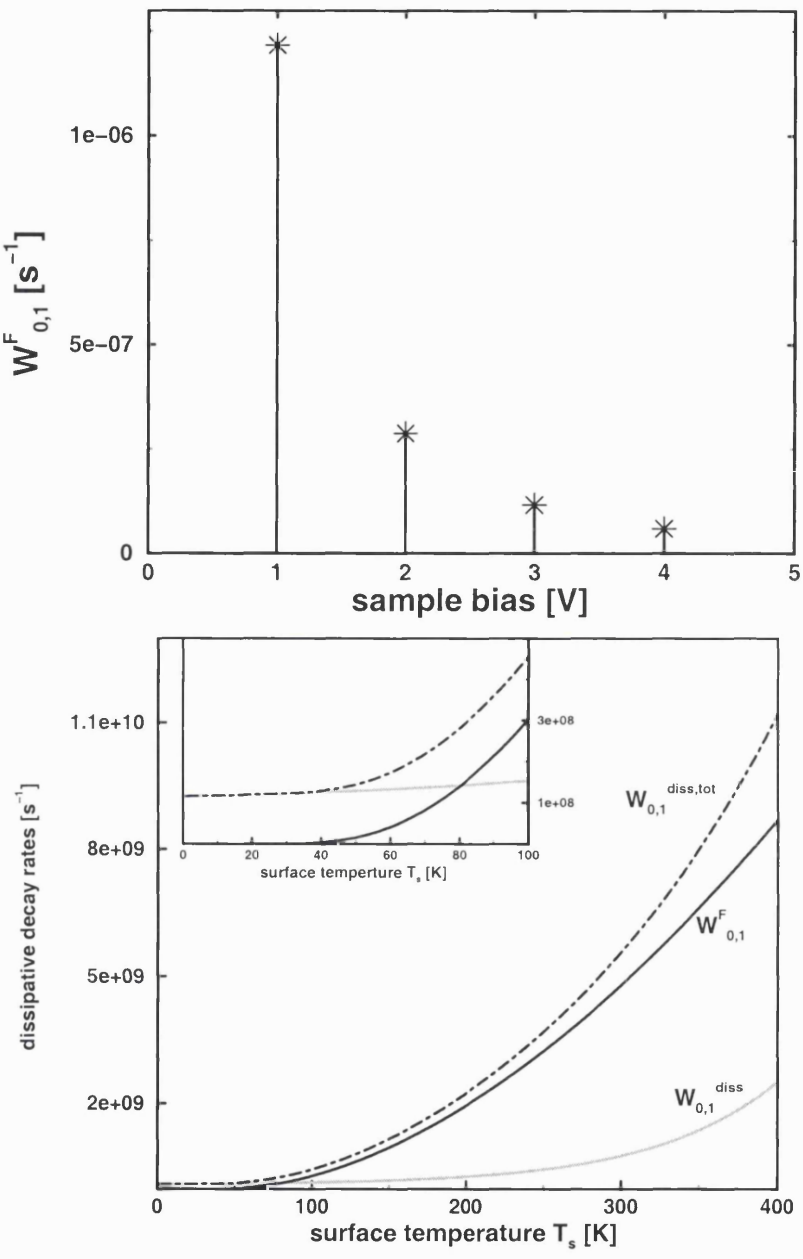

Figure 3.23: *Voltage dependence of the Förster transfer rate* $W^F_{0,1}$ *for* $T_s = 300$ *K (upper panel). The frequency shift* $\omega_0 \rightarrow \omega_F$ *gets larger with increasing voltage, thus diminishing the lateral energy transfer. The temperature dependence of the dissipative decay rates* $W^{diss}_{0,1}$ *and* $W^F_{0,1}$ *and the sum* $W^{diss,tot}_{0,1}$ *is shown in the lower panel (bias = 3 V). As it can be seen in the inserted blow-up, the Förster transfer rate is negligible for very low temperature, but changes the total energy decay rate drastically for temperatures* $T_s > 50$ *K.*

$W^F_{0,1}$, which was calculated according to Eq.(3.43) and Eq.(3.44) with the parameters as given in Ref.[26] (see Table 3.4). The field dependence enters quadratically through the field induced Stark shift, $(\omega_F - \omega_0)$, in the denominator of the Förster formula Eq.(3.43). The frequency shift $\omega_0 \rightarrow \omega_F$ gets larger with the strength of the applied electric field (see Table 3.3). This means an increasing shift of the SiH bond under the tip, away from the band of the other propagation SiH phonons. Thus, the lateral energy transfer is diminished with increasing electric field strength, as it is shown in the upper panel of Fig.3.23.

In the lower panel of Fig.3.23 , the temperature dependence of the Förster transfer rate is shown, exemplary for a sample bias = 3 V, as a function of the substrate temperature T_s (solid black line). Also shown is the corresponding vibrational energy decay rate $W^{diss}_{0,1}$ (solid grey line) and the resulting total dissipative decay rate $W^{diss,tot}_{0,1} = W^{diss}_{0,1} + W^F_{0,1}$ (dot-dashed black line). As it can be seen in the inserted blow-up, the Förster transfer rate is negligible for very low temperature, but changes the total energy decay rate drastically for temperatures $T_s > 50$ K.

So far calculations on the field-induced Stark effect (Refs.[86, 67, 26] and this work, see section 3.3) assumed that the STM tip has an ideal "one atom" structure, thus producing an electric field which is localized on a single adsorbate below the tip. However, this is not the case for real tip geometries. A tip curvature in the range of 100 - 1000 Å is usually found [105, 106] and it is generally assumed that the atomic resolution arises from a small protrusion or a single atom sticking out of the tip. Recently, Stokbro modelled the electric field under the STM tip for realistic tip structures and calculated the resulting vibrational SiH frequencies and Stark shifts, using density functional theory within the generalized gradient approximation and a slab with 12 Si atoms and 6 H atoms [100]. His calculations confirmed that a localized mode exists below the tip, but showed that it is not completely localized at a single site. With a more realistic tip geometry, the electric field right on top of an adsorbate is not very different from the nearest neighbour sites, allowing for a high diffusion rate to these sides. Therefore, Stokbro found that the decay of the

localized vibrational excitation due to the Förster transfer is about two orders of magnitude higher than the one obtained with the non-realistic tip geometry. Furthermore, Stokbro's calculations confirmed the suppression of energy diffusion from higher excited states ($n > 1$) due to the anharmonicity of the SiH bond potential (see section 3.4.3), justifying the inclusion of the Förster energy transfer just for transitions between states $|v_0\rangle$ and $|v_1\rangle$:

$$W^F_{n,m} = W^F_{0,1}\,\delta_{0n}\,\delta_{1m} \tag{3.53}$$

3.4.6 Desorption dynamics

3.4.6.1 Open system density matrix approach

In this work, the vibrational heating and the desorption dynamics of the STM induced hydrogen desorption from silicon in the "below threshold" regime were modelled within open-system density matrix theory. A dissipative Liouville - von Neumann equation of Lindblad form (Eq.(2.10)) was solved subject to the initial condition

$$\hat{\rho}_s(0) = |g\rangle\langle g| \otimes \sum_n w_n(T_s)|v_n\rangle\langle v_n| \quad , \tag{3.54}$$

where $|v_n\rangle$ is the n-th vibrational wave function in the electronic ground state and

$$w_n = e^{-(\varepsilon_n-\varepsilon_0)/k_BT_s} / \sum_n e^{-(\varepsilon_n-\varepsilon_0)/k_BT_s} \tag{3.55}$$

is the Boltzmann weight of state $|v_n\rangle$ at surface temperature T_s. The direct propagation scheme outlined in section 2.2.1 was used and all propagation parameters are given in Table 3.4. For all operators, a state representation was chosen. Vibrational excitations and de-excitations of vibrational states $|v\rangle$ were modelled with the Lindblad operators

$$\hat{C}_{m,n} = \sqrt{\Gamma_{m,n}}\,|v_m\rangle\langle v_n| \tag{3.56}$$

$$\hat{C}_{n,m} = \sqrt{\Gamma_{n,m}}\,|v_n\rangle\langle v_m| \quad , \tag{3.57}$$

where the relaxations and excitation rates Γ are given by

$$\Gamma_{n,m} = W^{inel}_{n,m} + W^{diss}_{n,m} + W^{F}_{0,1}\,\delta_{0n}\,\delta_{1m} \tag{3.58}$$

$$\Gamma_{m,n} = W^{inel}_{m,n} + \left[W^{diss}_{n,m} + W^{F}_{0,1}\,\delta_{0n}\,\delta_{1m}\right] \cdot e^{-(\varepsilon_m - \varepsilon_n)/k_B T_s} \tag{3.59}$$

with $W^{inel}_{n,m}$, $W^{diss}_{n,m}$ and $W^{F}_{0,1}$ as defined in Eqs.(3.50), (3.51) and (3.43).

The energy transfer was considered as irreversible as soon a continuum state was reached on the "vibrational ladder", i.e., population in the continuum was considered as desorbed. All 26 bound states of the SiH system were included in the propagation, but while the computation of the "up-" and "downward" rates comprised 69 continuum states (see above), just the first continuum state $|c_1\rangle := |c\rangle$ was explicitly considered in the propagation. The transition rates from a bound state $|b\rangle$ to all the regarded continuum states $|c_i\rangle$ were included by a summed rate, $\Gamma_{cb} = \sum_i \Gamma_{c_i b}$.

With the Hamiltonian Eq.(3.27) and the dissipative Liouvillian Eq.(2.11), the following expression thus results for the nuclear density evolution among the vibrational states (see Appendix B)

$$\langle v_n|\dot{\hat{\rho}}_s|v_n\rangle = \dot{\rho}_{s,nn} = \sum_{m\neq n} \Gamma_{n,m}\rho_{s,mm} - \rho_{s,nn}\sum_{m\neq n}\Gamma_{m,n} \tag{3.60}$$

and

$$\langle v_n|\dot{\hat{\rho}}_s|v_m\rangle = \dot{\rho}_{s,nm} = -\frac{i}{\hbar}(\varepsilon_n - \varepsilon_m)\rho_{s,nm} - \frac{1}{2}\sum_k(\Gamma_{k,n} + \Gamma_{k,m})\rho_{s,nm} \quad . \tag{3.61}$$

In the system considered, there are no initial coherences

$$\rho_{s,nm}(0) = \rho_{s,nm}(0)\delta_{nm} \quad . \tag{3.62}$$

In the Lindblad ansatz, coupling between the off-diagonal elements $\rho_{s,nm}$ and diagonal elements $\rho_{s,nn}$ can only arise by a direct coupling term in the Hamiltonian (see, for example, section 4). Because direct coupling was not considered here, the off-diagonal elements remain zero. Thus, a generalized Pauli master equation is obtained, where the first term on the right hand side of Eq.(3.60) models the gain

of population in state $|v_n\rangle$ from all other vibrational states $|v_m\rangle$, while the second one describes the population transfer from vibrational state $|v_n\rangle$ to the other states $|v_m\rangle$.

3.4.6.2 Desorption rates

The rate of desorbed atoms per electron was obtained by weighting the time evolution among the continuum state considered, $\langle c|\dot{\hat{\rho}}_s|c\rangle$, with the number of incident electrons per second. As shown in the following, all the different excitation and de-excitation rates influence the desorption yield.

In Fig.3.24, the current dependence of the desorption rate is shown for voltages 2 V in the upper panel and 4 V in the lower one, on a double logarithmic scale. The surface temperature T_s is 11 K and the results were obtained assuming $\tau_{vib}(11K) =$ 8.6 ns. The desorption yields show a strong current dependence and are significantly higher for the higher sample bias. Additionally to the desorption yields obtained including all inelastic and dissipative "upward" and "downward" rates (black solid line), the desorption rate under neglect of the dipole tunneling mechanism, i.e. $W_{n,m}^{inel} = W_{n,m}^{inel,res}$, is shown (dashed grey line). At the smaller voltage, the inclusion of $W_{n,m}^{inel,dip}$ leads to slightly higher desorption rates. At higher voltages, however, the resonance mechanism dominates even more, because $W_{n,m}^{inel,res}$ is not only significantly higher than $W_{n,m}^{inel,dip}$, but also shows a stronger voltage dependence (see section 3.4.5). Thus, the desorption rate calculated considering the resonance mechanism only is almost identical to the one computed with the total rate $W_{n,m}^{inel}$. The same observations were made for the other considered vibrational lifetimes at 11 K and for surface temperature $T_s = 300$ K, at it is shown in Fig.3.25.

At 300 K, the Förster type energy transfer becomes important, and the influence of $W_{0,1}^{F}$ on the desorption yield is notedly stronger than the one of $W_{n,m}^{inel,dip}$. As discussed in section 3.4.5, $W_{0,1}^{F}$ becomes smaller with increasing voltage. Thus, the difference in the desorption yields calculated with (black, dot-dashed line) and

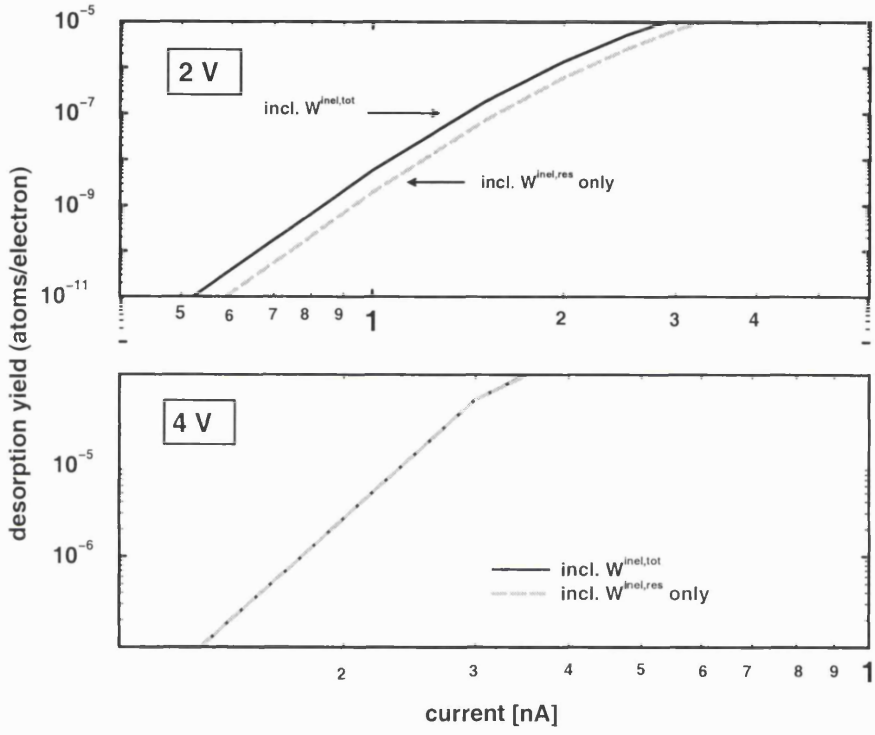

Figure 3.24: *STM induced hydrogen desorption from Si(100)-(2×1):H in the "below threshold" limit. The influence of* $W_{n,m}^{inel,dip}$ *on the desorption rate at different sample bias for* $T_s = 11\ K$, $\tau_{vib}(11K) = 8.6$ *ns. At the smaller voltage, the inclusion of* $W_{n,m}^{inel,dip}$ *leads to only slightly higher desorption rates. At the higher voltage, the desorption rate calculated considering the resonance mechanism only (dashed grey line) is almost identical to the one computed with the total rate* $W_{n,m}^{inel}$ *(solid black line).*

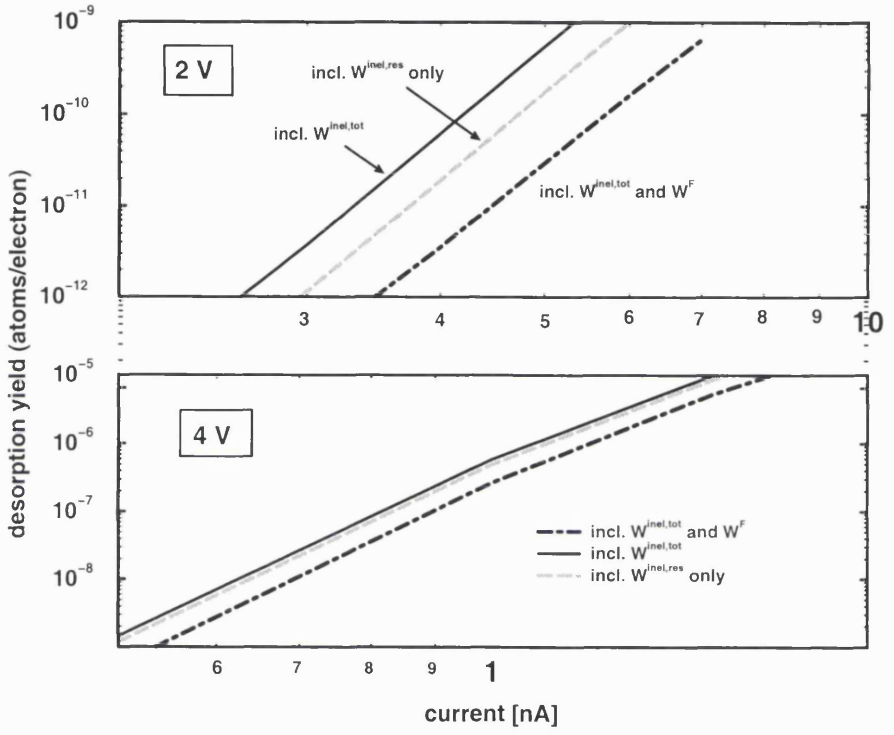

Figure 3.25: *STM induced DIMET of hydrogen from Si(100)-(2×1):H. The influence of* $W_{n,m}^{inel,dip}$ *and* $W_{0,1}^{F}$ *on the desorption yield at different sample bias for* $T_s = 300$ *K. Again, the influence of* $W_{n,m}^{inel,dip}$ *is minor, especially for the higher voltage. The inclusion of the Förster energy transfer rate* $W_{0,1}^{F}$ *has more notedly effect. With higher voltage, the difference in the desorption yields calculated with (black, dot-dashed line) and without (solid black line) the Förster energy dissipation becomes smaller, but is still pronounced.*

without (solid black line) the Förster energy dissipation becomes smaller (see lower panel of Fig.3.25), but is still pronounced due to the weak voltage dependence of $W_{n,m}^{diss}$.

The most significant influence on the desorption rate, however, has the vibrational lifetime included in $W_{n,m}^{diss}$, as it can be seen in Fig.3.26. For $T_s = 11$ K, where the experimental lifetime measurements for SiH were inconsistent [75] (see section 3.4.3), three different lifetimes, $\tau_{vib}(11K) = 3.4$, 8.6 and 20 ns, were considered. In accordance with the observations from section 3.4.5, the desorption yield is the higher the voltage and the longer the vibrational lifetime. In Fig.3.26, the desorption rates calculated for the truncated harmonic oscillator model with Eq.(3.49) and the values f_{in} as fitted by Avouris (see above) are indicated as grey lines (2 V: triangles; 3 V:bullets) to mark the approximate position of the experimental results (see section 3.4.4). As it can be seen, the yields computed including $W_{0,1}^{diss} = 1/20$ ns, i.e., with a vibrational lifetime close to the one estimated by Avouris et al. [72], fail completely; they are orders of magnitude higher than the experimentally observed desorption yields. Unfortunately, even with much lower lifetimes, i.e., much higher dissipative decay rates, the computed desorption yields are still too high compared to experiment.

For 300 K, $W_{0,1}^{diss} = 1/1.2$ ns was assumed, in agreement with the experimentally measured vibrational lifetime [75] (see section 3.4.3). However, for a sample bias of 2 V, the so obtained desorption yields are too high as well, as it can be seen in Fig.3.27, where the harmonic-linear results as approximate marks for the experimental data are also given as grey lines (2 V: triangles; 3 V: circles). The solid black lines represent the desorption yield computed with transition rates Γ as defined in Eqs.(3.58) and (3.59). The dashed lines give the desorption rate under the assumption of a 100 times higher Förster energy transfer rate, as it was calculated by Stokbro for a more realistic tip geometry[100] (see section 3.4.5). The higher dissipation rate leads to smaller desorption yields, thus bringing the rates calculated for 2 V closer to those observed experimentally. In contrast, for a sample

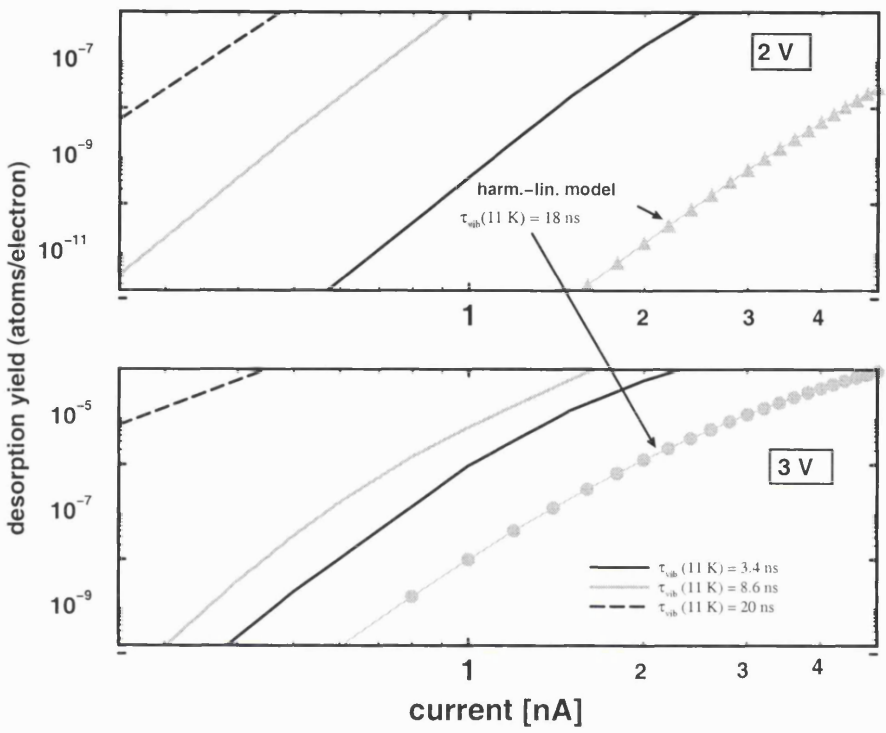

Figure 3.26: *STM induced desorption in the "below threshold limit". The influence of the vibrational lifetime on the hydrogen desorption rate from Si(100)-(2×1):H for T_s = 11 K and voltage 2 V (upper panel) and 3 V (lower panel). Because of inconsistent experimental measurements at low temperature, three different lifetimes, $\tau_{vib}(11K)$ = 3.4, 8.6 and 20 ns, were considered. The desorption yield is the higher the higher the voltage and the longer the vibrational lifetime. However, the computed desorption yields are generally higher than the experimental yields, symbolised by the harmonic rates obtained with Eq.(3.49) and the fitted fractions f_{in} (see text) and indicated as as grey lines (2 V: triangles; 3 V:bullets).*

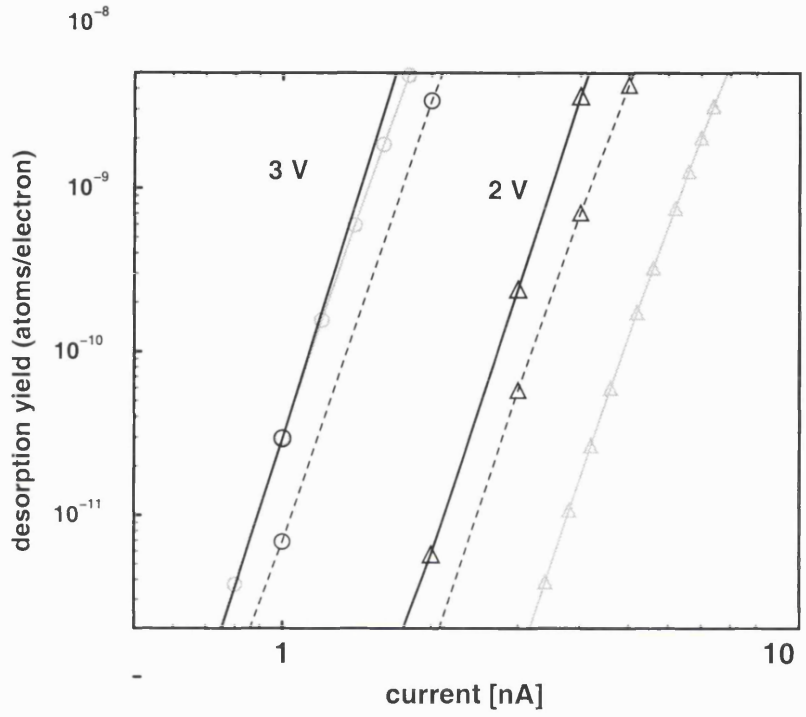

Figure 3.27: *STM stimulated DIMET of hydrogen from Si(100)-(2×1):H. The impact of the Förster energy transfer rate $W^F_{0,1}$ on the desorption yield and comparison with experimental results for T_s = 300 K, $\tau_{vib}(300K)$ = 1.2 ns. Given as approximate marks for the experimental data are the harmonic-linear results obtained with Eq.(3.49) and the values f_{in} fitted by Avouris (see text) as grey lines (2 V: triangles; 3 V: circles). For a sample bias of 2 V, the computed desorption rates are again notedly higher than the "experimental" results, but because of a too small voltage dependence of the anharmonic-linear rates, the yield calculated for 3 V seems in good agreement with it.*

bias of 3 V, the calculated desorption yields were already in good agreement with the harmonic-linear results, representing the approximate experimental values; the assumption of a higher Förster energy transfer rate leads to too small yields.

However, the fact that the desorption rates are too high for the smaller voltage, but seem correct for the higher bias indicates that the experimentally observed voltage dependence is not reproduced correctly in the transition models applied here. It can be assumed that with the correct voltage dependence the desorption yield calculated for 3 V will also be higher than the one experimentally observed. One reason for the too weak voltage dependence could be the quite roughly calculated, respectively estimated, dipole function $\tilde{\mu}(Z)$ entering in $W_{n,m}^{inel,dip}$. Nevertheless, the excitation (relaxation) rates caused by the dipole mechanism are much smaller than those of the resonance mechanism. So it is more likely that the problem arises from the dominating contribution $W_{n,m}^{inel,res}$, which is still modelled in linear approximation (see Eq.(3.36)). An improved, non-linear approach to resonant tunneling is clearly preferable, for reasons discussed above.

There are not many experimental data available for the "below threshold" deuterium desorption, just for a bias of 3 V and substrate temperature $T_s = 11$ K. The yield calculated with the anharmonic-nonlinear model is also higher than the one experimentally observed, but the isotope effect in the desorption yield is reproduced correctly. This is shown in Fig.3.28 for $T_s = 11$ K and a sample bias of 3 V (solid black line). The isotope effect is much higher than the one observed for desorption in the "above threshold" regime (section 3.2) and involves an isotope effect on the vibrational lifetime: the deuterium desorption yield is much smaller than the H yield because of the much shorter vibrational lifetime (see section 3.4.3). Again, the harmonic-linear result obtained with Eq.(3.49) is included (grey line) as approximative mark for the experimental values. Because deuterium desorption is experimentally not detectable for higher temperatures or smaller voltages, the deuterium yield calculated for 300 K can not be compared to experimental data. Nevertheless, the temperature dependence looks reasonable, considering the fact the

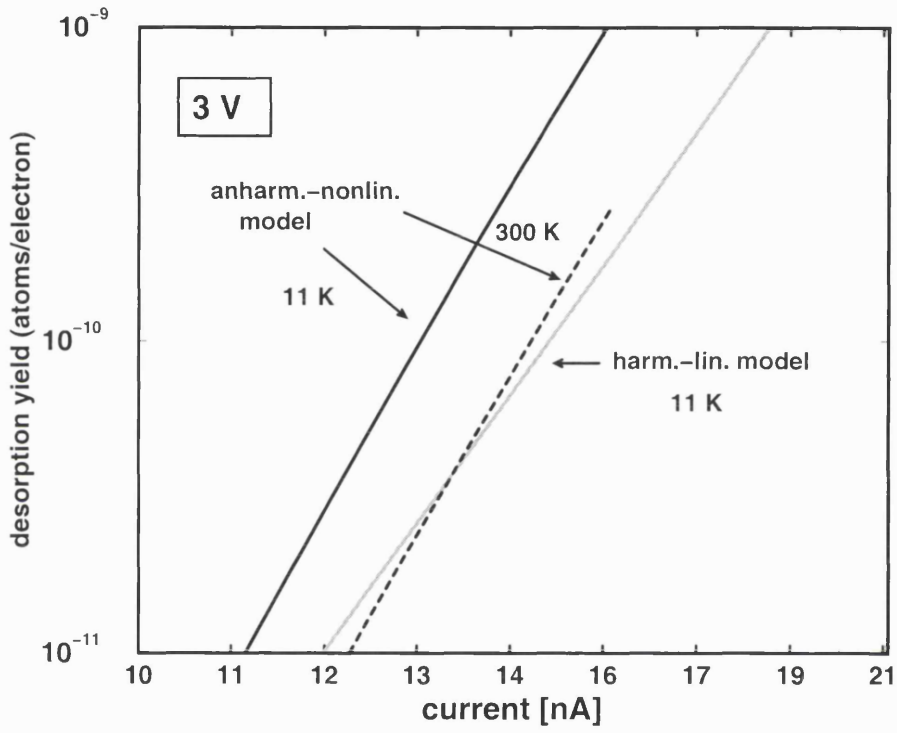

Figure 3.28: *STM induced deuterium desorption in the "below threshold" limit. Deuterium desorption is experimentally not detectable for higher temperatures, but the temperature dependence calculated here looks reasonable because the temperature dependence of the vibrational lifetimes is very weak for D;* τ_{vib} *= 270 ps at 11 K and 225 ps at 300 K [75].*

there is just a minor difference in the temperature dependent lifetimes: $\tau_{vib} = 270$ ps at 11 K and 225 ps at 300 K [75].

3.4.7 Summary and conclusions

The STM induced desorption dynamics of hydrogen and deuterium from Si(100) in the "below threshold" limit was investigated using an anharmonic, nonlinear 1D (N_b + 1) state model. For this, various factors responsible for vibrational excitation and relaxations were discussed and different theoretical approaches to model vibrational heating by inelastically scattering tunnel electrons were introduced.

The current dependence of the desorption rate was examined for different sample bias and surface temperatures, the influence of the vibrational lifetime and the Förster transfer on the desorption yield were investigated and isotope effects were addressed. It results that the most prominent factor to determine the desorption rate is the lifetime of the vibrational excitation, which is also the origin for the enormous isotope effect in the desorption yield.

With the anharmonic and nonlinear excitation model introduced in this work, the experimentally observed temperature and current dependence of the desorption rate can be reproduced, as well as the isotope effect in the desorption yield. However, the theoretical desorption rates are usually shifted to lower currents. This discrepancy can be due to different reasons. Presumably, the most critical point is the one dimensional modelling of the excitation/de-excitation processes. As seen above, the main factor that controls the desorption yield is the vibrational energy decay rate $W_{0,1}^{diss}$ and thus the vibrational lifetime τ_{vib}. The energy of the fundamental SiH vibrational mode is about 2000 cm^{-1}, so the only way the excitation can decay is by a multi-phonon process. It is most likely that the relaxation channel involves coupling to the SiH bending modes ($\hbar\omega_0 \sim 600 cm^{-1}$) as well as to substrate phonons ($\hbar\omega_0$ up to 520 cm^{-1}) [72, 107]. Thus, a description of the "vibrational heating" process and the eventual succeeding desorption in a 2 dimensional model seems

essential.

Another reason for the too high theoretical desorption rates – also observed by Stokbro et al. using a completely different theoretical modelling [19] – might be the basic assumption that the desorption process involves only one single SiH bond. Even if the experimental observations imply single H(D) desorption [73], it might happen that sometimes two H atoms from the same Si-dimer recombine and desorb as H_2 [68]. This is so far unaccounted for in the theoretical modelling here.

Concluding it can be said that the modelling of the complex process of desorption by multiple vibrational excitations with the manifold of excitation/relaxation mechanisms involved is a fruitful area for further research.

Chapter 4

Direct photoinduced desorption of H and D from a Si(100)-(2x1):H(D) surface [64]

4.1 Review of experimental results and related theoretical investigations

Recent experimental studies by Vondrak and Zhu [108, 109] showed that photo-excitation of the SiH bond on the Si(100)-(2x1):H surface at 157 nm leads to desorption of atomic hydrogen (deuterium). Quantitative measurements using polarized light demonstrated that the photo-desorption yield is related to the transition dipole moment of the SiH bond rather than the substrate absorbance. These observations indicate a direct coupling of the laser field to the transition dipole moment of the adsorbate system rather than an indirect excitation mechanism via the substrate. This is in contrast to UV/Vis laser experiments on metal surfaces, where nearly all photodesorption studies point to an indirect mechanism [11, 110, 111, 112].

The 7.9 eV photon energy of 157 nm laser light coincides approximately with the energy for the $\sigma \rightarrow \sigma^*$ transition of the SiH bond on Si(100), which is believed to

be responsible for the electron induced desorption of H and D in STM experiments in the "above threshold limit" (section 3.2). For the optical excitation of a $\sigma \rightarrow \sigma^*$ transition, the transition dipole moment should lie along the bond direction, which was indeed verified in the polarization measurements of Vondrak and Zhu [108, 109].

In the experiments laser desorption experiments [108, 109], a large isotope effect in the photodesorption yield

$$I_{des} = \frac{P_{des}(H)}{P_{des}(D)} \tag{4.1}$$

of 10±3 was observed. In the STM studies of electron-induced desorption of H and D from the same surface, Avouris et al. estimated the isotope ratio $I_{des} \approx 50$ for the desorption induced by field-emitted electrons with energies greater than $\approx$ 6 eV [18]. Vondrak and Zhu [108, 109] as well as Avouris et al. [17] carried out quantum dynamical calculations for zero surface temperature, both with an MGR type model and potentials based on ab initio cluster calculations [29]. These calculations explained the large isotope effect in the desorption yield by assuming an ultrashort excited state lifetime τ of less than 1 fs. For both experiments, the theoretical modelling was essentially the same, since the excitation leading to a DIET process was always treated as an initial Franck-Condon transition, i.e., no specifics of the STM or the laser entered the formalism.

In this work, DIET of H and D from Si(100)x(2x1) was also investigated (section 3.2). In addition to the earlier works by Avouris et al. [17, 29] and by Zhu and Vondrak [108, 109], it was demonstrated that a coordinate-dependent electronic relaxation ($\tau = \tau(Z)$ with $\lim_{Z\rightarrow\infty} \tau(Z) = \infty$) leads to increased desorption probabilities P_{des}. For coordinate-independent electronic quenching, an approximate semiclassical expression for the isotope effect was derived (see Eq.(3.20)):

$$I_{des} = e^{-\lambda/\tau} \tag{4.2}$$

with λ being related to the excited state potential parameters and the masses of H and D respectively.

In principle, both the laser and the STM experiment should involve the same $\sigma \rightarrow \sigma^*$ transition, making the large difference in the observed isotope ratios difficult to understand. However, the analytic expression Eq.(4.2) and the further results obtained in section 3.2 demonstrate that the isotope ratio I_{des} increases exponentially with decreasing excited state lifetime τ. Hence, for ultrashort lifetimes, already tiny differences in τ (or λ) will cause enormous differences in the ratio I_{des}, as it is shown in Fig.3.3. Thus, even smallest differences in the experimental conditions may lead to large differences in the observed isotope ratio. This is a tentative explanation for the quantitatively different isotope effects observed in the photo- and electron-induced DIET experiments by Zhu et al. and Avouris et al. respectively.

The aim of the following investigations was the active control of the photodesorption outcome. One of the best known reaction control strategies in photochemistry is *optimal control theory* [113, 114, 115] which involves specially shaped laser pulses, i.e. optimal electromagnetic fields in terms of spectral and temporal compositions for the reaction considered. However, this was developed for photochemistry in the gas phase and the application of optimal control theory in the condensed phase is non-trival. One reason for this is the difficulty of treating multi-mode problems, in particular on the quantum level of theory. Other problems are connected with the ultrafast decay of the electronically excited states. But above all, optimal control theory often requires a propagation backwards in time and the Liouville - von Neumann equation for open quantum systems is not time reversal invariant.

For these reasons, optimal control theory is not applied in this work, but the use of high-intensity fs lasers is proposed rather than the low-intensity ns lasers as in the experiments [108, 109] to control the desorption of H(D) from Si(100). Influencing the desorption yield and possible isotope effects may be possible by varying the fs laser parameters to an extent which is less possible when long-pulse lasers with low intensities are used. This hypothesis is investigated theoretically with the help of quantum dynamical model simulations within Markovian open system density matrix theory.

4.2 Desorption dynamics

The desorption has been modelled within the same MGR model and the potentials introduced in section 3.2.2 for the STM induced process in the "above threshold" (DIET) regime. For the theoretical description of the laser-induced desorption dynamics, a direct coupling model is adopted to simulate the laser excitation and a coordinate-dependent electronic decay rate is assumed, if not stated otherwise.

The system Hamiltonian in the Liouville-von Neumann equation (2.10) is now chosen as

$$\hat{H}_s = \hat{H}_g|g\rangle\langle g| + \hat{H}_e|e\rangle\langle e| + V_{ge}|g\rangle\langle e| + V_{eg}|e\rangle\langle g| \quad . \tag{4.3}$$

Whilst the diagonal blocks of $\hat{H}_s$ are the same as in Eq.(3.4), the off-diagonal elements now induce direct transitions between the electronic states. Here, only transitions stimulated by an electric field are included, and for the adsorbate-field coupling the semiclassical dipole approximation is made:

$$V_{eg} = V_{ge} = -\mu_{eg}(Z) \cdot E(t) \tag{4.4}$$

where $\mu_{eg}(Z)$ is the component of the transition dipole moment parallel to the adsorbate-surface bond and $E(t)$ the external electric field assumed to be polarized along the same direction.

The field is chosen as:

$$E(t) = E_0 \cdot s(t) \cdot cos(\omega t) \quad . \tag{4.5}$$

Here, ω is the laser carrier frequency and $s(t)$ is the shape function, for which two half Gaussians (eventually separated by a plateau region) are chosen:

$$s(t) = \begin{cases} e^{-(t-t_0)^2/(2\sigma^2)} & \text{for} \quad t \leq t_0 \\ 1 & \text{for} \quad t_0 \leq t \leq t_0 + t_{pla} \\ e^{-(t-t_0-t_{pla})^2/(2\sigma^2)} & \text{for} \quad t \geq t_0 + t_{pla} \quad . \end{cases} \tag{4.6}$$

Finally, the Condon approximation is made, i.e., the coordinate-dependence of the

transition dipole moment $\mu_{eg}(Z)$ is neglected in Eq.(4.4). In this way, the product $-\mu_{eg} \cdot E_0$ can be interpreted as a coordinate-independent coupling amplitude A_0.

This ansatz results in four laser parameters (the amplitude A_0, the width parameter σ, the plateau time t_{pla} and the frequency ω) which can be varied independently. The Gaussian peak time parameter t_0 (time for which the pulse becomes maximal) is selected so that for a given σ the field is practically zero at $t = 0$.

Dissipation is treated within the Lindblad semi-group approach and enters again through the coordinate-dependent Lindblad quenching operator $\hat{C}$ defined in Eq.(3.9). Possible indirect excitations through the substrate are assumed to be negligible, following Zhu's experimental observations of a direct excitation mechanism (see above).

As in section 3.2, all operators are represented on an equidistant, spatial grid in Z and the FFT algorithm is used to calculate the kinetic energy (see also appendix A). For the photo-induced desorption in the H/Si(100) system, the Liouville-von Neumann equation (2.10) was solved numerically subject to the initial condition

$$\hat{\rho}_s(0) = |g\rangle\langle g| \otimes |0_g\rangle\langle 0_g| \quad , \tag{4.7}$$

by the direct density matrix propagation scheme introduced in section 2.2.1. All calculations were carried out for zero temperature. The grid and propagation parameters are the same as the one for the direct density matrix propagation in section 3.2, except that the propagation time step Δt, which because of the fast oscillationg electric field involved was chosen to be smaller, namely $\Delta t = 2\,\hbar/E_h \approx 0.05$ fs. The total propagation time t_f depends on the duration of the laser pulse.

The time resolved desorption probability can be calculated from

$$P_{des}(t) = tr\{h(Z - Z_c)\hat{\rho}_s(t)\} \quad , \tag{4.8}$$

where $h(Z - Z_c)$ is a step function which is zero for $Z < Z_c$ and 1 for $Z \geq Z_c$ (see section 3.2.3). The observable desorption probability P_{des} itself is given by $P_{des} = \lim_{t\to\infty} P_{des}(t)$. The numerical propagation of the density matrix is rather costly and convergence to the point where $P_{des}(t) \to P_{des}$ can be slow. Additional problems

can arise by reflection phenomena. The set of basis functions for the density matrix propagation is built by just 512 grid points with the maximum possible [1] grid spacing Δz, i.e. the grid is relatively short. A larger grid corresponds to more basis functions L and because the memory required for a direct propagation of the density matrix scales $\propto L^2$, a direct propagation scheme then becomes unfortunately technically hard to realize.

To optimise convergence towards the final P_{des}, a new ansatz to obtain the final desorption probability was chosen:

$$P_{des} = \lim_{t\to\infty}[1 - N_g^b(t)] \tag{4.9}$$

where $N_g^b(t)$ is the sum of the populations of all n_b vibrational bound states in the electronic ground state. Here,

$$N_g^b(t) = \sum_{v_g=0}^{n_b-1} tr\{\hat{\rho}_s(t)|v_g\rangle\langle v_g|\} \tag{4.10}$$

with $tr\{\hat{\rho}_s(t)|v_g\rangle\langle v_g|\}$ being the population of the vibrational state $|v_g\rangle$.

For hydrogen and a laser pulse with parameters $A_0 = 0.0145\ E_h$, $t_0 = 1500\ \hbar/E_h$, $\sigma = 400\,\hbar/E_h$ and $\omega = 0.268\ E_h/\hbar$ respectively, the results obtained by Eq.(4.8) and Eq.(4.9) are compared in Fig.4.1. With both Eq.(4.8) and Eq.(4.9), $P_{des} = 8.4 \times 10^{-3}$ is obtained after a certain propagation time $P_{des} = 8.4 \times 10^{-3}$. The desorption probability $P_{des}(t)$ (black dashed line) starts to increase after a time $t \approx 2000\,\hbar/E_h = 43$ fs and reaches the final P_{des} after $\approx 5500\,\hbar/E_h = 133$ fs (see blow-up in the inset of Fig.4.1). In contrast, $[1 - N_g^b(t)]$ (solid grey line in Fig.4.1) passes a maximum at $\approx 1500\,\hbar/E_h = 36$ fs before it reaches it final value P_{des} after less than $3000\ \hbar/E_h = 72$ fs. Fig.4.1 shows clearly where the main advantage and disadvantage of the use of Eq.(4.9) lies: the "convergence" towards the final value for the desorption probability is indeed much faster, i.e. a lot of propagation time (almost 50% in the above example) can be saved. However, all information

[1] "possible" in respect to the evaluation of the kinetic energy; Δz dependes on the shortest resolvable De Broglie wave length (see section 3.2.2 and 5.3)

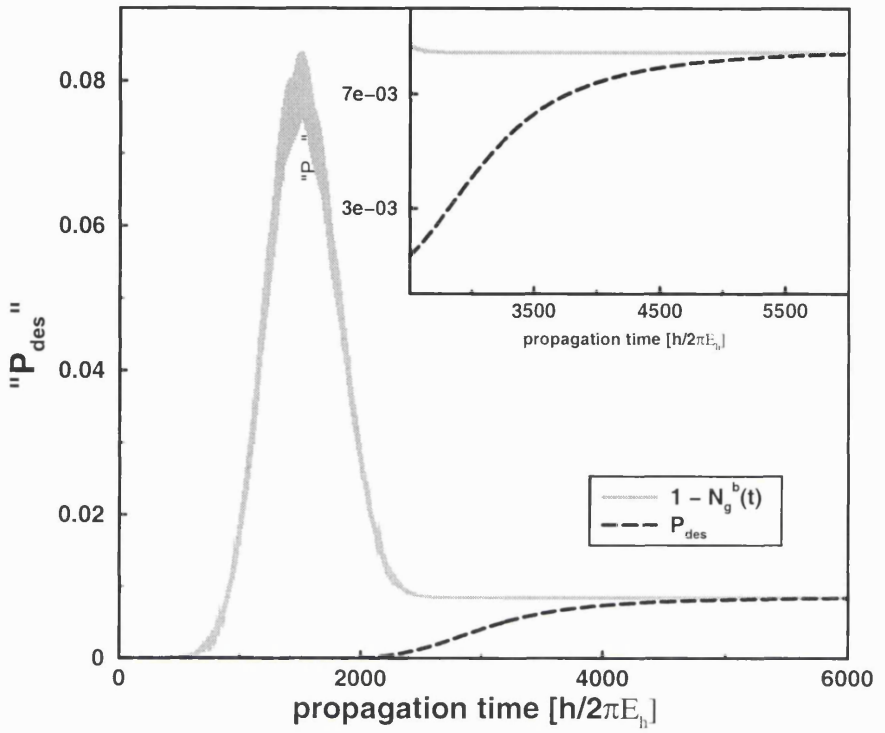

Figure 4.1: *Comparison of the "desorption probabilities" obtained by Eq.(4.8) (black dashed line) and Eq.(4.9) (solid grey line), exemplary for hydrogen and a laser pulse with parameters* $A_0 = 0.0145\ E_h$, $t_0 = 1500\ \hbar/E_h$, $\sigma = 400\,\hbar/E_h$ *and* $\omega = 0.268\ E_h/\hbar$. *The inset in the top right corner is a blow-up. One sees that the respective final values are reached after* $\approx 5500\,\hbar/E_h = 133$ *fs using Eq.(4.8) and after less than* $3000\ \hbar/E_h = 72$ *fs using Eq.(4.9).*

concerning the time-evolution of P_{des} is lost and no predictions about how long it will take the particles to leave the surface are possible.

4.3 Nanosecond laser desorption

The photodissociation of molecules with low-intensity cw lasers can be modelled within a sudden-transition excitation model [116]. A similar sudden-transition DIET model is used here to compare to the nanosecond lasers experiments of Zhu et al. [108, 109]. As the laser-excitation is not explicitly accounted for, this model is

analogous also to the treatment of the STM-induced "above threshold" desorption in section 3.2. Assuming a coordinate-independent excited state lifetime of $\tau = 0.75$ fs, a desorption probability of 2.4×10^{-3} is obtained for hydrogen and 2.0×10^{-4} for deuterium. This corresponds to an isotope ratio $I_{des} = 12$, which is close to that observed experimentally [108, 109].

It is shown in section 3.2 that the assumption of the electronic decay as coordinate-dependent is important for the SiH sudden-transition DIET model. Therefore, the coordinate-dependence of the excited state lifetime should also be included here. As it was suggested on the basis of Refs.[78, 117] (see also section 3.2.4), the range parameter γ in Eq.(3.10) is chosen to be 1.4 a_0.

If the excitation quenching is considered as dependent on the adsorbate-surface distance Z, $\Gamma_0 = 1/\tau$ in Eq.(3.9) must become larger, about 1/0.4 fs, to reproduce the experimentally observed isotope effect of 10 ± 3. This is because the yield obtained using a coordinate-dependent decay rate is about 35 times larger than in the coordinate-independent case (Fig.4.2), for reasons discussed in section 1.4) and in general, larger yields are associated with smaller isotope ratios and vice versa.

However, even if the desorption rates are generally much larger if one assumes a coordinate-dependent quenching process in the MGR model, the desorption probabilities for the shorter lifetimes are naturally smaller. Thus, for an excited state lifetime of $\tau = 0.4$ fs $P_{des}(H) = 1.85 \times 10^{-3}$ and $P_{des}(D) = 1.73 \times 10^{-4}$ are obtained. The lifetime $\tau = 0.4$ fs was used in the following calculations, since it provides an isotope effect $I_{des} \approx 11$ and so reproduces the experimental observed isotope ratio.

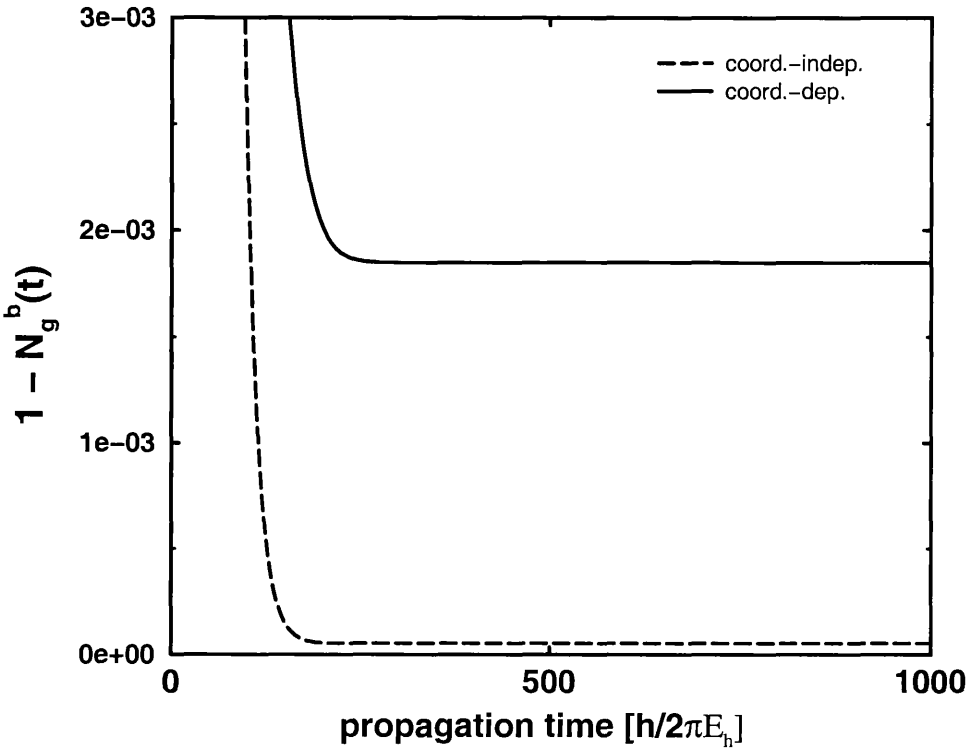

Figure 4.2: *Photoinduced DIET of H from Si(100)-(2x1). Shown is the function* $[1 - N_g^b(t)]$ *for hydrogen as obtained with a coordinate-independent electronic relaxation rate (dashed line,* $\Gamma = \Gamma_0 = 1/0.4$ *fs in Eq.(3.9)) and assuming a coordinate-dependent electronic decay (solid line,* $\Gamma_0 = 1/0.4$ *fs and* $\gamma = 1.4$ a_0 *in Eq.(3.9)). The desorption probability* $P_{des} = \lim_{t\to\infty}[1 - N_g^b(t)]$ *obtained with the coordinate-dependent model is about 35 times larger.*

4.4 Towards optimal femtosecond laser pulses

In order to enhance the desorption probability for the photo-induced desorption of hydrogen from Si(100)-(2x1) and to perhaps control the isotope ratio, the laser pulse parameters ω, A_0, σ and t_{pla} were partly optimized. Unfortunately, these calculations are quite costly, hence a complete and systematic variation of the full parameter space can not be presented here. Nevertheless, basic trends are clearly obvious.

4.4.1 Variation of the carrier frequency

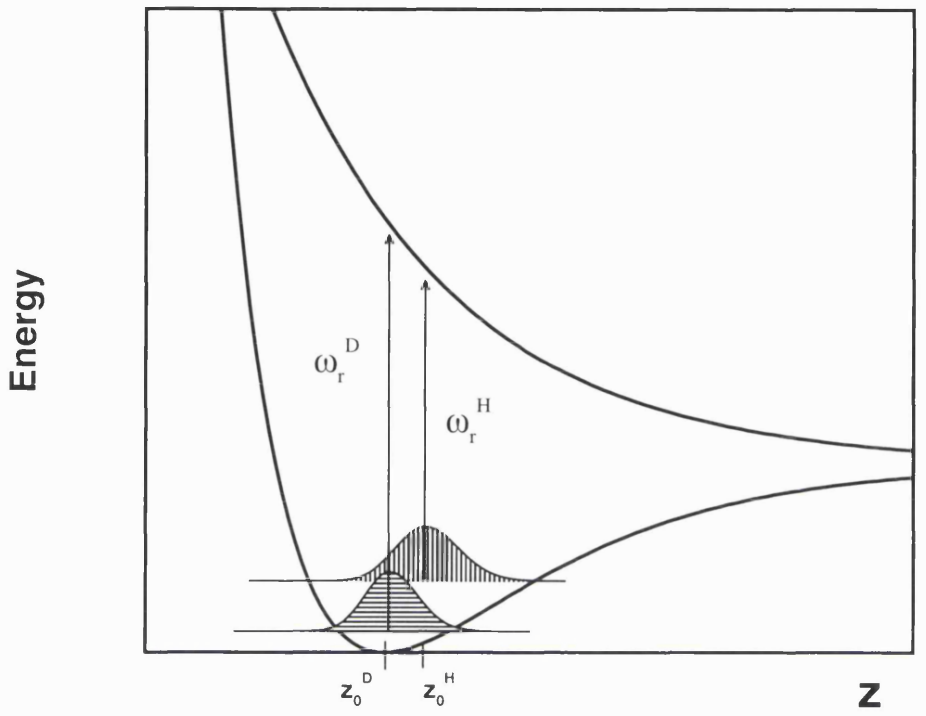

Figure 4.3: *Sketch of the initial wave functions of the two isotopes. Initially, the centre-of mass position* $\langle v_g|Z|v_g\rangle$ *of the hydrogen wave function (sketched with vertical lines) is at larger* Z *than the centre-of mass of the deuterium wave function (sketched with horizontal lines). Marked as arrows are the resulting resonance frequencies,* $\omega_r^H < \omega_r^D$*, for the photodesorption of H and D from Si(100).*

To optimise the laser carrier frequency ω, first excitation with a simple Gaussian pulse without a plateau region was modelled. While ω was varied between 0.230 $E_h/\hbar$ and 0.270 $E_h/\hbar$ in steps of $\Delta\omega = 0.005\, E_h/\hbar$, the other laser parameters were kept fixed:

- $\sigma = 400\, \hbar/E_h$
- $A_0 = 0.145\ E_h$
- $t_0 = 1500\ \hbar/E_h$

The choice of these parameters follows a pulse optimisation for the dissipation-free case in Ref.[64], where it leads to a desorption probability of ≈ 1 for a carrier frequency $\omega = 0.262 E_h/\hbar$.

Due to the higher mass of deuterium, the vibrational ground state of D has a lower energy ($\varepsilon_{0g}^D = 0.09$ eV) than the one of hydrogen ($\varepsilon_{0g}^H = 0.12$ eV) and thus, due to the vibrational anharmonicity of the system, the initial centre-of mass position $\langle v_g|Z|v_g\rangle = Z_0$ of deuterium is at a slightly shorter Z than $|0_g\rangle$ of hydrogen. This implies different optimal resonance frequencies ω_r for the two isotopes, pictured schematically in Fig.4.3. With $Z_0^H = 0.029\, a_0$ and $Z_0^D = 0.018\, a_0$, one can estimate for ω_r (see Fig.3.1):

$$\begin{aligned} \hbar\omega_r^H &= V_e(Z_0^H) - \varepsilon_{0g}^H = 0.262 E_h = 7.13 eV \\ \hbar\omega_r^D &= V_e(Z_0^D) - \varepsilon_{0g}^D = 0.265 E_h = 7.20 eV \end{aligned}$$

However, as it can be seen from Fig.4.4, the desorption yield for both isotopes actually reaches a maximum for carrier frequencies ω_r smaller than expected, namely $P_{des}(H) = 8.115 \times 10^{-3}$ at $\hbar\omega_r = 0.245\, E_h$ and $P_{des}(D) = 1.064 \times 10^{-4}$ at $\hbar\omega_r = 0.250\, E_h$ for deuterium. This indicates that the main excitation cross-section is at a larger distance Z, where the corresponding resonance frequency ω_r is smaller (see Fig.4.3).

These desorption probabilities for the fs laser excitation are clearly larger than the desorption probabilities for the ns laser DIET case, which were for the same lifetime τ (and the same range parameter γ) $P_{des}(H) = 1.85 \times 10^{-3}$ and $P_{des}(D) = 1.73 \times 10^{-3}$ respectively. This enhancement of reactivity appears to be even more evident considering that the desorption probabilities in the sudden-transition DIET scenario as calculated here (sections 3.2, 4.3) are *per excitation event* and therefore an upper limit, whereas for the fs laser the finite excitation probability is explicitly accounted for.

There is little variation in the calculated isotope effect, which changes from 9.8 at the lowest ω to 7.6 at the region of the respective ω_r, and then increases again

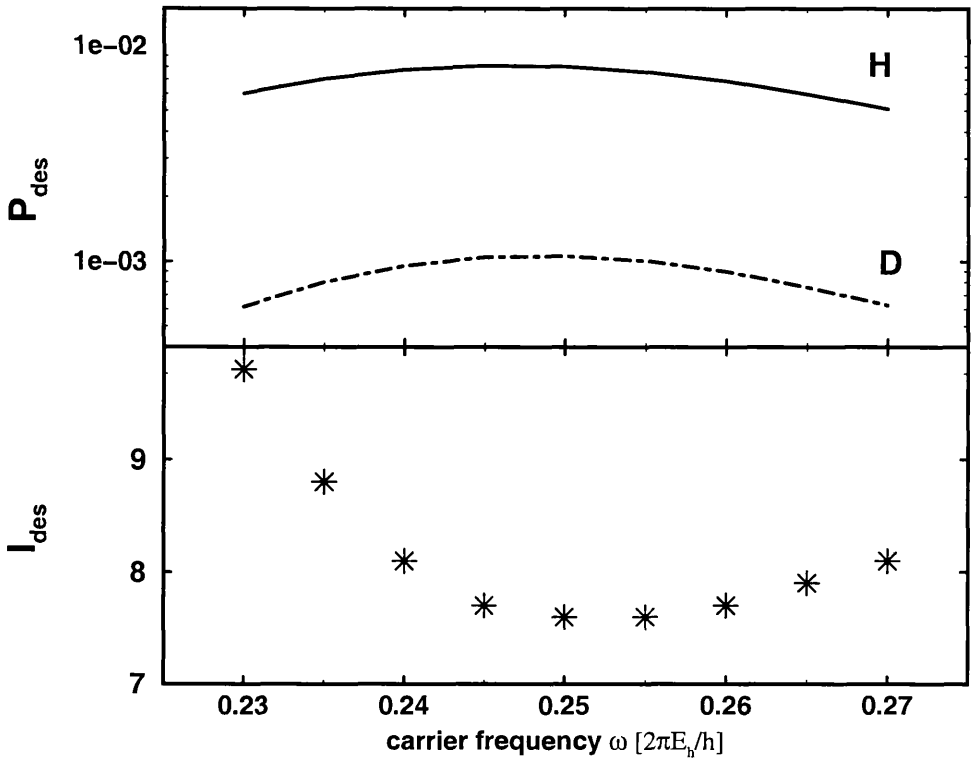

Figure 4.4: *Photo-induced desorption of H/D from Si(100)-(2x1). Shown is the desorption probability P_{des} of H (solid line) and D (dot-dashed line) as a function of the laser carrier frequency ω (semilogarithmic scale, upper panel) and the corresponding isotope ratio I_{des} (stars, lower panel). The desorption probability reaches a maximum for both H and D for $\omega = 0.245 - 0.255 E_h/\hbar$, while I_{des} is minimal for this region.*

(up to 8.1) for higher carrier frequencies, corresponding to lower desorption yields.

For the further calculations the "optimal" $\omega = 0.245\, E_h/\hbar$ for hydrogen was used.

4.4.2 Variation of the field amplitude E_0

In a next step, the field amplitude E_0 of the simple Gaussian pulse is varied, which means, under the Condon approximation, that effectively $A_0 = -\mu_{eg} E_0$ is varied. Calculations for $A_0 = 0.0097$, 0.0145, 0.0193, 0.0217 and 0.0324 E_h were carried out;

all other parameters are kept fixed:

- $\hbar\omega = 0.245\ E_h$
- $\sigma = 400\,\hbar/E_h$
- $t_0 = 1500\ \hbar/E_h$

As shown in the upper panel of Fig.4.5, the desorption probability P_{des} for both isotopes H and D increases almost linearly with the square of the laser coupling amplitude A_0 and hence quasi-linearly with the laser intensity and laser fluence, indicating a "DIET-like" scaling (see section 1.2). The lower panel of Fig.4.5 shows the corresponding isotope ratio I_{des}. Again, a higher isotope effect is found for lower yields and vice versa.

However, simply increasing the laser intensity to obtain higher photodesorption yields is not practical. The intensity of a laser beam with amplitude $A_0 = 0.0193\ E_h$ for example is $\approx 1.3 \times 10^{13}$ W/cm^2 (assuming a transition dipole moment $\mu_{eg}(Z) = 1\,ea_0 = 8.4784 \times 10^{-30}$ C m), while for the highest applied $A_0 = 0.0324\ E_h$ it is $\approx 3.7{\times}10^{13}$ W/cm^2. Whilst it is technically feasible to reach such high intensities (up to 10^{18} W/cm^2) experimentally, side-processes like thermal heating and ionisation are very likely to take place [118], which are not considered in the theoretical modelling here.

For the further calculation $A_0 = 0.0193\,E_h$ has been used, if not stated otherwise. Using this coupling amplitude, one obtains $P_{des}(H) = 0.01443$ and $P_{des}(D) = 2.129 \times 10^{-3}$. This is an increase in the desorption probability of hydrogen relative to the DIET (ns laser) case by a factor of about 8. For deuterium, this factor is even larger, namely ≈ 12 – again without taking the finite excitation probability into account. The isotope effect with this choice of A_0 is still pronounced and ≈ 7.

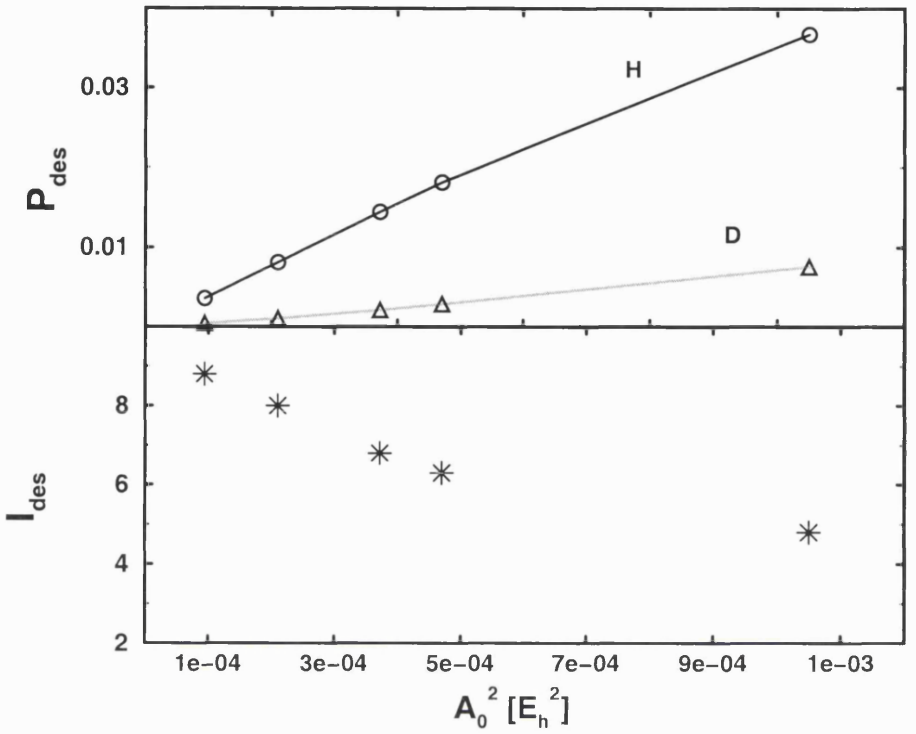

Figure 4.5: *The influence of the field coupling amplitude in photo-induced desorption of H/D from Si(100)-(2x1). In the upper panel, the desorption probabilities of H (circles, dark line) and D (triangles, grey line) are shown as a function of the square of the laser coupling amplitude* $A_0 = -\mu_{eg}E_0$. *In the lower panel the corresponding isotope ratios* I_{des} *are given. Their decrease with rising amplitude reflects the increase of the desorption probabilities of both H and D with increasing* A_0^2.

4.4.3 Variation of the laser pulse width σ

With the optimal carrier frequency for hydrogen desorption, $\omega = 0.245\,E_h/\hbar$, obtained by the variation of ω, the influence of the pulse width parameter σ was examined. The Gaussian peak time parameter t_0, i.e. the time for which the pulse becomes maximal, was chosen such that for a given σ the field is practically zero at $t = 0$ (e.g., $\mu_{eg}E(0) \approx 10^{-8}E_h$). All laser parameters investigated are given in Table 4.1 together with the resulting laser fluence $\mathcal{F}$.

Shown in Fig.4.6 are the desorption probabilities of hydrogen and deuterium

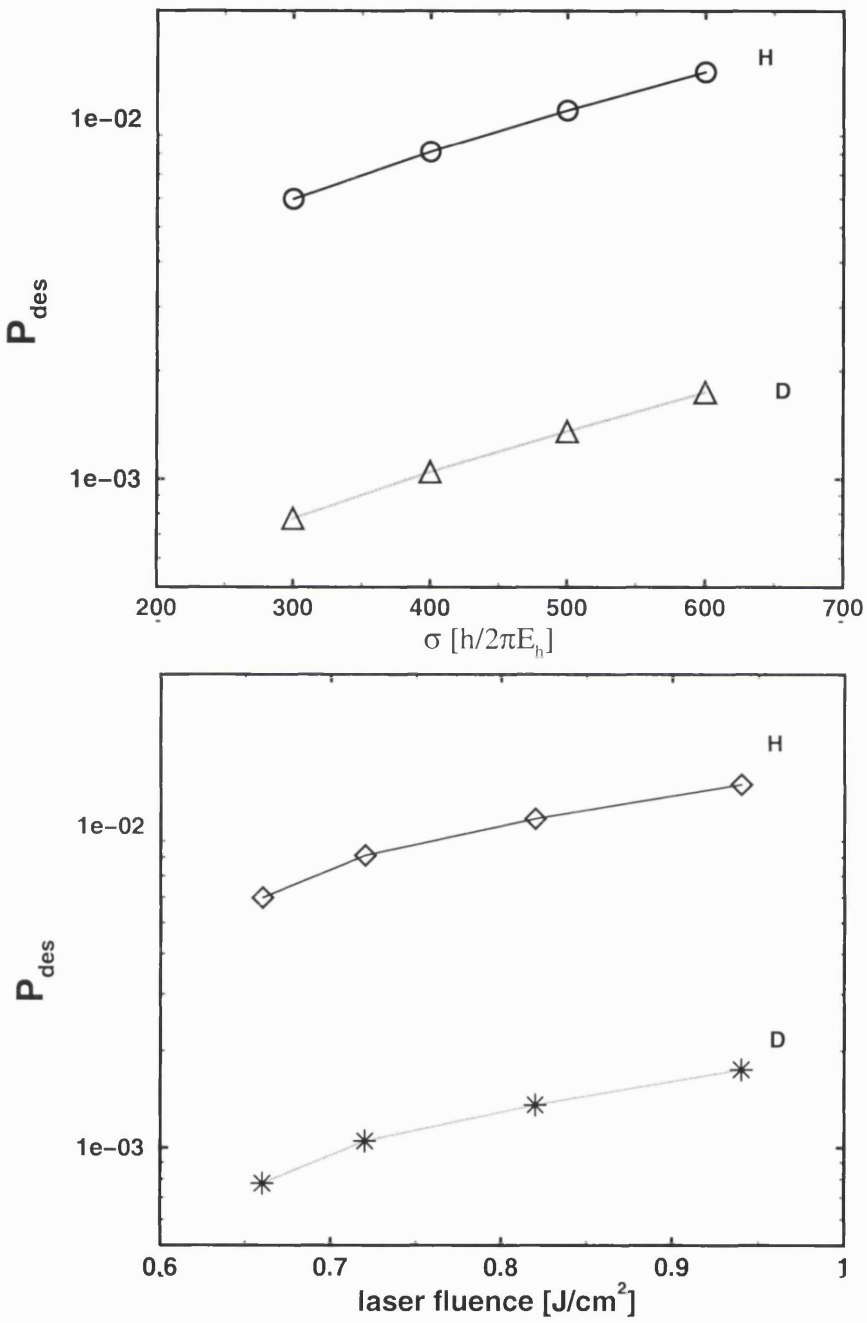

Figure 4.6: *Probabilities (semilogarithmic scale) of photo-induced desorption of hydrogen (circles, resp. diamonds) and deuterium (triangles, resp. stars) from Si(100)-(2x1) as a function of the pulse width parameter σ (upper panel) and of the laser fluence $\mathcal{F}$ (lower panel).*

$\sigma[\hbar/E_h]$	$t_0[\hbar/E_h]$	$A_0[E_h]$	$\omega[E_h/\hbar]$	$\mathcal{F}$ [J/cm^2]
300	**1500**	0.0193	0.245	0.66
400	**1500**	0.0193	0.245	0.72
500	**1600**	0.0193	0.245	0.82
600	**1800**	0.0193	0.245	0.94

Table 4.1: *Photo-induced desorption of H/D from Si(100)-(2x1). Gaussian laser pulse parameters and the resulting laser fluence $\mathcal{F}$ for the study of the influence of the width parameter σ (and the corresponding peak time t_0) on the desorption yield.*

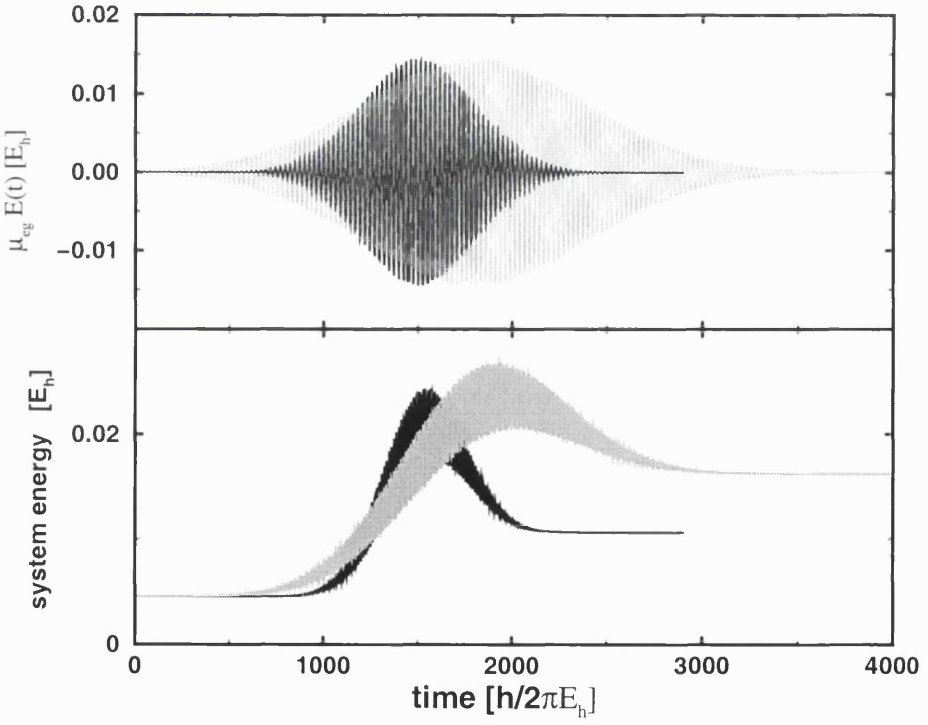

Figure 4.7: *Photo-induced desorption of H from Si(100)-(2x1) with Gaussian fs laser pulses. In the upper panel, the pulses for a width $\sigma = 300\,\hbar/E_h$ (black) and $\sigma = 600\,\hbar/E_h$ (grey) are given. In the lower panel the corresponding time evolution of the total system energy for the hydrogen desorption is shown. With the broader pulse, the system can gain more energy and so has a higher desorption probability.*

from Si(100) obtained with the laser parameters in Table 4.1 as a function of the laser width parameter σ itself and as a function of the resulting laser fluence $\mathcal{F}$. The desorption probability of H increases from $\approx 6.0 \times 10^{-3}$ for the smallest σ to $\approx 1.3 \times 10^{-2}$ for the broadest Gaussian pulse, while $P_{des}(D)$ increases from $\approx 7.7 \times 10^{-4}$ to $\approx 1.7 \times 10^{-3}$.

A broader pulse implies a larger area $\int E_o^2 s^2(t) dt$ and thus a higher laser fluence, as shown in the lower panel of Fig.4.6 and, for hydrogen, in Fig.4.7. With the broader pulse the system can gain more total energy, thus resulting in a higher desorption probability.This holds for both isotopes H and D likewise, so that the isotope ratio I_{des} stays unchanged for all different σ at $I_{des} \approx 8$.

However, as with the field amplitude, simply increasing the pulse width to enforce higher desorption rates is not realistic. The pulse energy density will increase likewise and thus lead to unwanted side-reactions like thermal heating, ionisation or even a melting of the surface . Hence, the same $\sigma = 400\,\hbar/E_h$ as in the previous sections was used for the following calculations.

4.4.4 Laser pulses with a plateau region

In accordance with the results obtained for broader Gaussian pulse it is expected that pulses with a plateau region ($t_{pla} > 0$ in Eq.(4.6)) will lead to higher desorption probabilities for both isotopes, because connected to the width of the plateau region is a higher pulse energy density.

Whilst the time t_{pla} for the plateau duration was varied between 1000 $\hbar/E_h$ and 6000 $\hbar/E_h$, the other pulse parameters were kept fixed:

- $\hbar\omega = 0.245\ E_h$
- $\sigma = 400\,\hbar/E_h$
- $A_0 = 0.0193\,E_h$
- $t_0 = 1500\ \hbar/E_h$.

The significant increase of the desorption probability P_{des} with the width of the plateau is shown in the upper panel of Fig.4.8; the numerical values are given in Table 4.2.

$t_{pla}[\hbar/E_h]$	$P_{des}(H)$	$P_{des}(D)$
0	0.0144	2.13×10^{-3}
1000	0.0443	0.0077
2000	0.0853	0.0176
3000	0.1319	0.0325
4000	0.1827	0.0520
5000	0.2350	0.0754
6000	0.2870	0.1019

Table 4.2: *Influence of the plateau time t_{pla} on the photo-desorption yield of H and D from Si(100)-(2x1).*

Without a plateau region, the corresponding simple Gaussian pulse gives $P_{des}(H) = 0.0144$ and $P_{des}(D) = 2.13 \times 10^{-3}$. With a plateau region, however, the desorption probabilities increase by a factor of 3-4 for the smallest plateau width already, while with $t_{pla} = 6000\,\hbar/E_h$ 20 times the yield for H and 48 times the yield for D is obtained, proportional to the yield produced by the corresponding simple Gaussian pulse. Comparing the desorption probability obtained with this plateau laser to the DIET case, it is found that that P_{des} of H is about 155 times as large for the fs laser than for the ns laser, while for deuterium the desorption probability is 590 times as large. With the higher yields, again the isotope effect in the desorption decreases from ≈ 6 for $t_{pla} = 1000\,\hbar/E_h$ to $I_{des} \approx 3$ for $t_{pla} = 6000\,\hbar/E_h$, demonstrating again that also the isotope ratios can be influenced by using fs rather than ns lasers.

In Fig.4.9, the situation for $t_{pla} = 4000\,\hbar/E_h$ is shown in more detail. From Fig.4.9(c), which shows the population of the excited state N_e both for H (black) and D (grey) as a function of time, it can be seen that the cw-like plateau pulse

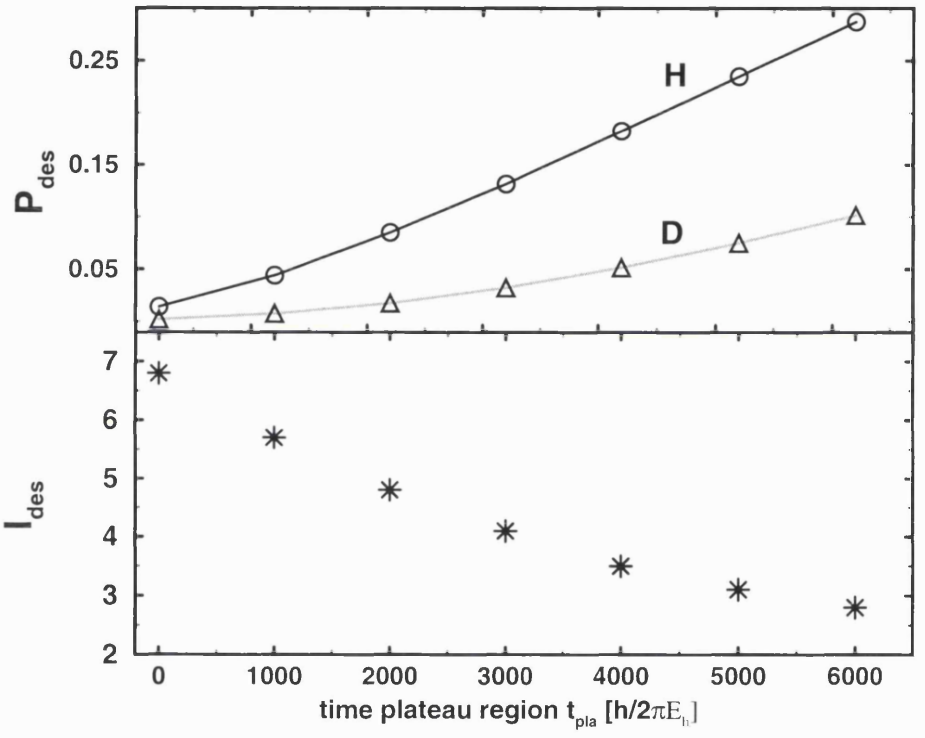

Figure 4.8: *Photo-induced desorption of H/D from Si(100)-(2x1) with "plateau pulses". Shown in the upper panel are the desorption probabilities for H (circles, black line) and D (triangles, grey line) as a function of the plateau time t_{pla}. In the lower panel, the corresponding isotope effects are given.*

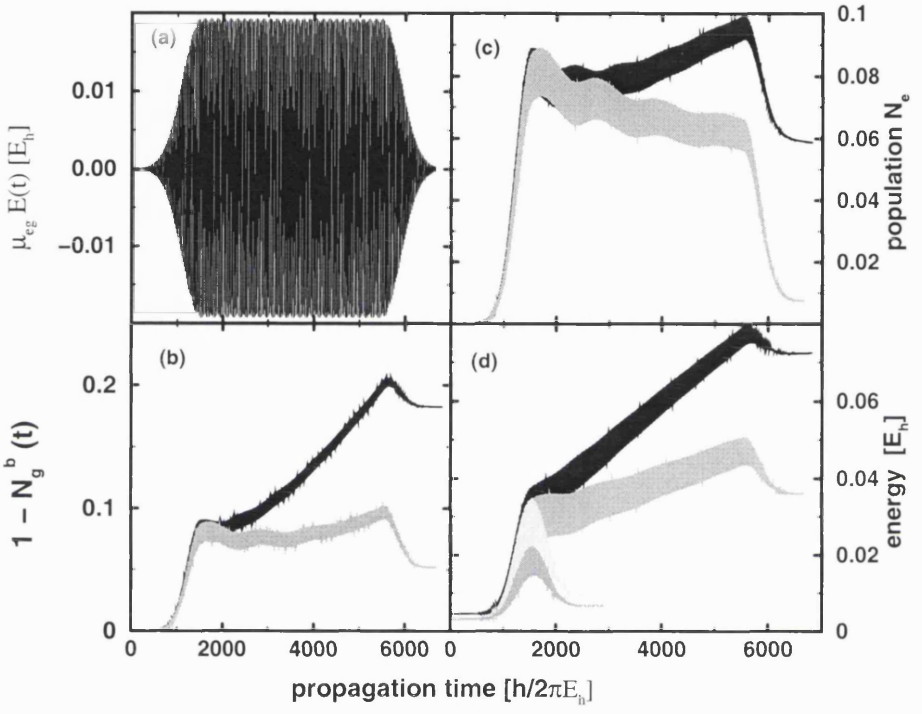

Figure 4.9: *Photo-induced desorption of H/D from Si(100)-(2x1) with a "plateau pulse". Shown is (a) the pulse with parameters* $A_0 = 0.0193\,E_h$, $\sigma = 400\,\hbar/E_h$, $\hbar\omega = 0.245\ E_h$, $t_0 = 1500\ \hbar/E_h$ *and* $t_{pla} = 4000\,\hbar/E_h$. *In (b), the resulting function* $[1 - N_g^b(t)]$ *for H (black) and D (grey) are given. (c) and (d) show the population on the excited state* $N_e(t)$ *and the total system energy, respectively for H (black) and D (grey). In (d), the system energy for an ordinary Gaussian pulse with the same parameters (but* $t_{pla} = 0\,\hbar/E_h$*) is shown for comparison (H: light grey; D: dark grey).*

shown in Fig.4.9(a) enforces damped Rabi oscillations, as it is typical for a cw laser field driven 2-level system. However, whilst for deuterium the dissipation always outweighs the energy gain through the laser field, the time evolution of $N_e(H)$ shows that for times $\geq 3000\,\hbar/E_h$, the energy gain "beats" the dissipation. The reason is that after $\approx 3000\,\hbar/E_h$ parts of the hydrogen wave packet are indeed so far away from the surface (larger Z), that the coordinate-dependent quenching rate becomes smaller than the excitation rate. Over the same time period, the slower deuterium has not come so far yet and so dissipation still dominates.

In Fig.4.9(d) the system energy curves are shown for the plateau pulse and the corresponding simple Gaussian pulse (H: light grey; D: dark grey) as a function of time. The energy increase for the isotopes is 15-20 times as high relative to the simple pulse without plateau region, leading to a strongly enhanced desorption probability P_{des}, as demonstrated in Fig.4.9(b).

4.4.5 Linearly chirped laser pulses

Along with the production of intense short laser pulses, various techniques have been developed in recent years to modulate and "shape" laser pulses. The most commonly exploited feature of modulated pulses is the *chirp*, which describes the temporal variation of the carrier frequency [119, 120, 121, 122, 123, 124]. A laser pulse is generally called *positively chirped* if the frequency increases and *negatively chirped* if it decreases with time.

The application of chirped pulses to shape nuclear wave packets and enhance vibrational coherence was first suggested by Ruhman and Kosloff [119]. They showed that negatively chirped pulses are more efficient than their unchirped counterparts for generating large-amplitude vibrational motion on the electronic ground state surface of CsI. Following this numerical study, Cerullo et al. [120] observed strong chirp dependence for high-power pulse excitation of dye molecules in solution. These authors found that the excitation process is enhanced by negatively chirped pulses

and suppressed by positively chirped ones. Negatively chirped laser pulses are also used in surface photochemistry. As argued by Yamashita et al., chirped pulses may greatly enhance the photodesorption desorption probability of NH_3/ND_3 from Cu(111) [123]. Positively chirped pulses whereas can promote reactions in the gas phase, as it was shown experimentally by Pastirk and co-workers [122]. By using positively chirped fs laser pulses they obtained an order of magnitude enhancement in the concerted elimination pathway leading to I_2 product formation in the photodissociation reaction of CH_2I_2. Conversly, negatively chirped pulses minimised the yield of I_2.

To investigate whether it is feasible to control the photodesorption of H/D from Si(100), and in particular to achieve $I_{des} < 1$, i.e., favour the desorption of deuterium to the one of hydrogen, the implications of linearly chirped fs laser pulses on the desorption yield of H and D were tested. In this case, the laser carrier frequency ω is a function of time:

$$\omega(t) = \omega_0 + \frac{\kappa}{2} t \quad . \tag{4.11}$$

Negative chirps with $\kappa < 0$ are expected to be useful here, since in this case the laser frequency ω decreases with time and hence should adapt optimally to the reduced resonance frequency of a wave packet moving away from the surface where the energy difference $V_e(Z) - V_g(Z)$ comes progressively smaller (see Fig.4.3). The optimal chirp is expected to be different for H and D, because the latter moves more slowly.

While experimenting with different chirp parameters κ, the other laser parameters were kept fixed (if not stated otherwise):

- $\hbar\omega = 0.245\, E_h$
- $\sigma = 400\, \hbar/E_h$
- $A_0 = 0.193\ E_h$
- $t_0 = 1500\ \hbar/E_h$

- $t_{pla} = 0\,\hbar/E_h$ or alternatively $t_{pla} = 2000\,\hbar/E_h$ for the chirped pulses with plateau region (see section 4.4.5.2).

4.4.5.1 Chirped Gaussian pulses

For Gaussian pulses without a plateau region different negative chirp parameters κ were tested between $-8 \times 10^{-5}\,(E_h/\hbar)^2$ and $\kappa = -1.8 \times 10^{-4}\,(E_h/\hbar)^2$ (see Table 4.3). The smaller negative κ produces an ever decreasing laser frequency ω up to the final propagation time, so the laser pulses are negatively chirped in the sense of the definition given above. The larger ones, however, produce "atypical chirps", i.e. laser pulse shapes, where the carrier frequency first decreases up to a certain time (which depends on κ), before it increases again (see Fig.4.10). In this work, those pulses will still be referred to as negatively chirped, because $\kappa < 0$. Similarly, pulses are called positively chirped if $\kappa > 0$.

Exemplary Gaussian pulses for $\kappa = -8{\times}10^{-5}\,(E_h/\hbar)^2$ and $\kappa = -1.5{\times}10^{-4}\,(E_h/\hbar)^2$ are shown in the upper part of Fig.4.10 as example. In the lower half of Fig.4.10, the corresponding functions $[1 - N_g^b(t)]$ for hydrogen are given. The shape of the $[1 - N_g^b(t)]$ curves follows closely the respective pulse shape and one can see that the pulse with $\kappa = -1.5 \times 10^{-4}\,(E_h/\hbar)^2$ (right side of the diagram) can at no time transfer as much population out of the bound electronic ground state as the pulse with the lower κ. In Table 4.3, the corresponding desorption probabilities $P_{des} = \lim_{t\to\infty}[1 - N_g^b(t)]$ are given for the pulses of Fig.4.10 as well as for the other laser pulses with negative chirp parameters κ. The desorption probabilities are 3 - 4 orders of magnitude smaller than for the corresponding unchirped fs laser pulse.

Those findings are perhaps surprising in the light of the introductory discussions, but a closer look at the desorption dynamics shows that the initial assumption that the excited wave packet moves significantly towards larger Z does not hold. The situation is shown for hydrogen in Fig.4.11 respectively, where the probability density of the wave packet in configuration space at time $t = 0$ and $t_f = 2900\,\hbar/E_h$

is given for (a) the unchirped Gaussian pulse with laser parameter $A_0 = 0.0193\,E_h$, $\sigma = 400\,\hbar/E_h$, $\hbar\omega = 0.245\ E_h$, $t_0 = 1500\ \hbar/E_h$ and (b) the same pulse, but with $\omega = \omega(t) = \omega_0 - 8.0 \times 10^{-5}\,(E_h/\hbar)^2 \cdot t$.

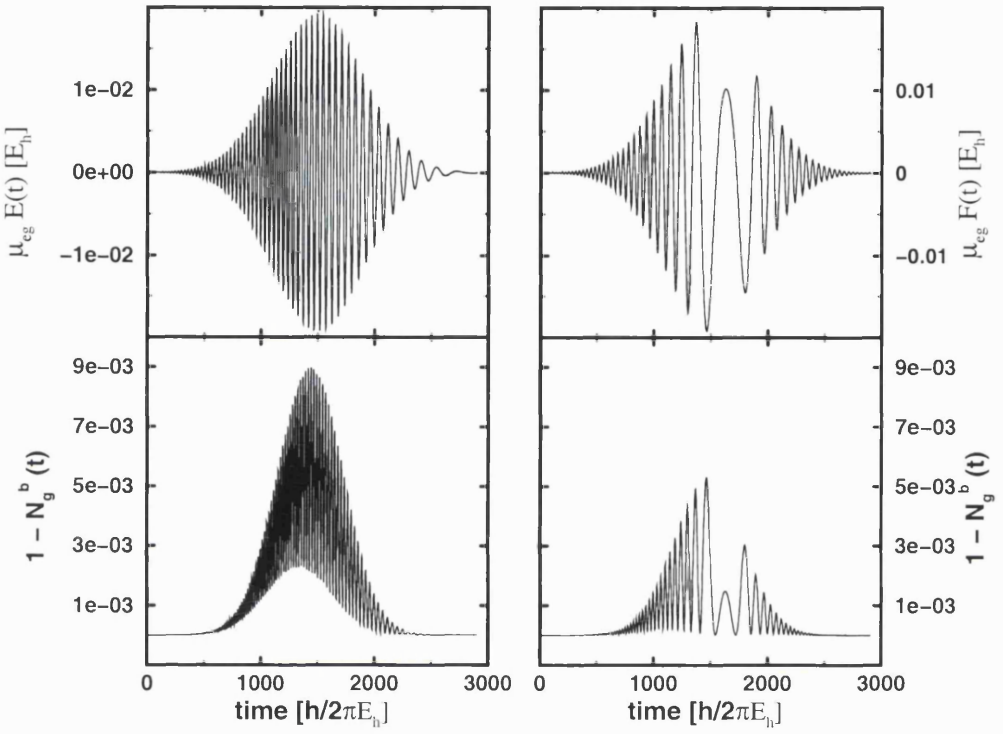

Figure 4.10: *Photo-induced desorption of H and D from Si(100)-(2x1):H/D with chirped laser pulses. On the left hand side, a pulse with* $\kappa = -8 \times 10^{-5}\,(E_h/\hbar)^2$ *(upper panel) and the corresponding function* $[1 - N_g^b(t)]$ *of hydrogen (lower panel) is shown. On the right hand side the same for a Gaussian pulse with* $\kappa = -1.5 \times 10^{-4}\,(E_h/\hbar)^2$ *is given.*

Because of the ultrafast excitation quenching (excited state lifetime $\tau = 0.4$ fs), with both the chirped and the unchirped laser pulse, the wave packet remains mainly localized around Z_0, conversely for the chirped pulse, hardly any difference is noticeable between the wave packet at time $t = 0$ and $t_f = 2900\,\hbar/E_h$. Because the excitation rate is so poor, hardly any population has the chance to reach larger distances Z where the resonance frequency ω_r becomes significantly smaller. Thus,

$\kappa[(E_h/\hbar)^2]$	P_{des}	I_{des}
0	H: 1.44 $\times 10^{-2}$	6.8
	D: 2.13 $\times 10^{-3}$	
- 8.0$\times 10^{-5}$	H: 8.48 $\times 10^{-6}$	3.1
	D: 2.74 $\times 10^{-6}$	
- 1.0$\times 10^{-4}$	H: 2.63 $\times 10^{-6}$	1.2
	D: 2.18 $\times 10^{-6}$	
- 1.2$\times 10^{-4}$	H: 9.81 $\times 10^{-7}$	**0.48**
	D: 2.04 $\times 10^{-6}$	
- 1.5$\times 10^{-4}$	H: 5.38 $\times 10^{-7}$	**0.26**
	D: 2.09 $\times 10^{-6}$	

Table 4.3: *Photo-induced desorption of H and D from Si(100)-(2x1):H/D with linearly chirped pulses. Influence of negative chirp parameters κ on the desorption yield and the isotope ratio I_{des}.*

when the pulse frequency $\omega(t)$ decreases with time, the discrepancy between $\omega(t)$ and the required ω_r increases and the excitation process becomes more and more inefficient, thus resulting in very small desorption probabilities.

However, also an increase of the pulse frequency $\omega(t)$ with time does not lead to significantly higher desorption probabilities (see Table 4.4). Compared to the corresponding unchirped laser pulses, the desorption probabilities obtained with positively chirped laser pulses are still 2 - 3 orders of magnitude lower. The reason here is that the pulse frequency $\omega(t)$ very quickly becomes much larger than the optimal resonance frequency ω_r. Thus the excitation of the adsorbate becomes more and more inefficient with time as well, producing just small desorption probabilities.

An interesting point is the influence of the chirped pulses on the isotope ratio I_{des}. As listed in Table 4.3, even $I_{des} < 1$ can be achieved for the "atypical"

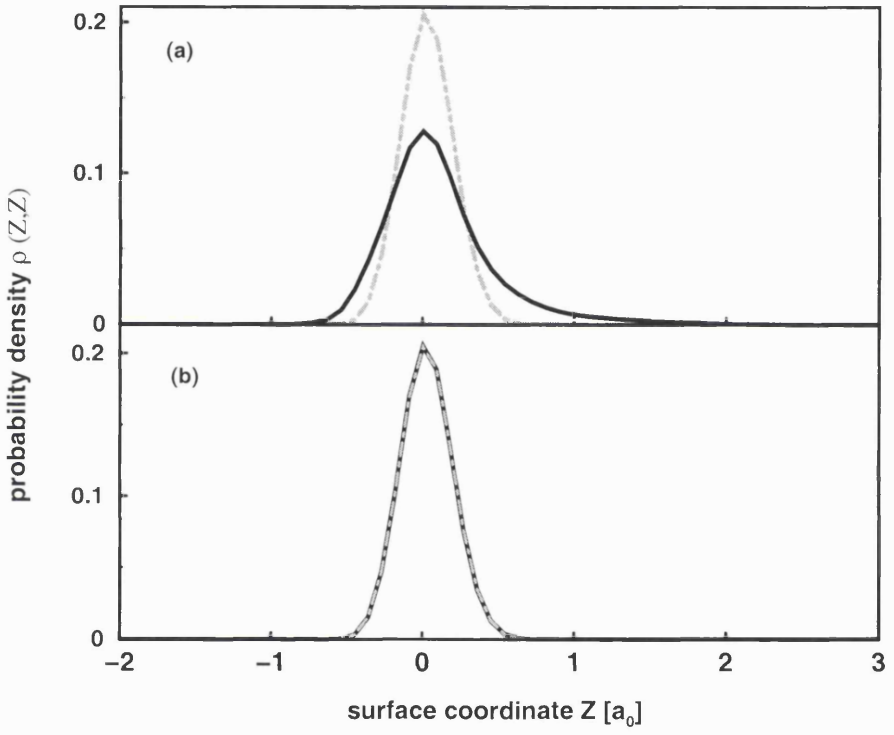

Figure 4.11: *Probability density of the hydrogen wave packet in configuration space at time* $t = 0$ *(dot-dashed grey line) and* $t_f = 2900\,\hbar/E_h$ *(solid black line) for (a) the unchirped Gaussian pulse with laser parameter* $A_0 = 0.0193\,E_h$, $\sigma = 400\,\hbar/E_h$, $\hbar\omega = 0.245\ E_h$, $t_0 = 1500\ \hbar/E_h$ *and (b) the same pulse, but with* $\omega = \omega(t) = \omega_0 - 8.0 \times 10^{-5}\,(E_h/\hbar)^2 \cdot t$.

$\kappa[(E_h/\hbar)^2]$	P_{des}	I_{des}
0	H: 1.44 $\times 10^{-2}$	6.8
	D: 2.13 $\times 10^{-3}$	
+ 8.0$\times 10^{-5}$	H: 7.60 $\times 10^{-5}$	6.2
	D: 1.23 $\times 10^{-5}$	
+ 1.0$\times 10^{-4}$	H: 3.74 $\times 10^{-5}$	3.9
	D: 9.60 $\times 10^{-6}$	
+ 1.2$\times 10^{-4}$	H: 2.24 $\times 10^{-5}$	3.1
	D: 7.29 $\times 10^{-6}$	

Table 4.4: *Photo-induced desorption of H and D from Si(100)-(2x1):H/D with linearly chirped pulses. Influence of positive chirp parameters κ on the desorption yield and the isotope ratio I_{des}.*

negative chirps. Further tests with other Gaussian pulses show that for example with $A_0 = 0.0145\,E_h$, $\sigma = 400\,\hbar/E_h$, $\hbar\omega = 0.268\ E_h$, $t_0 = 1500\ \hbar/E_h$ and $\kappa = -1.5 \times 10^{-4}\,(E_h/\hbar)^2$, ratios I_{des} as small as 0.1 can be obtained (in this case $P_{des}(H) = 2.107 \times 10^{-7}$ and $P_{des}(D) = 1.975 \times 10^{-6}$). Albeit the definite origin of these isotope ratios is not yet fully understood, it seems possible to significantly influence the isotope ratio of the photodesorption process. However, further examinations are clearly necessary.

4.4.5.2 Chirped pulses with a plateau region

Tests were also performed for chirped pulses with a plateau region. Here, the desorption probabilities are 1-2 orders of magnitudes higher than for the chirped pulses without a plateau region, but still very small compared to the corresponding unchirped ones (see section 4.4.4) for the reasons discussed above.

In Fig.4.12, two pulses with parameters $A_0 = 0.0193\,E_h$, $\sigma = 400\,\hbar/E_h$, $\hbar\omega = 0.245\ E_h$, $t_0 = 1500\ \hbar/E_h$ and $t_{pla} = 2000\ \hbar/E_h$ are shown, while in (a) $\kappa =$

$-5.0 \times 10^{-5}\,(E_h/\hbar)^2$ and in (b) $\kappa = -6.2 \times 10^{-5}\,(E_h/\hbar)^2$. In the lower panels of (a) and (b) the computed function $[1 - N_g^b(t)]$ for H (black) and D (grey) are given. While for the unchirped plateau pulses $[1 - N_g^b(t)]$ increases for the whole time the

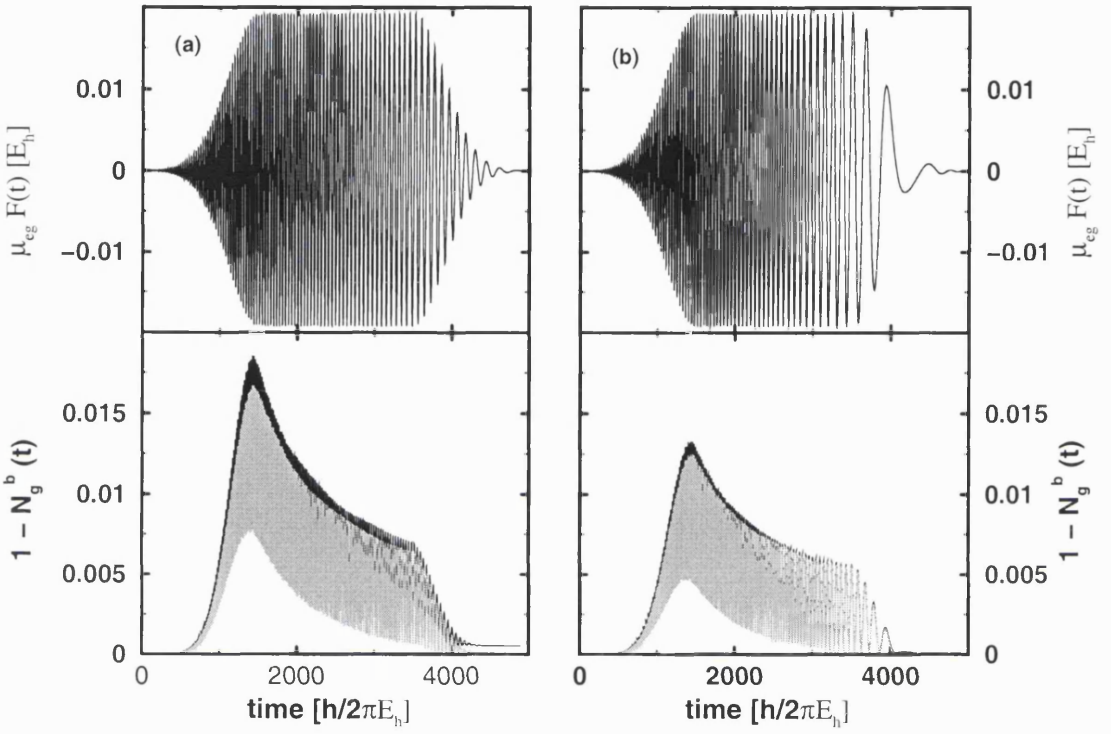

Figure 4.12: *Photo-induced desorption of H/D from Si(100)-(2x1) with chirped "plateau pulses". In the upper panel of (a), the laser pulse with parameters* $A_0 = 0.0193\,E_h$, $\sigma = 400\,\hbar/E_h$, $\hbar\omega = 0.245\ E_h$, $t_0 = 1500\ \hbar/E_h$, $t_{pla} = 2000\ \hbar/E_h$ *and* $\kappa = -5.0 \times 10^{-5}\,(E_h/\hbar)^2$ *is shown with the resulting function* $[1 - N_g^b(t)]$ *for each H (black) and D (grey). In (b) the same is given for an similar pulse, but* $\kappa = -6.2 \times 10^{-5}\,(E_h/\hbar)^2$.

pulse is switched on (see for example Fig.4.9), here it decreases with decreasing laser frequency $\omega(t)$, thus producing lower desorption probabilities compared to the unchirped case (see Table 4.5). The reason is again that no parts of the wave packet can reach larger Z in time to adapt to the decreasing laser frequency $\omega(t)$ and be efficiently excited. However, because of the higher pulse energy density a higher

desorption rate can be achieved than with simple chirped Gaussian pulses.

$\kappa[(E_h/\hbar)^2]$	P_{des}	I_{des}
0	H: 8.54 $\times 10^{-2}$	4.8
	D: 1.76 $\times 10^{-3}$	
-3.4$\times 10^{-5}$	H: 4.83 $\times 10^{-3}$	16
	D: 3.11 $\times 10^{-4}$	
-5.0$\times 10^{-5}$	H: 4.01$\times 10^{-3}$	17
	D: 2.41 $\times 10^{-4}$	
-6.2$\times 10^{-5}$	H: 8.17 $\times 10^{-4}$	21
	D: 3.88 $\times 10^{-5}$	
+3.4$\times 10^{-5}$	H: 3.98 $\times 10^{-3}$	10
	D: 3.88 $\times 10^{-4}$	
+5.0$\times 10^{-5}$	H: 2.22 $\times 10^{-4}$	6
	D: 3.68 $\times 10^{-5}$	
+6.2$\times 10^{-5}$	H: 1.16 $\times 10^{-4}$	5
	D: 2.43 $\times 10^{-5}$	

Table 4.5: *Photo-induced desorption of H and D from Si(100)-(2x1):H/D with linearly chirped "plateau" pulses. Influence of the chirp parameter κ on the desorption yield and the isotope ratio I_{des}.*

With positively chirped plateau pulses one obtains only slightly different desorption probabilities than with negatively chirped ones. This indicates that the magnitude of the desorption rates is dominated by the overall pulse energy density rather than the chirp, i.e., the laser frequency.

Remarkably high isotope effects are found with negatively chirped pulses. For $\kappa = -3.4 \times 10^{-5}\,(E_h/\hbar)^2$, the ratio $P_{des}(H)/P_{des}(D) \approx 16$ and for $\kappa = -6.2 \times 10^{-5}\,(E_h/\hbar)^2$, I_{des} is even higher, ≈ 21. But here, as in the previous chapter, further investigations about the origin of the isotope ratios are clearly necessary.

4.5 Summary and conclusions

An open system density matrix approach was adopted for the theoretical investigation of the photo-induced desorption of hydrogen and deuterium from Si(100)-(2x1):H/D. The modelling of the desorption dynamics was done within a 1 mode - 2 state MGR type model, including a coordinate-dependent decay rate of the electronically excited state.

The use of femtosecond rather than nanosecond lasers has been suggested to directly photodesorb hydrogen and deuterium from the Si(100) surface. By shaping the ultrashort pulses, the possibility of influencing the desorption process, i.e. yields and isotope ratios, emerges. This was not obvious from the outset because the quenching of the excited state resonance proceeds within less than a fs, which is much shorter than the pulses employed.

Very substantial increases in the desorption yield compared to the ns laser induced DIET process can be accomplished by using fs Gaussian pulses with a plateau region, while variations of the isotope effects in the desorption yields between 0.1 and 21 were achieved by using linearly chirped pulses.

However, for final conclusions directly relevant for a quantitative experimental verification a more systematic investigation of the parameter space is required together with a more detailed treatment of the process, e.g. including multi-dimensionality.

Chapter 5

Photodesorption of NO from Pt(111) [62]

The photodesorption of NO from various metal, semiconductor, insulator and alloy surfaces is a "prototypical" case for laser-induced photochemistry at surfaces, extensively studied both experimentally and theoretically [11]. With low-intensity ns-lasers, DIET experiments have been carried out, for example, for NO/Pt(111) [48, 49], NO/Pt(100) [125], NO/Ni(100)-O [126], NO/Pt(111)-Ge [127], NO/Si(111)7×7 [128], NO/NiO(100) [129], NO/NiO(111) [130]. Similarly, with high-intensity laser-pulses in the (sub-) ps range, DIMET for NO/Pd(111) [131], NO/Pt(111) [28] and NO/NiO(100) [132] has been observed. In most of these experiments, not only were the integral desorption cross sections and product translational energies measured, but also state-resolved quantities, e.g., the population of vibrational, rotational, or spin–orbit coupled states.

In contrast to the laser-induced desorption of H from Si(100) (see previous section) an *indirect* mechanism is assumed for the excitation process in the NO/Pt(111) system. An initial creation of "hot electrons" in the metal substrate is assumed, which then transfer energy to the adsorbate and eventually lead to the forming of a *"negative ion resonance"*. Subsequent evolution of the non-stationary excited ad-

sorbate and simultaneous electronic relaxation can lead to the desorption of neutral molecules in their electronic ground state.

5.1 Review of experimental results and previous theoretical treatment

For the DIET of NO from Pt(111), Buntin et al. [48, 49] found that the desorption probability is typically low: When 355 nm laser pulses with a FWHM of 9 ns were used, $\approx 5 \times 10^{-8}$ NO molecules desorbed per absorbed photon, corresponding to a total cross section of 2.5×10^{-22} cm^{-2}. The desorbates are both translationally and vibrationally hot. The average kinetic energy is $\langle E_{kin} \rangle \approx 0.2$ eV, giving a flux-weighted "translational temperature" of $T_{kin} = \langle E_{trans} \rangle / 2k_B \approx 1200$ K. Only $v = 0$ and $v = 1$ vibrational states of free nitric oxide are significantly populated, with a ratio of $P_1/P_0 \approx 0.04$. This corresponds to a "vibrational temperature" of the desorbates of $T_{vib} = 850$ K, which is in fact "hot" as compared to the surface temperature of $T_s = 200$ K. These results depend somewhat on the ns laser pulse parameters. For instance, for pulses of 5 ns FWHM (at a wavelength of 355 nm), a cross section of $4 \cdot 10^{-21}$ cm^{-2} and a translational temperature of about $T_{trans} \approx 670$ K was reported [28].

When ultrashort (sub-ps), high-intensity lasers are used for excitation, an adsorbate can undergo multiple transitions between ground and excited state(s). This DIMET case can be distinguished from DIET by the so-called "DIMET hallmarks" (see section 1.2). Experiments for NO/Pt(111) in the multiple excitation limit have bee carried out by Ho and co-workers [28]. Using lasers with FWHM below 200 fs, it was observed that the desorption yield can increase by orders of magnitude, and that it scales superlinearly (according to $\mathcal{F}^{6\pm1}$) with laser fluence $\mathcal{F}$. In contrast, the DIET yields typically increase linearly with $\mathcal{F}$. Further, the translational energy $\langle E_{kin} \rangle$ was found to increase for fluences larger than 2 mJ/cm^2 near–linearly with

$\mathcal{F}$, while under DIET conditions $\langle E_{kin} \rangle$ is independent on the laser fluence. Usually, DIMET conditions lead to enhanced vibrational excitation [131, 132].

Quantum theoretical simulations on the photodesorption in NO/metal and NO/oxide systems have been carried out by various groups [31, 32, 35, 36, 42, 47, 60, 61, 133, 134, 135]. Most of these theoretical treatments made use of an one-dimensional (1D) Antoniewicz-type (see section 1.4) two-state *negative ion resonance* model [42]. The 1D model is attractive computationally and the relative success of 1D models for NO/Pt relies on the fact that excitation of an internal adsorbate mode (the NO stretch) is not as important as for other systems, such as ammonia desorbing from various substrates [111, 110] . However, for a more complete and quantitative description of the NO desorption process, the inclusion of the NO vibration is mandatory. So far, for this purpose mostly simplified semiclassical [42, 136] or single–quantum trajectory wave packet treatments [47] of two-dimensional (2D) models (including Z, the molecule-surface distance and r, the NO stretch) have been considered. In the latter, a single residence time τ_R for the wave packet in the excited state is assumed, rather than a distribution of residence times.

5.2 Potential energy surfaces

In this work, DIET and DIMET of NO from Pt(111) have been described by a two-state Antoniewicz-type model, considering two degrees of freedom, namely the molecule-surface distance Z and the NO stretch r. The nuclear system Hamiltonian is again assumed to be uncoupled:

$$\hat{H}_s = \hat{H}_g |g\rangle\langle g| + \hat{H}_e |e\rangle\langle e| \quad , \tag{5.1}$$

where $|g\rangle$ is a stable ground state and $|e\rangle$ a short-lived excited intermediate state. The Hamiltonian is taken to be of the form

$$\hat{H}_l = -\frac{\hbar^2}{2}\left(\frac{1}{m_r}\frac{\partial^2}{\partial r^2} + \frac{1}{m_Z}\frac{\partial^2}{\partial Z^2}\right) + V_l(r, Z) \quad ; l = g, e \quad , \tag{5.2}$$

with r and Z being the vibrational and the centre-of-mass motion of NO, respectively. $m_r = m_N m_O/(m_N + m_O)$ is the reduced mass of NO and $m_Z = m_O + m_N$ the total molecular mass.

For the electronic ground state, corresponding to a neutral ground state NO molecule adsorbing on top of a Pt(111) substrate with its molecular axis perpendicular to the surface, a model potential as suggested by Chakrabarti et al. [47] was used. The potentials are given in terms of the shortest distance from the metal surface to N and O, x_{PtN} and x_{PtO}, respectively. The coordinates transform as follows:

$$x_{\mathrm{PtN}} = Z - r\,\frac{m_O}{m_O + m_N} \tag{5.3}$$

and

$$x_{\mathrm{PtO}} = Z + r\,(1 - \frac{m_O}{m_O + m_N}) \tag{5.4}$$

with m_O and m_N being the mass of oxygen and nitrogen, respectively, and

$$r = x_{\mathrm{PtO}} - x_{\mathrm{PtN}} \quad . \tag{5.5}$$

Thus, the electronic ground state potential is given by

$$V_g = V_{\mathrm{PtN}} + V_{\mathrm{PtO}} + V_{\mathrm{NO}} \quad , \tag{5.6}$$

where the V_i are Morse potentials for i =PtN and i =NO,

$$V_i(y) = D_i[1 - e^{-\beta_i(y - y_{g0})}]^2 \tag{5.7}$$

($y = x_{\mathrm{PtN}}$ or $y = r$), while for the PtO interaction an exponential repulsion is assumed:

$$V_{\mathrm{PtO}}(x_{\mathrm{PtO}}) = Ae^{-\alpha x_{\mathrm{PtO}}} \quad . \tag{5.8}$$

This potential predicts a binding energy $\approx$ 1.1 eV and vibrational frequencies consistent with experiment [47].

Unfortunately, the excited state surface is poorly characterised. Chakrabarti and co-workers assumed that it is of the negative ion resonance or metal-to-ligand

charge transfer type [47], describing the interaction of an NO^- molecule with the Pt substrate with one electron removed. The suggested potential is [47]

$$V_e = V_{\mathrm{PtN}} + V_{\mathrm{PtO}} + V_{\mathrm{NO^-}} + \Phi_{\mathrm{Pt}} + V_{\mathrm{im}} \quad , \tag{5.9}$$

where Φ_{Pt} is the work function of Pt and V_{im} is an image-charge attraction term accounting for the attraction of NO^- by a positive image charge in the metal surface:

$$V_{\mathrm{im}} = -\frac{1}{4(Z - Z_{\mathrm{im}})} \quad . \tag{5.10}$$

In deviation from Ref.[47], Finger and Saalfrank introduced a shift parameter Δ, which produces an energy difference $V_e - V_g$ of 1.5 eV at the Franck-Condon point, consistent with inverse photoemission data [137]. Finally, $V_{\mathrm{NO^-}}$ in Eq.(5.9) is a Morse potential for NO^-:

$$V_{\mathrm{NO^-}}(r) = D_{\mathrm{NO^-}} \left[1 - e^{-\beta_{\mathrm{NO^-}}(r - r_{0,\mathrm{NO^-}})}\right]^2 \quad . \tag{5.11}$$

Both the ground and excited state potentials are bound. The equilibrium geometry of the ground state is at $r_{\mathrm{min}} = 1.16$ Å and $Z_{\mathrm{min}} = 2.16$ Å with the parameters given in Table 5.1.

For the NO^- resonance state, Chakrabarti et al. assumed a gas phase bond length difference between NO and NO^- of $\Delta r \approx 0.1$ Å remains the same also in the adsorbed state [47]. By simply using the parameters of a free gas-phase NO^-, the equilibrium geometry is $r = 1.24$ Å, $Z = 1.93$ Å (this surface model will be called henceforth "model A"). This implies that upon excitation the wave packet will initially move inward (towards lower Z) and at the same time towards increasing NO bond length r [47, 135, 60], leading eventually to vibrationally excited products.

Guo found [135] that the experimentally measured moderate vibrational excitation of the desorbing NO molecule is incompatible with the model potentials proposed in Ref.[47], as it was also found by Finger and Saalfrank [60]. As a consequence, the negative ion resonance model for the photodesorption of NO from

metal surfaces was questioned [136, 138]. The too pronounced vibrational excitation results from too large a NO bond-lengthening in the excited state after a full one-electron charge transfer into the anti-bonding $2\pi^*$ level of NO.

To obtain a better agreement between theory and experiment, in Refs.[60] and [135] the problem was "solved" by simply reducing r_{0,NO^-} in (5.9). In this work, a slightly more sophisticated ansatz is chosen in relaxing the full one-electron charge transfer assumption. It was argued on the basis of tight-binding Green's function calculations [117] that a full charge transfer should occur only asymptotically, i.e., $\delta = \delta(Z)$ and $\lim_{Z\to\infty}\delta(Z) = -1|e|$, while closer to the surface the transfer is incomplete, $|\delta(Z)| < 1$. This is because the closer the molecule is to the surface, the broader the excited state resonance becomes, eventually back-donating charge to the metal substrate. Particularly around the Franck-Condon point the excited, adsorbed NO molecule may actually be only slightly negatively charged. Accordingly, there is a smooth transition between partial and full charge transfer with increasing distance Z. Therefore, a coordinate-dependence of the NO^- Morse parameters in Eq.(5.9) is expected to be more realistic than assuming a full electron transfer irrespective of geometry.

Potential parameters: Ground state	
Morse well depth V_{NO}	$D_{NO} = 0.2433$ E$_h$ $= 6.62$ eV
Morse well depth V_{PtN}	$D_{PtN} = 0.0429$ E$_h$ $= 1.17$ eV
Morse well location V_{NO}	$r_{0,NO} = 1.151$ Å
Morse well location V_{PtN}	$x_{0,PtN} = 1.50$ Å
Morse exponent V_{NO}	$\beta_{NO} = 2.743$ Å^{-1}
Morse exponent V_{PtN}	$\beta_{PtN} = 1.682$ Å^{-1}
Exponential prefactor V_{PtO}	$A = 23.3182$ E$_h$ $= 634.51$ eV
Exponential range parameter V_{PtO}	$\beta = 3.366$ Å^{-1}
Potential parameters: Excited state(s)	
Morse well depth V_{NO^-}	$D_{NO^-} = 0.1889$ E$_h$ $= 5.14$ eV
Morse well location V_{NO^-}	$r_{0,NO^-} = 1.258$ Å
Morse exponent V_{NO^-}	$\beta_{NO^-} = 2.229$ Å^{-1}
"image plane"	$z_{im} = 0.847$ Å
Work function Pt(111)	$\Phi = 5.70$ eV
Shift parameter (model A)	$\Delta = 1.7749$ eV
Shift parameter (model B)	$\Delta = 1.5267$ eV
Range of "switch" function $\delta(Z)$ (model B)	$\zeta = 32.139$ Å^{-2}
Propagation: Grid parameters	
Grid spacings	$\Delta_Z = 0.01$ Å
	$\Delta_r = 0.024$ Å
Nb. of grid points	$N_Z = 2048$
	$N_r = 32$
Grid starts at	$Z = 1.19$ Å
	$r = 0.84$ Å
Propagation: Cutoff function $f(Z) = 1 - [1 + e^{\alpha(Z-Z_d)}]^{-1}$	
Wave packet considered desorbed for	$Z_d > 5.29$ Å
Range parameter	$\alpha = 7.559$ Å^{-1}
Propagation: Split operator propagation parameters	
Time step	$\Delta t = 0.19$ fs
Total propagation time (DIET)	$t_f = 754.7$ fs
Total propagation time (DIMET)	$t_f = 1064.7$ fs
Lifetime averaging parameters (Gadzuk)	
"Residence time grid" starts at	$\tau_{R0} = 1$ fs
"Residence time grid" spacing	$\Delta_R = 1$ fs
Number of residence times considered	$N = 80$
Electronic temperature profile parameters	
Energy difference parameter	$\Delta V = 1.50$ eV
Characteristic times	$\tau_1 = 145.2$ fs
	$\tau_2 = 96.8$ fs
	$\tau_3 = 16.94$ fs

Table 5.1: Photodesorption of NO from Pt(111): Numerical parameters for the potentials, wave packet propagation, lifetime averaging, and for the electronic temperature $T_{el}(t)$ (Eq.(5.30)).

In "surface model B" the Z-dependence of the NO^- Morse parameters is included, reflecting a continuous transition from weak charge transfer at small Z to full charge transfer at $Z \to \infty$. Specifically it is chosen

$$r_{0,\mathrm{NO}^-} \to r_{0,\mathrm{NO}^-}(Z) = \delta(Z) \cdot r_{0,\mathrm{NO}^-} + [1 - \delta(Z)] \cdot r_{0,\mathrm{NO}} \quad , \tag{5.12}$$

where the $r_{0,\mathrm{NO}}$ and r_{0,NO^-} are the equilibrium positions for the electronic ground and excited state Morse functions of NO, as given in Table 5.1. Analogous transformations are used for the Morse well depth, $D_{\mathrm{NO}^-} \to D_{\mathrm{NO}^-}(Z)$ and for the exponents, $\beta_{\mathrm{NO}^-} \to \beta_{\mathrm{NO}^-}(Z)$ [1]. $\delta(Z)$ is a "switch" function which can also be interpreted as a Z-dependent charge transfer, chosen as

$$\delta(Z) = \begin{cases} 0 & \text{, if} \quad Z \leq Z_{\mathrm{im}} \\ 1 - e^{-\zeta(Z - Z_{\mathrm{im}})^2} & \text{, if} \quad Z > Z_{\mathrm{im}} \end{cases} \tag{5.13}$$

For 2D model surface B, also the shift parameter Δ in Eq.(5.9) was adjusted to produce the correct excitation energy (see Table 5.1). Both excited state models A and B are of very similar topology. However, model surface B predicts an equilibrium geometry for the excited state of r=1.17 Å, Z=1.91 Å, i.e, the NO bond length difference Δr is now only $\Delta r \approx 0.01$ Å.

5.3 Computation of properties

Stochastic wave packet methods were used to model the photodesorption of NO from Pt(111), and for each quantum "trajectory" n the properties of interest were calculated as follows: The population of the electronic states is given by

$$N_{i,n} = \langle \Psi_{i,n}(Z, r; t) | \Psi_{i,n}(Z, r; t) \rangle_{Z,r} \quad \text{with} \quad i = e, g; \tag{5.14}$$

[1] In principle, the Z-dependence of the charge transfer should also enter the image-charge term in Eq.(5.10), for example by replacing the 1 in the denominator by $\delta(Z)^2$. Since the image charge approximation is anyway questionable for Z smaller than ≈ 2 Å, it was refrained from doing so.

where $\langle\rangle_{Z,r}$ denotes the integration over Z and r. For the analysis of the desorbed part, an asymptotic part $|\Psi_n^a(Z,r;t)\rangle$ of the nuclear wave function is computed by multiplying the ground state wave packet at time t with a smoothing cut-off function:

$$|\Psi_n^a(Z,r;t)\rangle = |\Psi_{g,n}(Z,r;t)\rangle \cdot \left(1 - 1[1 + e^{\alpha(Z-Z_d)}]^{-1}\right) \quad . \tag{5.15}$$

The cut-off function makes it possible to to perform Fourier transforms of the desorbed part without obtaining artificial oscillations in order to calculate its kinetic energy (see below).

The desorption probability for each quantum trajectory is given as

$$p_{des,n}(t) = \langle\Psi_n^a(Z,r;t)|\Psi_n^a(Z,r;t)\rangle_{Z,r} \quad . \tag{5.16}$$

The final population of the vibrational states of desorbed NO is obtained by projecting the asymptotic wave function $|\Psi_n^a(Z,r;t)\rangle$ on the asymptotic vibrational eigenstates $|v_g(r)\rangle$ of free NO and integration over Z

$$P_{des,v,n}(t) = \int |\langle v_g(r)|\Psi_n^a(Z,r;t)\rangle_r|^2 dZ \quad . \tag{5.17}$$

Summation over the eigenstates v gives then the total desorption probability $\langle P_{des}\rangle(t)$:

$$\langle P_{des,n}\rangle(t) = \sum_v P_{des,v,n}(t) \quad . \tag{5.18}$$

The state resolved translational energy in Z direction is obtained as

$$E_{kin,v,n}(t) = \langle\tilde{\Psi}_{v,n}^a(k_Z,t)|\hbar^2 k_Z^2/2m_Z|\tilde{\Psi}_{v,n}^a(k_Z,t)\rangle_{k_Z} \quad , \tag{5.19}$$

with

$$|\tilde{\Psi}_{v,n}^a(k_Z,t)\rangle = \frac{1}{\sqrt{2\pi}} \int_{-\infty}^{\infty} e^{-ik_Z Z} |\Psi_{v,n}^a(Z;t)\rangle dZ \tag{5.20}$$

being the Fourier transform of

$$|\Psi_{v,n}^a(Z;t)\rangle = \langle\phi_v(r)|\Psi_n^a(Z,r;t)\rangle_r \quad . \tag{5.21}$$

The total translational energy of the desorbed part is the sum over the eigenstates v:

$$E_{kin,n}^{tot}(t) = \sum_v E_{kin,v,n}(t). \tag{5.22}$$

For the total kinetic energy and the vibrational population distribution of the desorbed part, the averaged expectation values are obtained by dividing by the averaged desorption probability to give the values per desorbed molecule:

$$\langle E_{kin} \rangle(t) = \frac{E_{kin}^{tot}(t)}{\langle P_{des} \rangle(t)} \quad . \tag{5.23}$$

and the total vibrational energy $E_{vib}(t)$ per molecule (excluding zero-point motion) is

$$\langle E_{vib} \rangle(t) = \frac{\sum_v P_{des,v}(t) \cdot (\varepsilon_v - \varepsilon_0)}{\langle P_{des} \rangle(t)} \quad . \tag{5.24}$$

Again, a grid representation for the wave functions and the operators was chosen and the propagation was done using the FFT method and a split-operator propagator (see appendix A). All computational parameters for the propagation and the averaging procedure are given in Table 5.1; they are more strictly adopted to the problem than in Ref.[60].

5.4 DIET dynamics in the two-mode model

The DIET dynamics is treated within the (generalized) Gadzuk algorithm as outlined in sections 2.2.2.2 and 2.2.2.3. The electronic quenching of the excited state is modelled by the single Lindblad operator

$$\hat{C}_1 = \sqrt{\Gamma_{ge}} |g\rangle\langle e| \quad . \tag{5.25}$$

The decay rate Γ_{ge} in Eq.(5.25) is in general expected to be a function of the coordinates. Coordinate-dependent quenching must be assumed, because free NO^- is stable (NO has a positive electron affinity), and hence $\lim_{Z\to\infty} \Gamma_{ge}(r, Z) = 0$. $r \to \infty$ corresponds to the creation of free a O^- ion, which is also stable, and a neutral N atom on the surface. Thus, also $\lim_{r\to\infty} \Gamma_{ge}(r, Z) = 0$. To account for this, the quenching rate is taken to be

$$\Gamma_{ge}(r, Z) = \Gamma_{ge}^0 \cdot e^{-\beta_r (r - r_{\min})} \cdot e^{-\beta_Z (Z - Z_{\min})} \tag{5.26}$$

where the β_i's ($i = r, Z$) are range parameters and $r_{\min}, Z_{\min}$ are the coordinates of the electronic ground state minimum.

The simulations were performed by (i) numerically diagonalizing the electronic ground state Hamiltonian $\hat{H}_g$ to obtain the bound states $|v_g\rangle$ of the system, (ii) repeatedly propagating $|0_g\rangle$ under the influence of the excited state Hamiltonian (5.1), (iii) analyzing the part of the wave function passing a hypothetical line at Z_d which separates the reactants from the product (see above), and (iiii) averaging according to Eq.(2.38) respectively Eq.(2.44).

5.4.1 General aspects of DIET dynamics

As a first step, the DIET process was investigated for $T_s = 0$ K and a coordinate independent decay rate $\Gamma_{ge} = \Gamma_{ge}^0 = 1/\tau$ (thus assuming $\beta_r = \beta_Z = 0$ in Eq.(5.26)), which is reasonable as long as the wave packet does not undergo large-amplitude motions in the excited state. For the simulation of the coordinate-independent quenching scenario, the original Gadzuk method (section 2.2.2.2) was used. In Fig.5.1 the expectation values $\langle r\rangle(\tau_R)$ and $\langle Z\rangle(\tau_R)$ are shown for the coordinates of a ground state wave packet evolving in the electronically excited state as functions of the residence time τ_R. Both surface models A and B are given. At $\tau_R = 0$, the expectation values are those of the ground state wave function $|0_g\rangle$, i.e, $\langle r\rangle(0) = \langle 0_g|r|0_g\rangle \approx r_{\min} = 1.16$ Å and $\langle Z\rangle(0) = \langle 0_g|Z|0_g\rangle \approx Z_{\min} = 2.16$ Å. For finite τ_R up to $\approx 10 - 15$ fs, the wave packet moves towards the surface –which is typical for an Antoniewicz-type scenario (see section 1.4)– and at the same time towards increasing NO bond length r. Due to the fact that the model is two-dimensional, the wave packet in the excited state does not move directly towards the Pt surface, but starts oscillating in the NO coordinate. Thus, it will reach the point from where higher desorption yields are achieved later than in a one-dimensional model, and consequently the lifetime τ of the excited state must be larger to obtain the same desorption probabilities. The oscillatory motion along the r coordinate becomes

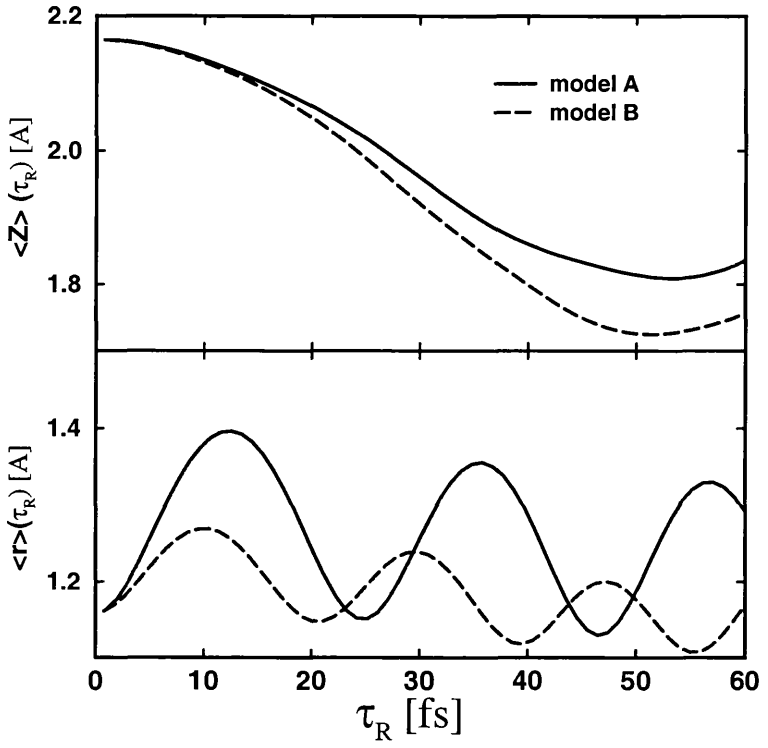

Figure 5.1: *Expectation values for the coordinates $\langle Z \rangle$ (upper panel) and $\langle r \rangle$ (lower panel) for an excited ground state wave function, transfered to the excited state to move there for a certain time τ_R . The solid curves are for model surface A, the dashed ones for model B. For $\tau_R < 5$ fs, the wave packet moves towards the surface and for longer τ_R away from it. In the two-dimensional model the wave packet does not move directly towards the Pt surface, but starts oscillating in the NO coordinate; the $\langle r \rangle$ expectation value oscillates with a period of $\approx$ 25 fs for model A and $\approx$ 19 fs for model B.*

visible at larger residence times, while $\langle Z \rangle$ steadily decreases up to the $\tau_R \approx 50$ fs when the wave packet is reflected from the repulsive wall of the potential at low adsorbate-surface distance Z. The amplitude of the $\langle r \rangle$ oscillation is considerably larger for surface model A (solid lines in Fig.5.1) than for model B (dashed lines). This indicates that upon return to $|g\rangle$ the wave packet in model A will be much more vibrationally excited than in model B. Also, because excited model B is less NO^- like, the vibrational period is shorter since $\omega_{NO} > \omega_{NO^-}$.

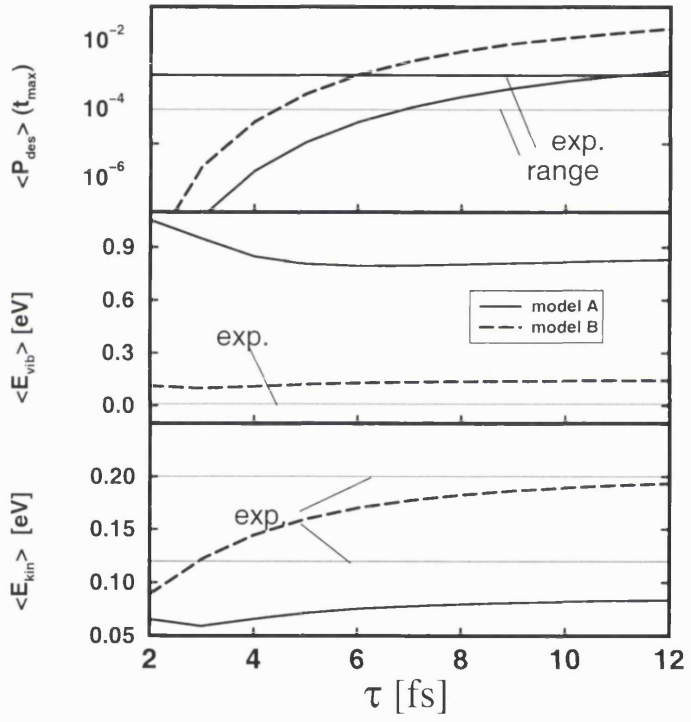

Figure 5.2: *Averaged desorption probabilities per excitation event $\langle P_{des} \rangle(t)$ (upper panel), averaged vibrational energies per desorbing particle $\langle E_{vib} \rangle(t)$ (middle panel) and averaged translational energies per desorbing particle $\langle E_{kin} \rangle(t)$ (lower panel), as a function of excited state lifetime, τ for DIET of NO from Pt(111) with a coordinate-dependent quenching rate. Shown are the results of the 2D models A (solid lines) and B (dashed lines) and experimental estimates values or ranges of values (horizontal thin lines; see text).*

After the averaging of N individual quantum trajectories for various τ_R (see Table 5.1) according to Eq.(2.33), the final expectation values for the properties of interest are obtained. Shown in Fig.5.2 is the averaged desorption probability per excitation event, $\langle P_{des} \rangle(t)$ (Eq.(5.18)), the averaged kinetic energy per desorbing particle, $\langle E_{kin} \rangle(t)$ (Eq.(5.23)) and the averaged vibrational energies per desorbing particle, $\langle E_{vib} \rangle(t)$ (Eq.(5.24)), as functions of τ. Both the results for model surfaces A and B are given, together with the experimental values (or estimates thereof) as horizontal lines. Experimentally, the desorption probability per excitation event is estimated to be in the order of 10^{-3} to 10^{-4} [31, 42], the kinetic energy is between $\langle E_{kin} \rangle \approx 0.12$ eV [28] and ≈ 0.20 eV [48, 49]. The experimental vibrational energy is $\langle E_{vib} \rangle = 0.04 \cdot 0.232$ eV $= 9.3$ meV [48, 49].

From the plot of the desorption probability in the upper panel of Fig.5.2, a lifetime of $\tau \approx 7$ - 12 fs can be estimated from model A to be compatible with the experiment, while the 2D model B implicates a shorter excited state lifetime of $\tau \approx 4$ - 6 fs. The lifetime predicted by model A in particular is significantly longer than that obtained by direct density matrix propagation within a 1D model (with only Z included) [31], where $\tau \approx 2$ - 3 fs was estimated. In the 2D models used in this work, larger lifetimes are needed to achieve reasonable desorption probabilities, because the excited state wave packet does not move straight along the desorption coordinate, but also along the NO mode.

From the lower panel of Fig.5.2, one similarly notes that the translational energies per desorbate are "reasonable" for surface model B, assuming $\tau \geq 3$ fs. However, for the 2D model A, the desorbates are translationally too "cold" at least by a factor of 2 as compared to experiment, irrespective of τ. At the same time, the computed vibrational excitation of the desorbing NO is much too strong (by a factor of ≈ 100) as shown in the middle panel of Fig.5.2. The vibrational excitation predicted by surface model B is also too high, but at least qualitatively correct (see below). In the following it is assumed that τ is between 3 and 6 fs for surface model B and $\tau =$ 10 fs for 2D model A, to account for experiment in an "optimal" way.

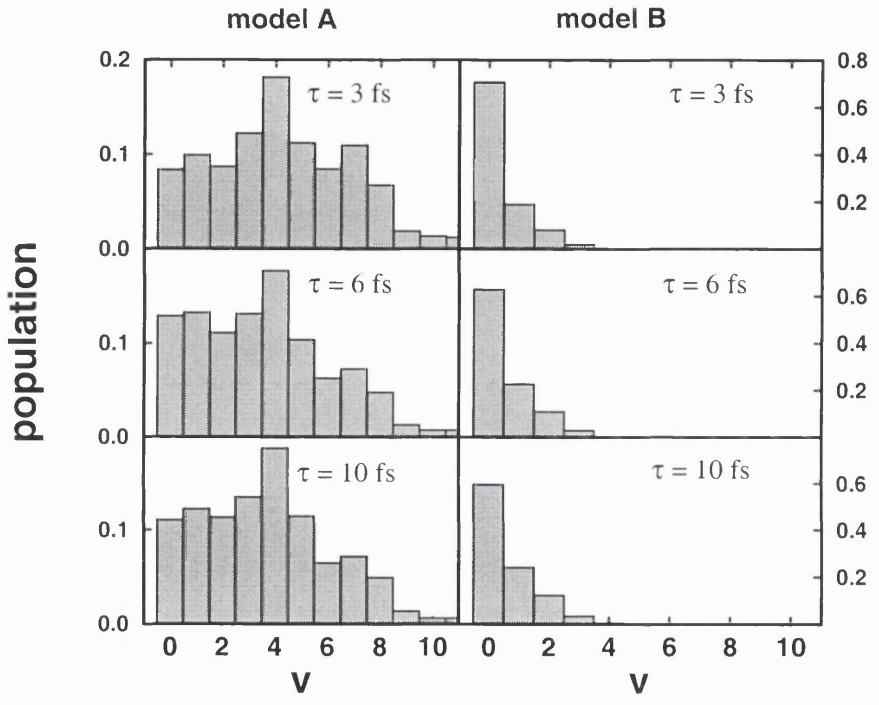

Figure 5.3: *Averaged vibrational state populations of desorbing NO, $P_v := \langle P_v \rangle(t)$ for DIET of NO from Pt(111) with coordinate-independent quenching. The left column is for DIET 2D model A, the right one for surface model B. In both cases, three lifetimes (τ = 3,6 and 10 fs) are considered. Qualitatively, the experimentally observed moderate vibrational excitation of the desorbates is reflected much better in 2D model B than surface model A.*

As mentioned above, the enormous vibrational excitation predicted by the 2D model A [60, 135, 136], was used as argument against the negative ion resonance model of the NO desorption from Pt(111).

In Fig.5.3 the vibrational state population of desorbing NO, $P_v := \langle P_v \rangle(t)$, is shown in the form of histograms for the 2D DIET models A and B. In both cases, three respective lifetimes (τ = 3,6 and 10 fs), are considered, where the first two cover the possible range for surface model B and the last is more appropriate for model A (see above). It is recognised that the moderate vibrational excitation found in experiment ($P_1/P_0 \approx 0.04; P_v/P_0 \approx 0 (v > 1)$, [48, 49]) is at least qualitatively met by the more realistic 2D model B. In contrast, model A for which an integer charge transfer had been assumed, fails completely, by even predicting a population inversion. These findings are almost independent of the particular choice of τ. Therefore, within the "asymptotic negative ion" picture (surface model B) there is no contradiction between the observed moderate vibrational excitation and the assumed charge transfer.

5.4.2 The effects of coordinate-dependent quenching

Even in the improved surface model B the computed vibrational excitation of the desorbates is somewhat overestimated. For τ = 3 fs, for example, the model predicts $P_1/P_0 = 0.26$, and $P_2/P_0 \approx 0.11$. The quantitative difference with experiment may be due to many reasons. First is the model character of the potentials, another one the reduced dimensionality of the dynamics. Rotations and frustrated translations will absorb some energy in a higher-dimensional approach. Further, it was shown in Ref.[60] that the coordinate-dependence of the decay rate $\Gamma_{ge}(r, Z)$ as expressed in Eq.(5.26), may cause further vibrational cooling of the desorbates.

Unfortunately, nothing is known about the r-dependence of $\Gamma_{ge}(r, Z)$. Also because the NO bond cannot be broken in contrast to the NO-surface bond at the energies considered here, just the effects of a finite range parameter β_Z along Z in

Eq.(5.26) are considered now.

Computationally, the treatment of coordinate-dependent quenching is done most efficiently using the generalized Gadzuk method (see section 2.2.2.3). To demonstrate how the generalized Gadzuk algorithm works in practice, in Fig.5.4 the numerically determined generalized Gadzuk weighting factors w_n are shown as a function of τ_{Rn} (see Eq.(2.45)) for the 2D surface model B. Exemplary, the parameters $1/\Gamma_{ge}^0 = 6$ fs, $\beta_r = 0$, $\beta_Z = 1.0$ Å^{-1} and $Z_{\min} = 2.16$ Å were chosen for Eq.(5.26).

The exponential decrease of Γ_{ge} with Z is reasonable in view of the exponentially decreasing overlap between adsorbate and metal orbitals [78, 117]. For $Z \to \infty$, $\Gamma_{ge} = 0$ because this corresponds to a stable NO^- ion separated from the positively charged metal. The parameters where chosen such that, at the Franck-Condon point ($Z = 2.16$ Å), the decay rate is identical to a coordinate-independent decay rate of $\Gamma_{ge}^0 = 1/6$ fs^{-1}. In the coordinate-independent scenario ($\beta_r = \beta_Z = 0$), the generalized Gadzuk weights are identical to those of the simple Gadzuk procedure ($w_n = \Gamma_{ge}^0 \cdot e^{-\tau_R \Gamma_{ge}^0} \cdot \Delta\tau_R$), as also demonstrated numerically in Fig.5.4. From the blow-up for large residence times τ_R in the lower panel of Fig.5.4 it can be seen that in the coordinate-dependent case the generalized Gadzuk weights are, for instance for $\tau_R \approx 40$ fs, smaller by a factor of about 2 than for coordinate-independent quenching. In general, from $\tau_R > 30$ fs the coordinate-dependent weights are smaller than the coordinate-independent ones. Since the weights are normalized, therefore at smaller τ_R the generalized Gadzuk weights have to be slightly larger than in the coordinate-independent case, making quantum jumps more probable for small τ_R.

After the averaging of the expectation values of the single quantum trajectories according to Eq.(2.44), the time-resolved desorption probability $\langle P_{des} \rangle(t)$ is obtained. As shown in Fig.5.5a, coordinate-dependent electronic quenching leads to a reduction of the yield by a factor of 2. This is due to the fact that in the coordinate-dependent case "trajectories" with smaller τ_R, for which $P_{des}(\tau_R)$ is small, have a larger weight. Within the Antoniewicz model this can be rationalised with the observation that that part of the wave packet closer to the metal surface (i.e. at shorter

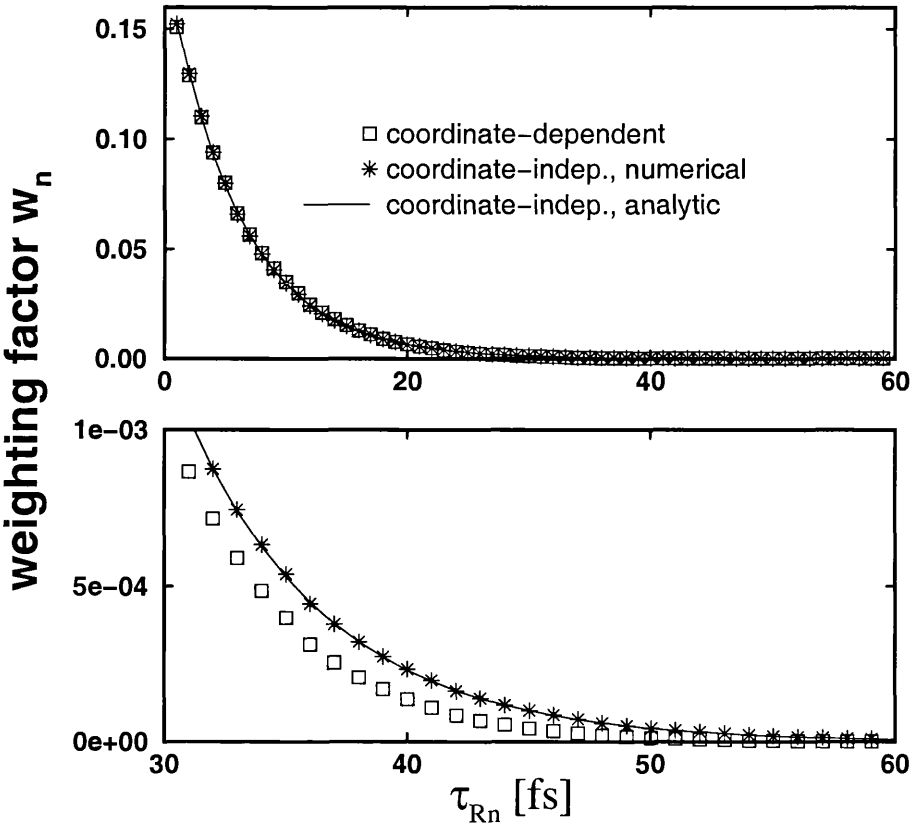

Figure 5.4: *The effects of coordinate-dependent quenching in DIET of NO from Pt(111). Shown are the numerically obtained Gadzuk weighting factors w_n as a function of τ_{Rn} for surface model B for $1/\Gamma^0_{ge} = 6$ fs, $\beta_r = 0$, $\beta_Z = 1.0$ Å^{-1} and $Z_{min} = 2.16$ Å in Eq.(5.26), respectively, as open squares. For the choice $\beta_Z = 0$ (coordinate-independent quenching) the analytic Gadzuk weights (solid line) and the numerically determined generalized Gadzuk weights (stars) are shown as well. The lower panel is a blow-up of the upper one, for larger residence times.*

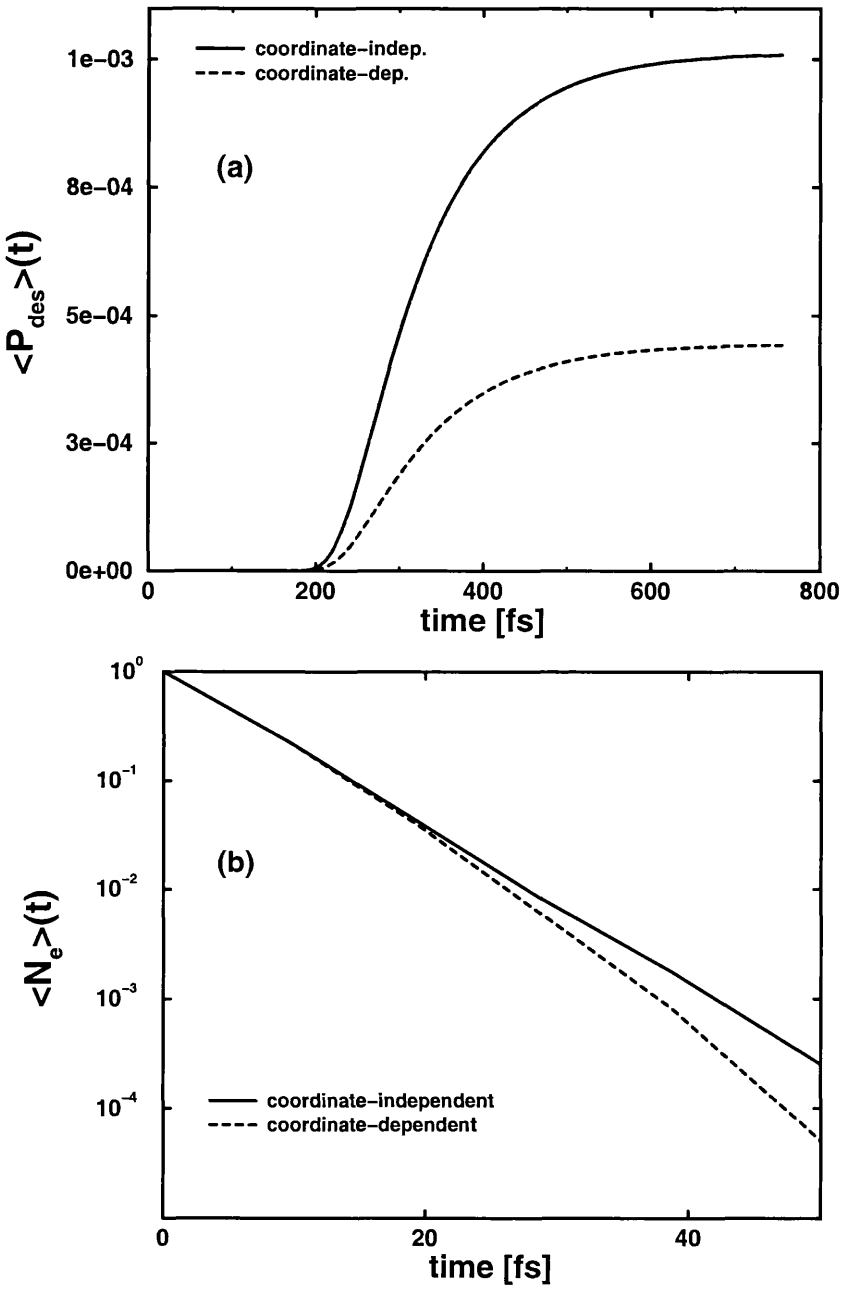

Figure 5.5: *The effects of coordinate-dependent quenching in DIET of NO from Pt(111). The solid curves are for 2D surface model B obtained with* $1/\Gamma^0_{ge} = 6$ *fs,* $\beta_r = 0$, $\beta_Z = 1.0$ Å^{-1} *and* $Z_{min} = 2.16$ Å *in Eq.(5.26), showing (a) the time-resolved desorption probability* $\langle P_{des} \rangle(t)$*, and (b) the corresponding decay of the excited state population* $\langle N_e \rangle(t)$ *(logarithmic scale). The dashed curves are (a)* $\langle P_{des} \rangle(t)$ *and (b) the excited state population* $\langle N_e \rangle(t)$ *for* $\beta_Z = 0$*, i.e., coordinate-independent quenching.*

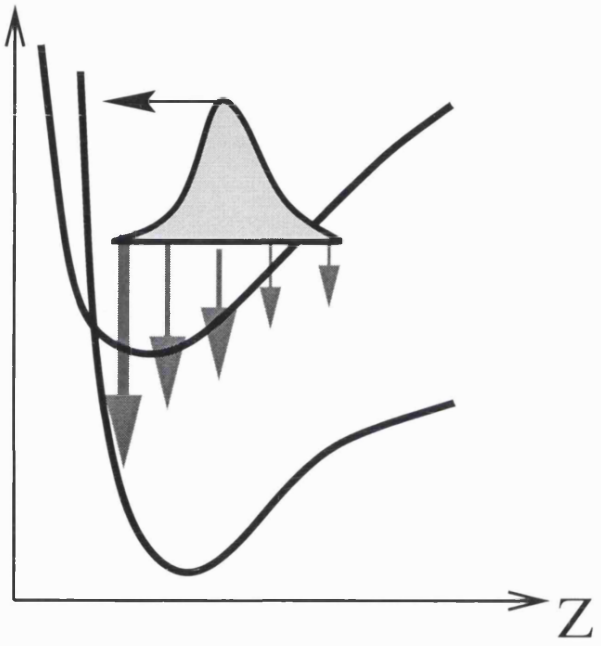

Figure 5.6: *Coordinate-dependent electronic quenching in the Antoniewicz model. The electronic relaxation is faster at short adsorbate-surface distances Z. Thus the wave packet has less chance to reach the steep repulsive wall of the electronic ground state, resulting in a reduced desorption probability.*

Z) is quenched most efficiently, so it has no chance to reach the steep repulsive wall of the electronic ground state opposite the desorption chanel which would cause desorption (see Fig.5.6). This finding is qualitatively different from that found for the MGR desorption scenario, where coordinate-dependence of the relaxation rate leads to significantly higher desorption probabilities (see section 3.2.4).

The decay of the resonance population $\langle N_e \rangle(t)$ is shown in Fig.5.5b. It appears only slightly different at larger times compared to the coordinate-independent relaxation scenario; for coordinate-dependent quenching the population decays somewhat faster. This is because of the smaller weighting factors for longer residence times and can be explained in a wave packet picture by the fact that the wave packet on the excited state moves towards shorter Z-values where the electronic quenching is more efficient than with a constant, coordinate-independent rate. The same effects were found in Ref.[31], using a 1D model and a different computational method. No significant effect of finite β_Z on the kinetic energy distribution of the desorbates and only small effects on their vibrational energies were found. Here, however, the inclusion of finite β_r could be essential to arrive at a more qualitative level of agreement with the experiment. Preliminary results by Finger and Saalfrank [60] have shown a substantial reduction of the overpopulation of higher NO vibrational states by also including the dependence of Γ_{ge} on r and further examinations are clearly necessary.

5.5 DIMET of NO from Pt(111)

5.5.1 Theoretical treatment of the DIMET process

The open system density matrix Lindblad approach and the direct and stochastic wave packet methods to solve the Liouville-von Neumann equation (2.10) (see section 2.2) can easily be generalized to treat desorption processes induced by multiple excitations/de-excitions (DIMET). For this, the initial condition

$$\hat{\rho}(0) = |g\rangle\langle g| \otimes |0_g\rangle\langle 0_g| \quad , \tag{5.27}$$

is chosen and the dissipative Lindblad functional has to be supplemented by a term accounting for the excitation of the adsorbate $|g\rangle \rightarrow |e\rangle$. The hot electron-mediated excitation is modelled by the corresponding Lindblad operator, $\hat{C}_2$:

$$\hat{C}_2 = \Gamma_{eg}(t)|e\rangle\langle g| \quad , \tag{5.28}$$

with $\Gamma_{eg}(t)$ being the transfer rate of nuclear density from the electronic ground to the excited state. The inclusion of the excitation in the dissipative part of Eq.(2.10) corresponds to the *indirect* nature of the excitation process and is in contrast to the photodesorption of H from Si(100) (see section 4), where the adsorbate excitation was assumed to be *direct* and included in the Hamiltonian.

The excitation rate is determined from the deexcitation rate $\Gamma_{ge}(r, Z)$ by the principles of detailed balance

$$\Gamma_{eg}(t) = \Gamma_{ge}(r, Z) \cdot e^{-\Delta V / k_B T_{el}(t)} \quad . \tag{5.29}$$

Detailed balance expresses the fact that the excitation and the deexcitation originate from the same metal-adsorbate coupling mechanism and are reversible microscopically.

The potential energy difference $\Delta V = V_e - V_g$ and the prefactor $\Gamma_{ge}(r, Z)$ make $\Gamma_{eg}(t)$, in principle, coordinate-dependent. Under the assumption that the dominant excitation region is localized around the ground state equilibrium distance r_0, Z_0,

the coordinate-dependence of ΔV is neglected and a constant $\Delta V = V_e(r_0, Z_0) - V_g(r_0, Z_0)$ is assumed. For simplicity, but also because coordinate-dependent quenching causes no order-of-magnitude effects for NO/Pt(111), a coordinate-independent decay rate $\Gamma_{ge}(r, Z) = \Gamma^0_{ge}$ is chosen, which makes the excitation operator $\Gamma_{eg}(t)$ coordinate-independent.

The time dependence of $\Gamma_{eg}(t)$ arises from the fact that a pulsed laser experiment is to be modelled. The modelling includes a time dependent electronic temperature profile $T_{el}(t)$, which can be calculated semi-microscopically using a coupled diffusion equation formalism containing laser and substrate characteristics [139]. In this work, a model form suggested in Ref.[139] is used instead:

$$T_{el}(t) = T_m \cdot \frac{e^{-t/\tau_1}}{e^{-t/\tau_2} + 1} \cdot g(t) \quad , \tag{5.30}$$

with $g(t) := 1 - \left[e^{(t-\tau_2)/\tau_3} + 1\right]^{-1}$. Eq.(5.30) is used as a rough analytical representation for the response of an electron gas to a (sub–)ps laser pulse. It is a function which starts from $T_{el} \approx 0$, reaches a peak T_{max} ($\neq T_m$) of several thousands of K after a few hundred fs and then falls off on the ps–timescale (see Fig.5.8). The parameters τ_1, τ_2, τ_3 used in this work are given in Table 5.1, while T_m is varied parametrically to simulate different laser fluences.

The treatment of DIMET by the direct method for solving the Liouville-von Neumann equation (2.10) is no more complicated than the treatment of DIET. However, it is numerically too costly because the two dimensions considered result in a density matrix too large in memory requirements. Thus, the Liouville - von Neumann equation (2.10) is solved by the stochastic Monte Carlo Wave Packet Method (MCWP) introduced in section 2.2.2.1. The MCWP method, however, is numerically much harder for DIMET than for DIET. The presence of the excitation term leads to an effective, non-Hermitian Hamiltonian

$$\hat{H}' = \hat{H} - \frac{i\hbar}{2}[\Gamma_{ge}|e\rangle\langle e| + \Gamma_{eg}(t)|g\rangle\langle g|] \quad , \tag{5.31}$$

and to quantum trajectories corresponding to P-fold excitation/deexcitation cycles,

which are in the case of coordinate–independent transition rates of the type ($t > \sum_{i=1}^{2P} \tau_i$):

$$
\begin{aligned}
|\psi(t;\tau_0,\tau_1,\ldots,\tau_{2P-1},\tau_{2P})\rangle \;=\; & e^{-i\hat{H}_g(t-\tau_{2P})/\hbar}|g\rangle \\
& \times\langle e|e^{-i\hat{H}_e(\tau_{2P}-\tau_{2P-1})/\hbar}\rangle e|\langle g|\cdots|e\rangle \\
& \times\langle g|e^{-i\hat{H}_g(\tau_3-\tau_2)/\hbar}|g\rangle\langle e|e^{-i\hat{H}_e(\tau_2-\tau_1)/\hbar}|e\rangle \\
& \times\langle g|e^{-i\hat{H}_g\tau_1/\hbar}|0_g\rangle \quad . \qquad (5.32)
\end{aligned}
$$

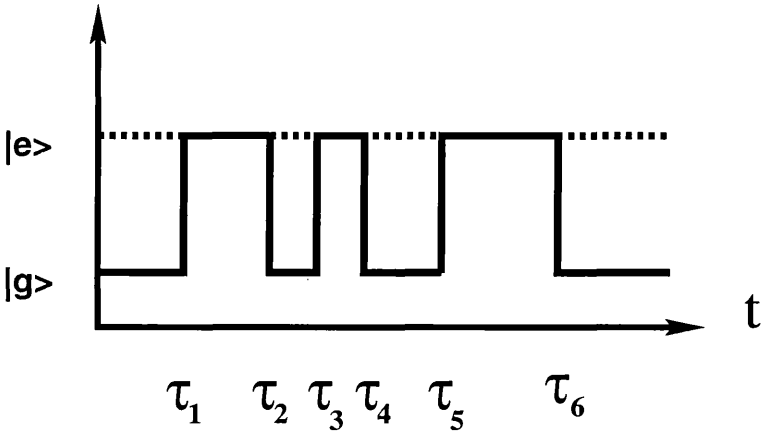

Figure 5.7: *DIMET of NO from Pt(111). Sketch of an P-fold excitation/deexcitation cycle for $P = 3$. The $|g\rangle\langle e|$ and $|e\rangle\langle g|$ operators in Eq.(5.32) enforce transitions between both surfaces.*

Here, the $|g\rangle\langle e|$ and $|e\rangle\langle g|$ operators enforce transitions between both surfaces. The "odd minus even" residence time intervals $\tau_{2k+1}-\tau_{2k}$ $[k = 0,\ldots,P-1\ ;\ (\tau_0 = 0)]$ and the interval $t - \tau_{2P}$ correspond to situations where the wave packet resides on the ground state surface; the "even minus odd" residence time intervals $\tau_{2k} - \tau_{2k-1}$ $(k = 1,\ldots,P)$ denote propagations in the excited state. The situation is sketched in Fig.5.7 for the example $P = 3$.

As explained in section 2.2.2.1, the expectation values for the randomly selected quantum trajectories (which are independent of the initial propagation τ_0 on $|g\rangle$),

$$
A_n(t) = \langle\psi(t;\tau_{1n},\tau_{2n},\ldots,\tau_{2P_n})|\hat{A}|\psi(t;\tau_{1n},\tau_{2n},\ldots,\tau_{2P_n})\rangle \quad , \qquad (5.33)
$$

are simply averaged over using Eq.(2.30).

5.5.2 DIMET dynamics

The time evolution of the electronic temperature, Eq.(5.30), and the electronic excitation rate, Eq.(5.28) are shown in Fig.5.8. The electronic temperature rises within $\approx$ 140 fs to the respective peak value (see Table 5.2) and decays to zero in about 1 ps.

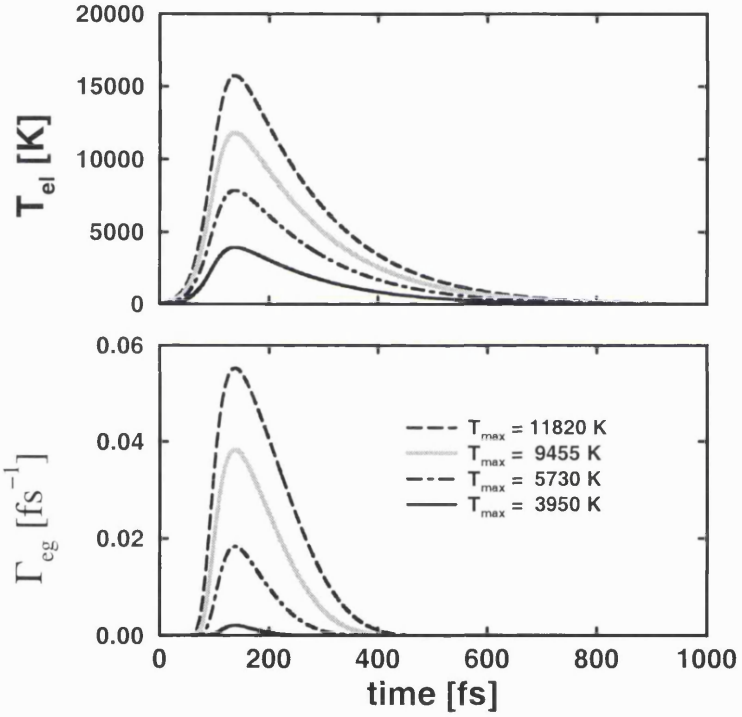

Figure 5.8: *The electronic temperature profile (upper panel) and the electronic excitation rate $\Gamma_{eg}(t)$ (lower panel) as a function of time t for the electronic temperature considered (see Table 5.2. The electronic temperature profile induces an electronic excitation rate which depends exponentially on the electronic temperature.*

The choice of parameters for the electronic temperature profile (see Table 5.1) is motivated by computational reasons. The peak temperatures are chosen rather high to reach reasonable converged results with a feasible number of Monte Carlo

quantum trajectories. Four peak electronic temperatures, between $\approx$ 3900 K and $\approx$ 11800 K, have been considered, where the latter value is by about a factor of two above what has been realized experimentally so far [131].

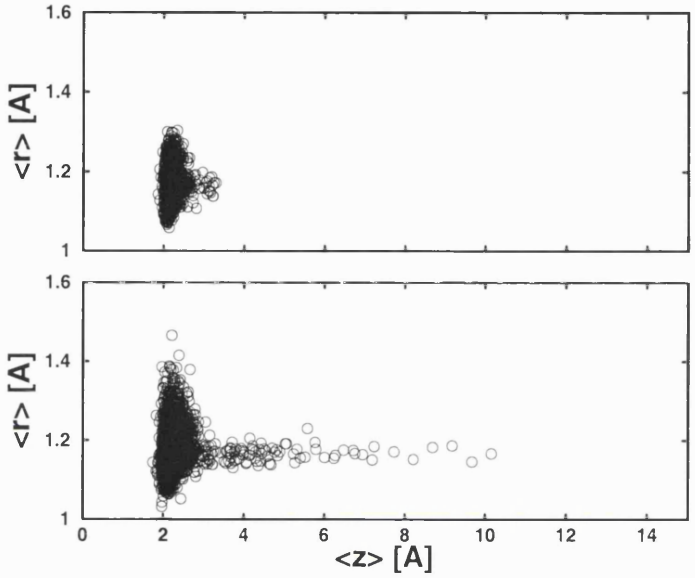

Figure 5.9: *DIMET of NO from Pt(111). Expectation values in the r and Z coordinate of all trajectories at equidistant time steps of 36.3 fs. The expectation values for two peak electronic temperatures are given: in the upper panel for* T_{max} = 5730 K (T_m = 20000 K) *and in the lower panel for* T_{max} = 11820 K (T_m = 41255 K). *For the higher electronic temperature, the sampled space is larger than for the lower one, in particular along Z, and thus more quantum "trajectories" will lead to desorption.*

The sampled coordinate space for the MCWP calculations within the DIMET scenario is shown in Fig.5.9 for T_{max} = 5730 K (upper panel) and T_{max} = 11820 K (lower panel) respectively. Every 36.3 fs, a snapshot of the position of the wave packet has been taken for each trajectory. All the snapshots are displayed together. It can be seen that for a maximum electronic temperature of 11820 K the sampled space is larger than for T_{max} = 5730 K, in particular along Z, and thus more molecules will desorb.

T_{max} [K]	T_m [K]	N
3950	13787	4000
5730	20000	3000
9455	33000	2000
11820	41255	2000

Table 5.2: *The electronic peak temperatures T_{max}, the corresponding T_m values for Eq.(5.30) and the number of MCWP quantum trajectories N for DIMET of NO from Pt(111).*

Depending on T_{max}, different number N of quantum trajectories was chosen to account for the slower statistical convergence in the low-T_{max} (low-probability) regime. The electronic peak temperatures T_{max} considered and the corresponding T_m values for Eq.(5.30) are given in Table 5.2 together with the corresponding maximum number of MCWP quantum trajectories N.

Increasing the laser fluence leads to higher electronic peak temperatures T_{max} and thus, according to Eq.(5.29), to a non-linear increase of the excitation rate $\Gamma_{eg}(t)$ (see Fig.5.8). Because the lifetime of the excited state is so short, the non-linear increase of the excitation rate $\Gamma_{eg}(t)$ considerably enhances the chance for multiple-excitations, and therefore leads to the "DIMET hallmarks" referred to in section 1.2. Using the Monte Carlo wave packet method (see section 2.2.2.1), the number of excitations per quantum trajectory can be counted and hence the term "multiple" be quantified [31].

In Fig.5.10a the average number of excitations per laser pulse,

$$\langle m \rangle = \frac{\sum_{m=0} ms(n)}{N} \quad , \tag{5.34}$$

is shown for 2D model B and a quenching rate $\Gamma_{ge} = \Gamma_{ge}^0 = 1/6$ fs^{-1}, where m in Eq.(5.34) is the number of excitations, $s(m)$ is the number of m-fold excitations per quantum trajectory and N is the number of MCWP trajectories.

From test calculations it was estimated that, except for the lowest T_{max}, the

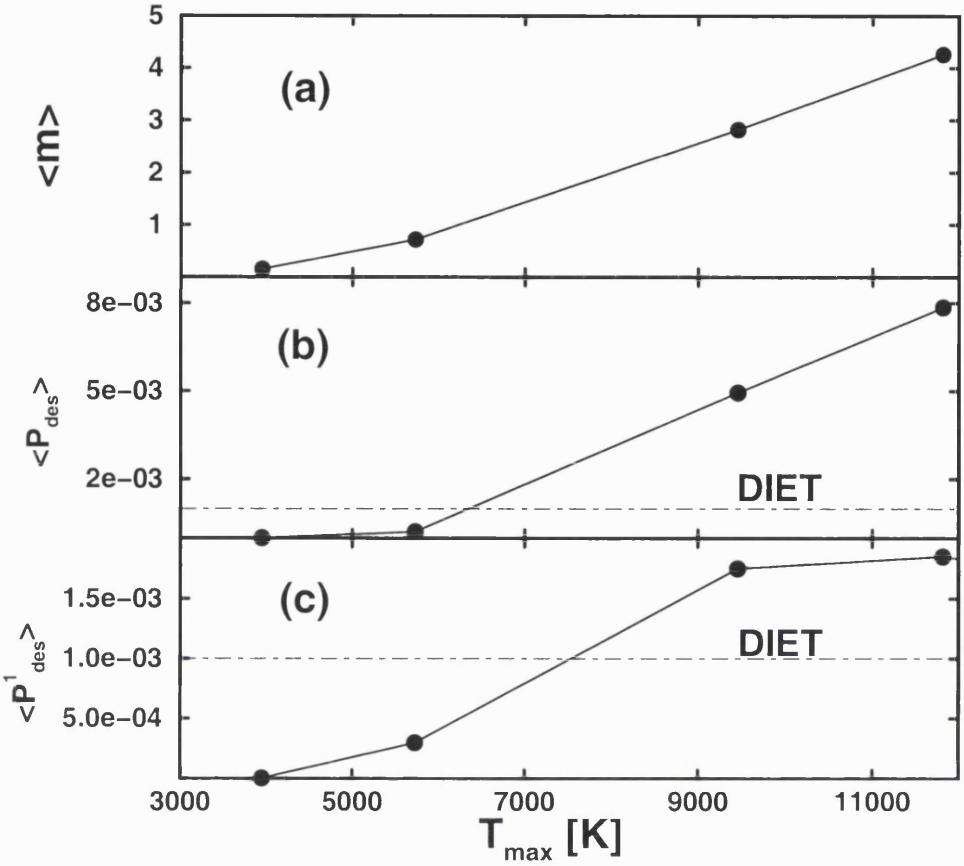

Figure 5.10: *DIMET of NO from Pt(111) within 2D model B and coordinate-independent transition rates* ($\Gamma^0_{ge} = 1/6\ fs^{-1}$). *Shown are several computed quantities or observables of the desorbates, as a function of the maximum electronic temperature* T_{max}: *In (a) the average number of excitations per laser pulse* $\langle m \rangle$, *in (b) the averaged desorption probability* $\langle P_{des} \rangle(t)$ *and in (c) the averaged desorption probability per excitation event* $\langle P^1_{des} \rangle$. *For the latter two cases, also the DIET value is given as a horizontal, dot-dashed line. The electronic peak temperatures* T_{max} *considered are (the corresponding* T_m *values for Eq.(5.30) in brackets):* $T_{max} = 3950\ K$ *(*$T_m = 13787\ K$*), 5730 (20000), 9455 (33000), and 11820 (41255)* K. *For these cases,* N= 4000, 3000, 2000 *and 2000 MCWP trajectories were used, to assure that in all cases the estimated error (based on the scattering of computed data) is less than 10 %. (In the case of the lowest temperature, the estimated relative error is around 30 %.)*

statistical errors made for different computed properties, are of the order of ± 10 %. It is seen that the average excitation number $\langle m \rangle$ increases as T_{max}, i.e., as laser fluence, increases. For the lower T_{max}, $\langle m \rangle$ increases slightly super-linear and quasi-linear for the larger T_{max} (> 9000 K).

Closer inspections for low T_{max} show that, in most cases, no excitation at all takes place. For example, for T_{max} = 3950 K (T_m = 13787 K), out of N = 4000 trajectories only ≈ 500 lead to a transition $|g\rangle \rightarrow |e\rangle$. This observation can be used to accelerate the MCWP algorithm considerably. Namely, for coordinate-independent transition rates the norm loss $\delta p(t+\Delta t)$ due to the upward operator $\hat{C}_2$ in Eq.(5.28) is given analytically as

$$\delta p(t+\Delta t) = 1 - e^{-\int_t^{t+\Delta t} \Gamma_{eg}(t')dt'} \quad . \tag{5.35}$$

Since the time-evolution of the stationary vibrational ground state wave packet $|0_g\rangle$ in the ground electronic state is trivial, the numerical propagation of the wave packet has to be carried out only from that time on when a random number $\varepsilon \in [0,1]$ becomes larger than $\delta p(t+\Delta t)$, i.e., when the wave packet indeed performs a quantum jump.

In Fig.5.10(b) the desorption probability $\langle P_{des} \rangle(t)$ of NO from Pt(111) is shown. Further, in Fig.5.11(a) the average kinetic energies per desorbate $\langle E_{kin} \rangle(t)$ and in Fig.5.11(b) the average vibrational energies $\langle E_{vib} \rangle(t)$ for the various T_{max} studied are given. A super-linear increase of $\langle P_{des} \rangle(t)$ can be clearly observed for lowest three T_{max} < 9000 K as well as a quasi-linear increase of $\langle E_{kin} \rangle(t)$ with peak electronic temperature. The computed superlinearity of the desorption yield with peak temperature will translate in a somewhat less pronounced increase of $\langle P_{des} \rangle(t)$ with the laser fluence $\mathcal{F}$ because T_{max} is expected to increase approximately proportional to the square root of $\mathcal{F}$ [140]. Therefore, the experimentally observed distinct power law scaling [28] cannot be fully accounted for by the model. This was also unexpected since, for a quantitative agreement, a more realistic parametrization of the hot-electron function $T_{el}(t)$ is essential.

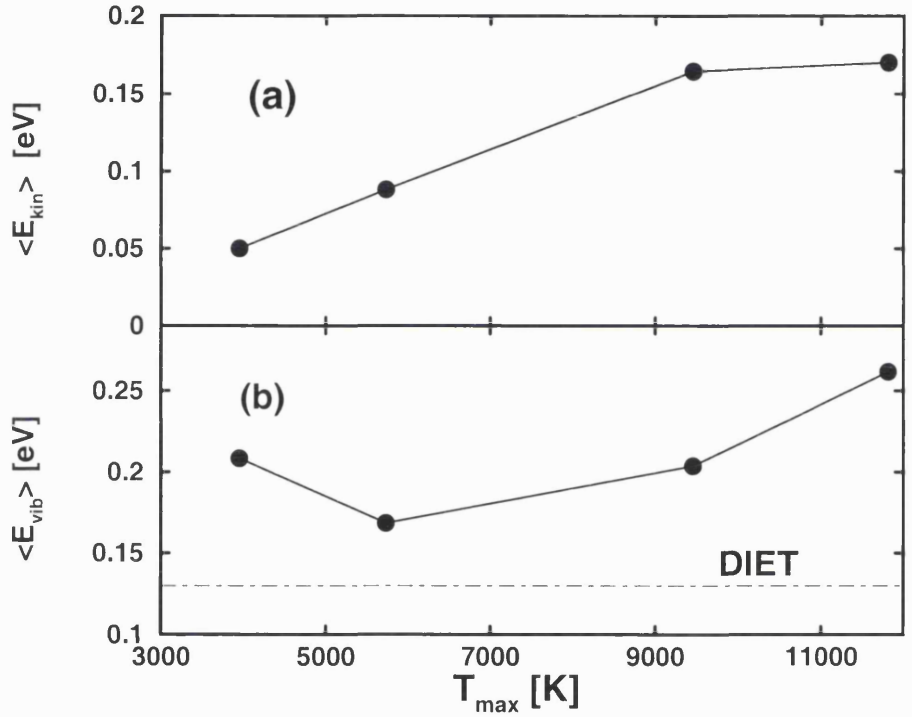

Figure 5.11: *The same as Fig.5.10 for (a) the averaged kinetic energies* $\langle E_{kin} \rangle(t)$ *and (b) the averaged vibrational energies of the desorbates* $\langle E_{vib} \rangle(t)$*; for the latter, the theoretical DIET value (see also Fig.5.3) is shown as a horizontal, dot-dashed line.*

The "linear regime" for $\langle m \rangle$ at large T_m (T_{max}) (Fig.5.10(a)), translates into a slower, quasi-linear increase of $\langle P_{des} \rangle$, and a "levelling off" of the kinetic energies with T_{max} (Fig.5.11(a)). This theoretical prediction holds for very large, perhaps impractically large peak temperatures. However, the observed behaviour is reasonable because the desorption probability cannot increase forever according to a power law, but must level off at some point to approach a finite value. The increase of the desorption in DIMET probability relative to DIET is demonstrated in Fig.5.10(c). There, the desorption probability *per excitation event*

$$\langle P^1_{des} \rangle := \frac{\langle P_{des} \rangle}{\langle m \rangle} \quad . \tag{5.36}$$

is shown as a a function of T_{max}. It is seen that for large T_{max}, $\langle P^1_{des} \rangle$ is indeed much larger than $\langle P^1_{des} \rangle$(DIET) $\approx 1 \cdot 10^{-3}$, which is included in Figs.5.10(b) and 5.10(c) as a dashed horizontal line. It should be noted that even at much lower T_{max}, the DIMET process is expected to lead to higher desorption yields than DIET because only a small fraction of adsorbates will actually be excited in DIET [42]. The results suggest that at high enough fluences, DIMET is even more efficient than DIET when in both cases one excitation took place. Finally, $\langle P^1_{des} \rangle$ is observed to increase somewhat with increasing T_{max}, a "synergetic effect" already found in the 1D model [31].

Concerning the vibrational energies per desorbate, $\langle E_{vib} \rangle(t)$ (Fig.5.11(b)), one finds for all cases studied that in the DIMET case the vibrational excitation is always larger than for the DIET scenario (dashed horizontal line in Fig.5.11(b)), in agreement with experiments [131, 132]. Further, as a general trend $\langle E_{vib} \rangle(t)$ increases with increasing T_{max}.

5.6 Summary and conclusion

The photodesorption of NO from Pt(111) has been investigated for the DIET (single excitation limit) and DIMET (multiple excitation limit) process within a two-

dimensional model, using a Markovian open system density matrix approach for the simulation of the desorption dynamics.

Concidering the DIET dynamics, it was found that the negative ion resonance model makes sense also for NO desorbing from metals, as long as the transfer of a full electron is assumed to happen only *asymptotically*, i.e., for $Z \to \infty$. The excited state lifetime is estimated to be ultrashort with $\tau < 10$ fs, in agreement with a previous 1D model [31]. Coordinate-dependence of the quenching rate along Z slightly decreases the desorption probability, while a coordinate-dependence of Γ_{ge} along r leads to vibrationally cooler products [60]. In the 2D "asymptotic negative ion resonance model", the desorption probabilities and kinetic and vibrational energies of the desorbates are qualitative, sometimes even in quantitative agreement with experimental data [48, 49, 28].

In the DIMET case, the experimentally known "DIMET hallmarks" [28] (larger desorption yields, scaling of yields, translational and vibrational energies with laser fluence) are at least qualitatively accounted for. For very large electronic peak temperatures (laser fluences), a "saturation regime" for those observables at very large laser fluences is predicted.

Future work should concentrate on several aspects. More reliable excited state potentials and their lifetimes are required to achieve satisfying quantitative agreement between theory and experiment. It it also important to use more realistic $T_{el}(t)$ curves [131] and to extend the model to multi-dimensions. In particular, the experimentally observed, substantial rotational excitation of the desorbates [48, 49] should be accounted for.

Chapter 6

Final summary and conclusions

This thesis is focused on the theoretical modelling of stimulated desorption processes of adsorbate-surface systems. The underlying theme is the implication of transient excited intermediates on the dynamics and the mechanism of bond breaking in complex systems.

In the first part of this thesis, section 1, a short introduction to general aspects of surface chemistry is given. Basic features of excitation and desorption processes in condensed phase are discussed and simple models for their description introduced.

In section 2, theoretical models and methods relevant to the applications in this work are reviewed in general. This includes open system density matrix theory and different quantum dynamical approaches to solve the underlying dissipative Liouville - von Neumann equation.

Various aspects of STM induced desorption are investigated and discussed for Si(100)-(2x1):H(D) in section 3. Results obtained by quantum mechanical wave packet and density matrix propagation, as well as classical methods are presented and compared to experiment.

Laser induced desorption of H(D) from Si(100)-(2x1) is treated in section 4 and possibilities for an active control of the photodesorption outcome are suggested.

In section 5, a two dimensional model is applied to the photodesorption of NO

from a Pt(111) surface. Results are represented which confirm the experimental observation that the desorption outcome is substantially different if a pulsed (fs) laser is used rather than a cw (ns) laser.

All induced processes considered have in common a theoretical description with relatively simple two state models. MGR and Antoniewicz type models have been adopted and extended to make predictions and simulations of non-adiabatic desorption systems of actual interest. While quantum effects and a proper treatment of electronic (and sometimes vibrational) relaxation are accounted for, the simplicity of the original MGR and Antoniewicz models is largely retained. This simplicity allows for the investigation of various, often opposing trends during the non-adiabatic surface reactions and despite the simplifications involved, the presented model studies give already reliable basic trends.

However, the nature of relaxation and excitation processes involved in STM or laser driven surface reactions and the eventually following bond breaking is most of the time not simple. Hence, effects neglected in the modelling may be important for quantitative predictions. Multi-dimensionality, the participation of more than one electronically excited state, an explicit inclusion of vibrational relaxation and a more detailed treatment of the excitation processes involved are issues which have to be addressed in the future. A very important factor is the calculation of reliable potential energy surfaces, in particular for the excited states. There is also a need for efficient numerical methods, for example because of the heavy scaling of density matrix calculations. Effective numerical techniques are essential not only for the treatment of complex surface reactions but also for the modelling of other process where a high number of degrees of freedom needs to be considered, e.g. in biochemistry.

Various groups are already working on those problems and towards possible improvements in the direction of more complete and even larger system simulations, aiming at a quantitative comparison with experimental results. Nevertheless, due

to the complexity of processes like non-adiabatic dynamics at solid surfaces, it is to expect that simple models, like the ones introduced and used in this work, will continue to be most useful in surface science, both as a source for a general physical insight and as a starting point for a more sophisticated treatment.

Appendix A

Numerical solution of the nuclear Schrödinger equation

A.1 The DVR method for the computation of eigenstates and eigenenergies

The numerical solution of the time-independent Schrödinger equation for the calculation of the (vibrational) system eigenstates requires a discretisation of the respective wave functions and operators in configuration space. The task of an efficient coordinate discretisation is to construct a preferably small grid $x_1, ..., x_G$, so that by representing the Hamiltonian and the wave function on this grid, the one dimensional eigenvalue problem

$$\left[-\frac{\hbar^2}{2\mu}\frac{\partial^2}{\partial x^2} + V(x)\right]|\Psi_\nu\rangle = E_\nu|\Psi_\nu\rangle \tag{A.1}$$

becomes a matrix eigenvalue problem

$$\begin{pmatrix} H_{11} & \dots & H_{1G} \\ \vdots & & \vdots \\ H_{G1} & \dots & H_{GG} \end{pmatrix} \begin{pmatrix} \psi_1 \\ \vdots \\ \psi_G \end{pmatrix}_\nu = E_\nu \begin{pmatrix} \psi_1 \\ \vdots \\ \psi_G \end{pmatrix}_\nu \quad . \tag{A.2}$$

In this work, the *Discrete Variable Representation* (DVR) method was used for the coordinate discretisation. This method, based on earlier works by Harris [141] and Dickinson [142], was introduced by Light and co-workers [143, 144] in chemical physics for solving the time-independent Schrödinger equation. The idea of the *sinc function* DVR method [89] used in this work is very simple and has a universal character. The Hamilitonian matrix and all aspects of the calculations have no explicit reference to an underlying basis from which the DVR comes and involve only the grid points themselves.

For a one-dimensional system with coordinate x restricted to an interval (a, b) the kinetic energy operator is

$$\hat{T} = -\frac{\hbar^2}{2\mu}\frac{d^2}{dx^2} \quad . \tag{A.3}$$

Using an equidistant grid $\{x_i\}$

$$x_i = a + (b-a)i/G\,, \quad i = 1, ..., G-1 \tag{A.4}$$

the basis functions ϕ_i for a uniform grid are Fourier–functions (i.e. eigenfunctions of a particel-in-a-box):

$$\phi_g(x) = \sqrt{\frac{2}{b-a}} \cdot sin\left[\frac{g\pi(x-a)}{b-a}\right], \quad g = 1, ..., G-1 \quad . \tag{A.5}$$

Under the assumption that the wave functions vanish at the interval endpoints a and b, one obtains $G-1$ functions and $G-1$ grid points. The grid point representation of the kinetic energy, or DVR, is then given by

$$T_{ij} = -\frac{\hbar^2}{2\mu}\Delta x \sum_{g=1}^{G-1} \phi_g(x_i)\phi_g''(x_j) \tag{A.6}$$

where $\Delta x = (b-a)/G$ is the grid spacing. With Eq.(A.5) one so obtains

$$T_{ij} = -\frac{\hbar^2}{2\mu}\left(\frac{\pi}{b-a}\right)^2 \frac{2}{G}\sum_{g=1}^{G-1} g^2 sin\left(\frac{g\pi i}{G}\right) sin\left(\frac{g\pi j}{G}\right) \quad . \tag{A.7}$$

As shown by Colbert and Miller [89], this becomes for $i \neq j$

$$T_{ij} = -\frac{\hbar^2}{2\mu}\frac{(-1)^{i-j}}{(b-a)^2} \cdot \frac{\pi^2}{2}\left\{\frac{1}{sin^2[\pi(i-j)/2G]} - \frac{1}{sin^2[\pi(i+j)/2G]}\right\} \tag{A.8}$$

For the diagonal elements one obtains accordingly

$$T_{ii} = -\frac{\hbar^2}{2\mu}\frac{1}{(b-a)^2}\cdot\frac{\pi^2}{2}\left[(2G^2+1)/3 - \frac{1}{sin^2(\pi i/G)}\right] \quad . \tag{A.9}$$

As it is with all DVR methods, the potential energy matrix is diagonal

$$V_{ij} = V(x_i)\delta_{ij} \tag{A.10}$$

and with the sinc-function DVR, a simple expression for the kinetic energy matrix is obtained. Considering for example the special case of an interval $(a,b) = (-\infty,\infty)$. In this case, a finit grid spacing $\Delta x = (b-a)/G$ requires that $G \to \infty$ also. With the grid as defined in Eq.(A.4), it is also $i+j \to \infty$, but $i-j$ is finit. Thus Eq.(A.8) becomes

$$T_{ij} = \frac{\hbar^2(-1)^{i-j}}{2\mu\Delta x^2}\left\{\begin{array}{ll} \pi^2/3\,, & i=j \\ \frac{2}{(i-j)^2}\,, & i\neq j \end{array}\right\} \quad . \tag{A.11}$$

The resulting Hamiltonian is greatly simplified and the Hamiltonian matrix sparse, which allows efficient diagonalisation. The application of the sinc function DVR for other intervals, e.g. $[0,\infty]$ or $[0,\pi]$ for systems described in polar coordinates is straightforward and described by Colbert and Miller as well [89].

To compute the eigenvalues and eigenenergies of the eigenvalue problem A.2, an explicit grid has to be chosen, i.e. a step size Δx and a maximum index G, which determines the grid limits $x_{min} = -G\Delta x$ and $x_{max} = G\Delta x$, have to be defined. For this, a maximum energy E_{max} is fixed, up to which the eigenvalues and -vectors should be calculated. The extent of the grid is then chosen so that $V(x_{max}) > E_{max}$ and $V(x_{min}) \gg E_{max}$. The step size Δx results from the observation that wave functions are well represented on a grid if 3-4 grid points N_B are used per De Broglie wave length λ_{min} of E_{max}

$$\lambda_{min} = \frac{2\pi\hbar}{\sqrt{2\mu E_{max}}} \tag{A.12}$$

$$\Longrightarrow \Delta x = \frac{\lambda_{min}}{N_B} \quad . \tag{A.13}$$

A.2 The split-operator propagator

The time dependent Schrödinger equation

$$i\hbar\frac{\partial}{\partial t}|\Psi(t)\rangle = \hat{H}|\Psi(t)\rangle \quad . \tag{A.14}$$

is a first-order differential equation in time. The Hamiltonian $\hat{H}$ is a sum of an operator $\hat{T}$ for the kinetic energy and an operator $\hat{V}$ for the potential energy. $\hat{H}$ is given in one dimension as

$$\hat{H} = \hat{T} + \hat{V} \tag{A.15}$$

$$\hat{T} = \frac{\hat{p}^2}{2\mu} = -\frac{\hbar^2}{2\mu}\frac{\partial^2}{\partial x^2} \quad . \tag{A.16}$$

The initial (one dimensional) wave function $|\Psi(x;t=0)\rangle$ is represented on a discrete grid with G equidistant grid points in configuration space. The potential energy operator $\hat{V}$ is diagonal in configuration space and the calculation of $\hat{V}|\Psi\rangle$ is a simple multiplication of $|\Psi(x)\rangle$ with the potential $V(x)$ on every coordinate x. The kinetic energy operator $\hat{T}$ is diagonal in momentum space. Thus, for the spatial derivative, the wave function is transformed to momentum space by FFT (*Fast Fourier Transform*). There, the spatial derivative corresponds to a simple multiplication with the square of the momentum coordinate and is thus numerically simple. After the multiplication, the resulting wave function is back-transformed to coordinate space.

To get the time derivative of Eq. A.14, the *split operator technique* by Feit and Fleck [77] was used in this work. The wave function $|\Psi(x,t)\rangle$ is propagated in discrete time steps Δt up to a final propagation time t_f. The wave function at time $t+\Delta t$ is calculated from the wave function at time t using the short-time propagator $\hat{U}(\Delta t)$ according to (atomic units)

$$|\Psi(t,\delta t)\rangle = e^{-i\hat{H}\Delta t}|\Psi(t)\rangle = \hat{U}(\Delta t)|\Psi(t)\rangle \quad . \tag{A.17}$$

In the split-operator method, $\hat{U}(\Delta t)$ can be approximated by

$$\hat{U}(\Delta t) = e^{-i\hat{H}\,\Delta t} \approx e^{-\frac{i}{2}\hat{V}\,\Delta t}\; e^{-i\hat{T}\,\Delta t}\; e^{-\frac{i}{2}\hat{V}\,\Delta t} + O(\Delta t^3) \quad . \tag{A.18}$$

The propagation scheme is norm conserving since only unitary operators are involved.

Appendix B

Time evolution of the density matrix elements

The elements of the density matrix result from the action of the Liouvillian superoperator $\mathcal{L}$ on the density $\hat{\rho}_s$. With the Lindblad operators

$$\hat{C}_{ij} = \sqrt{\Gamma_{ij}}|i\rangle\langle j| \tag{B.1}$$

the Liouville - von Neumann equation (2.10) ($\frac{\partial}{\partial t}\hat{\rho}_s = \dot{\hat{\rho}}_s$) becomes

$$\dot{\hat{\rho}}_s = -\frac{i}{\hbar}[\hat{H}_s, \hat{\rho}_s] + \sum_{i \neq j}\left(\hat{C}_{ij}\hat{\rho}_s\hat{C}_{ij}^{\dagger} - \frac{1}{2}[\hat{C}_{ij}^{\dagger}\hat{C}_{ij}\hat{\rho}_s]_+\right) \tag{B.2}$$

and the change of the matrix elements ρ_{nm} in time is given by

$$\begin{aligned}\langle n|\dot{\hat{\rho}}_s|m\rangle &= -\frac{i}{\hbar}\langle n|(\hat{H}_s\hat{\rho}_s - \hat{\rho}_s\hat{H}_s)|m\rangle \\ &+ \sum_{i \neq j}\langle n|\left(\Gamma_{ij}|i\rangle\langle j|\hat{\rho}_s|j\rangle\langle i| - \frac{1}{2}\Gamma_{ij}(|j\rangle\langle i|i\rangle\langle j|\hat{\rho}_s + \hat{\rho}_s|j\rangle\langle i|i\rangle\langle j|)\right)|m\rangle \quad .\end{aligned} \tag{B.3}$$

The single terms of Eq. B.3 will be treated separately.

B.1 Hamiltonian part

The change of the density matrix elements in time due to the Hamiltonian evolution results in

$$\begin{aligned}\langle n|\dot{\rho_H}|m\rangle &= -\frac{i}{\hbar}\langle n|(\hat{H}_s\hat{\rho}_s - \hat{\rho}_s\hat{H}_s)|m\rangle \\ &= -\frac{i}{\hbar}\langle n|\left(E_n\hat{\rho}_s - \hat{\rho}_s E_m\right)|m\rangle \\ &= -\frac{i}{\hbar}\langle n|E_n\hat{\rho}_s|m\rangle - \langle n|\hat{\rho}_s E_m|m\rangle \\ &= -\frac{i}{\hbar}(E_n - E_m)\langle n|\hat{\rho}_s|m\rangle \quad . \end{aligned} \tag{B.4}$$

The complete term vanishes for the diagonal elements, where $n = m$.

B.2 Dissipative part

By exploiting orthonormality, $\langle i|j\rangle = \delta_{ij}$, the second term of Eq. B.3 becomes

$$\begin{aligned}\langle n|\dot{\rho_D}|m\rangle &= \sum_{i\neq j}\Gamma_{ij}\langle n|i\rangle\langle j|\hat{\rho}_s|j\rangle\langle i|m\rangle \\ &\quad -\frac{1}{2}\sum_{i\neq j}\Gamma_{ij}\left(\langle n|j\rangle\langle j|\hat{\rho}_s|m\rangle + \langle n|\hat{\rho}_s|j\rangle\langle j|m\rangle\right) \quad . \end{aligned} \tag{B.5}$$

In the first term, products $\langle n|i\rangle$ as well as $\langle i|m\rangle$ appear. Thus this term will only contribute if $i = n = m$. The same holds for the second term with products $\langle n|j\rangle$ and $\langle j|m\rangle$. In this way, Eq.B.5 becomes for the diagonal elements ($m = n$)

$$\begin{aligned}\langle n|\dot{\rho_D}|n\rangle &= \sum_{j\neq n}\Gamma_{nj}\langle j|\hat{\rho}_s|j\rangle - \frac{1}{2}\sum_{i\neq n}\Gamma_{in}\left(\langle n|\hat{\rho}_s|n\rangle + \langle n|\hat{\rho}_s|n\rangle\right) \\ &= \sum_{j\neq n}\Gamma_{nj}\langle j|\hat{\rho}_s|j\rangle - \langle n|\hat{\rho}_s|n\rangle\sum_{i\neq n}\Gamma_{in} \\ &= \sum_{m\neq n}\Gamma_{nm}\langle m|\hat{\rho}_s|m\rangle - \langle n|\hat{\rho}_s|n\rangle\sum_{m\neq n}\Gamma_{mn} \quad . \end{aligned} \tag{B.6}$$

In the same way,

$$\langle n|\dot{\rho_D}|m\rangle = -\frac{1}{2}\sum_{i\neq n}\Gamma_{in}\langle n|\hat{\rho}_s|m\rangle - \frac{1}{2}\sum_{i\neq m}\Gamma_{im}\langle n|\hat{\rho}_s|m\rangle$$

$$
\begin{aligned}
&= -\frac{1}{2}\langle n|\hat{\rho}_s|m\rangle \sum_{i\neq n} (\Gamma_{in} + \Gamma_{im}) \\
&= -\frac{1}{2}\langle n|\hat{\rho}_s|m\rangle \sum_{k\neq n} (\Gamma_{kn} + \Gamma_{km}) \qquad \text{(B.7)}
\end{aligned}
$$

for the off-diagonal elements ($m \neq n$) is obtained.

In summary, the time evolution of the density matrix elements is given for the diagonal elements by

$$
\begin{aligned}
\langle n|\dot{\hat{\rho}}_s|n\rangle &= \sum_{m\neq n} \Gamma_{nm}\langle m|\hat{\rho}_s|m\rangle - \langle n|\hat{\rho}_s|n\rangle \sum_{m\neq n} \Gamma_{mn} \\
= \dot{\rho}_{nn} &= \sum_{m\neq n} \Gamma_{nm}\,\rho_{mm} - \rho_{nn} \sum_{m\neq n} \Gamma_{mn} \qquad \text{(B.8)}
\end{aligned}
$$

and for the off-diagonal elements

$$
\begin{aligned}
\langle n|\dot{\hat{\rho}}_s|m\rangle &= -\frac{i}{\hbar}(E_n - E_m)\langle n|\hat{\rho}_s|m\rangle - \frac{1}{2}\langle n|\hat{\rho}_s|m\rangle \sum_{k\neq n} (\Gamma_{kn} + \Gamma_{km}) \\
= \dot{\rho}_{nm} &= -\frac{i}{\hbar}(E_n - E_m)\,\rho_{nm} - \frac{1}{2}\,\rho_{nm} \sum_{k\neq n} (\Gamma_{kn} + \Gamma_{km}) \qquad \text{(B.9)}
\end{aligned}
$$

is obtained.

Bibliography

[1] G. Ertl. *Angew. Chem.*, 102:1258, 1990.

[2] G.A. Somorjai. *Introduction to Surface Chemistry and Catalysis.* Wiley, New York, 1994.

[3] D.J. DiMaria and E.Cartier. *J. Appl. Phys.*, 78:3883, 1995.

[4] Ph. Avouris. *Acc. Chem. Res.*, 28:95, 1994.

[5] K. Christmann. *Introduction to Surface Physical Chemistry.* Springer Verlag, New York, 1991.

[6] S.J. Lombardo and A.T. Bell. *Surf. Sci. Rep.*, 13:1, 1991.

[7] H.-L. Dai and W. Ho (eds.). *Laser Spectroscopy and Photochemistry on Metal Surface.* World Scientific, Singapore, 1995.

[8] G.Binning , H. Rohrer , Ch. Gerber and E. Weibel. *Phys. Rev. Lett.*, 49:57, 1982.

[9] G.A.D. Briggs and A.J. Fisher. *Surf. Sci. Rep.*, 33:1, 1999.

[10] W. Ho. *Acc. Chem. Res.*, 31:567, 1997.

[11] F.M. Zimmermann and W. Ho. *Surf. Sci. Rep.*, 22:127, 1995.

[12] H. Guo , P. Saalfrank and T. Seideman. *Prog. Surf. Sci.*, 62:239, 1999. and references therein.

[13] A.H. Zewail. *Ultrafast dynamics of the Chemical Bond.* World Scientific, Singapore, 1994.

[14] R.E. Walkup , D.M. Newns and Ph. Avouris. *Atomic and Nanometer Scale Modification of Materials.* Kluwer, Dordrecht, 1993.

[15] D.M. Eigler and E.K. Schweizer. *Nature (London)*, 344:524, 1990.

[16] G. Meyer, L. Bartels, S. Zophel, E. Henze and K.-H. Rieder,. *Phys. Rev. Lett.*, 78:1512, 1997.

[17] Ph. Avouris , R.E. Rossi , H.C. Akpati , P. Nordlander , T.-C. Shen , G.C. Abeln and J.W. Lyding. *Surf. Sci.*, 363:368, 1996.

[18] T.-C. Sheng , C. Wang , G.C. Abeln , J.R. Tucker , J.W. Lyding , Ph. Avouris and R.E. Walkup. *Science*, 268:1590, 1995.

[19] K. Stokbro, B. Yu-Kuang Hu, C.Thirstrup, and X.C. Xie. *Phys. Rev. B*, 58:8038, 1998.

[20] D.M. Eigler , C.P. Lutz and W.E. Rudge. *Nature (London)*, 352:600, 1991.

[21] L. Bartels, G. Meyer, K.-H. Rieder, D.Velic, E. Knoesel, A. Hotzel, M. Wolf and G. Ertl. *Phys. Rev. Lett.*, 80:2004, 1998.

[22] L. Bartels, G. Meyer and K.-H. Rieder. *Appl. Phys. Lett.*, 71:213, 1997.

[23] U. Quaade, K. Stokbro, C.Thirstrup and F. Grey. *Surf. Sci.*, 415:L1037, 1998.

[24] W. Ho. *Acc. Chem. Res.*, 31:567, 1998.

[25] I.-W. Lyo and Ph. Avouris. *Science*, 253:173, 1991.

[26] B.N.J. Persson and Ph. Avouris. *Surf. Sci.*, 390:45, 1997.

[27] F. Weik, A. de Meijere and E. Hasselbrink. *J. Chem. Phys.*, 99:91, 1993.

[28] W. Ho. *Surf. Sci.*, 363:166, 1996.

[29] Ph. Avouris , R.E. Walkup , A.R. Rossi , T.-C.Sheng , G.C. Abeln , J.R. Tucker and J.W. Lyding. *Chem. Phys. Lett.*, 257:148, 1996.

[30] K. Stokbro, C.Thirstrup, M. Sakurai, U. Quaade, B. Yu-Kuang Hu, F. Perez-Murano and F. Grey. *Phys. Rev. Lett*, 80:2618, 1998.

[31] P. Saalfrank. *Chem. Phys.*, 193:119, 1995.

[32] S. Harris , S. Holloway and G.R. Darling. *J. Chem. Phys.*, 102:8235, 1995.

[33] K. Blum. *Density matrix theory and applications.* Plenum Press, New York, 1981.

[34] M. Berman , R. Kosloff and H. Tal-Ezer. *J. Phys. A: Math. Gen.*, 25:1283, 1992.

[35] P. Saalfrank and R. Kosloff. *J. Chem. Phys.*, 105:2441, 1996.

[36] P. Saalfrank , R. Baer and R. Kosloff. *Chem. Phys. Lett.*, 230:463, 1994.

[37] G. Lindblad. *Commun. Math. Phys*, 48:119, 1976.

[38] A.G. Redfield. *Adv. Magn. Reson.*, 48:119, 1956.

[39] D. Menzel and R. Gomer. *J. Chem. Phys.*, 41:3311, 1964.

[40] P.A. Redhead. *Can. J. Phys.*, 42:886, 1964.

[41] P.R. Antoniewicz. *Phys. Rev. B*, 21:3811, 1980.

[42] J.W. Gadzuk , L.J. Richter , S.A. Buntin , D.S. King and R.R. Cavanagh. *Surf. Sci.*, 235:317, 1990.

[43] J.W. Gadzuk. *Phys. Rev. B*, 44:13, 1991.

[44] E. Hasselbrink, M. Wolf, S. Holloway and P. Saalfrank. *Surf. Sci.*, 363:179, 1996.

[45] C. Daniel, R. de Vievie-Riedle , M.-C. Heitz , J. Manz and P. Saalfrank. *Int. J. Quant. Chem.*, 57:595, 1996.

[46] P. Saalfrank and T. Klamroth. *Ber. Bunsenges. Phys. Chem.*, 99:463, 1995.

[47] Chakrabarti, V. Balasubramanian, N.Sathyamurthy N and J.W. Gadzuk. *Chem. Phys. Lett.*, 242:490, 1995.

[48] S.A. Buntin, L.J. Richter, R.R. Cavanagh and D.S. King. *Phys. Rev. Lett.*, 61:1321, 1988.

[49] S.A. Buntin, L.J. Richter, D.S. King and R.R. Cavanagh. *J. Chem. Phys.*, 91:6429, 1989.

[50] G. Lindblad. *Commun. Math. Phys.*, 48:119, 1976.

[51] V. Gorini , A. Kossakowski and E.C. Sudarshan. *J. Math. Phys.*, 17:821, 1976.

[52] H. Tal-Ezer. High degree interpolation polynomial in newton form. Icase report no 88–93, NASA Langley Research Center, Hampton, 1988.

[53] L.N. Trefethen. *J. Sci. Stat. Comp.*, 1:82, 1980.

[54] G. Ahskenazi , R. Kosloff , S. Ruhmann and H. Tal-Ezer. *J. Chem. Phys.*, 103:10005, 1995.

[55] K. Mølmer , Y.Castin and J. Dalibard. *J. Opt. Soc. Am. B*, 10:524, 1993.

[56] P. Gaspard and M.Nagaoka. *J. Chem. Phys.*, 111:5668, 1999.

[57] P. Gaspard and M.Nagaoka. *J. Chem. Phys.*, 111:5676, 1999.

[58] W.T. Strunz, L. Disi and N. Gisin. *Phys. Rev. Lett.*, 82:1801, 1999.

[59] B. Wolfseder and W. Domcke. *Chem. Phys. Lett.*, 235:370, 1995.

[60] K. Finger and P. Saalfrank. *Chem. Phys. Lett.*, 268:291, 1997.

[61] P. Saalfrank. *Chem. Phys.*, 211:265, 1996.

[62] P. Saalfrank , G. Boendgen, K. Finger and L. Pesce. *Chem. Phys.*, 251:51, 2000.

[63] G. Boendgen and P. Saalfrank. *J. Phys. Chem. B*, 102:8029, 1998.

[64] P. Saalfrank, G. Boendgen, C. Corriol and T. Nakajima. *Faraday Discussions*, 117, 2000. in press.

[65] G.Binnig and H. Rohrer. *Rev. Mod. Phys.*, 57:615, 1987.

[66] R.M. Feenstra. *Surf. Sci.*, 299:965, 1994.

[67] H.C. Akpati , P. Nordlander , L.Lou and Ph. Avouris. *Surf. Sci.*, 372:9, 1997.

[68] P. Kratzer. *Phys. Stat. Sol.*, 159:91, 1997.

[69] K. Christmann. *Surface Sci. Rept.*, 9:1, 1988.

[70] J.J. Boland. *Advan. Phys.*, 42:129, 1993.

[71] R.A. Street. *Hydrogenated amorphous silicon.* Cambridge University Press, Cambridge, 1991.

[72] E.T. Foley , A.F. Kamm , J.W. Lyding and Ph. Avouris. *Phys. Rev. Lett.*, 80:1336, 1998.

[73] T.-C. Shen and P. Avouris. *Surf. Sci.*, 390:35, 1997.

[74] S. Maruno , H. Iwasaki , K.Horioka , S.-T-Li and S. Nakamura. *Phys. Rev. B*, 27:4110, 1993.

[75] P. Guyot-Sionnest, P.H. Lin and E.M. Miller. *J. Chem. Phys.*, 102:4269, 1995.

[76] R. Kosloff and D. Kosloff. *J. Chem. Phys.*, 79:1823, 1983.

[77] M.D. Feit , J.A. Fleck and A. Steiger. *J. Comput. Phys.*, 47:412, 1982.

[78] P. Schuck and W.Z. Brennig. *Z. Phys. B - Condensed Matter*, 46:137, 1982.

[79] T. Klamroth and P. Saalfrank. *Surf. Sci.*, 2000. in press.

[80] D. Menzel. *Surf. Sci.*, 14:340, 1969.

[81] G.P. Salam , M. Persson and R.E. Palmer. *Phys. Rev. B*, 49:10655, 1994.

[82] C.Thirstrup, M. Sakurai, T. Nakayama and K. Stokbro. *Surf. Sci.*, 424:L329, 1999.

[83] D.R. Jennison, J.P. Sullivan, P.A. Schultz, M.P. Sears and E.B. Stechel. *Surf. Sci.*, 390:112, 1997.

[84] I.-W. Lyo and Ph. Avouris. *Science*, 253:600, 1991.

[85] M. A. Rezaei, B. C. Stipe and W. Ho. *J. Chem. Phys.*, 110:4891, 1999.

[86] B.N.J. Persson and Ph. Avouris. *Chem. Phys. Lett.*, 242:483, 1995.

[87] T. Klammroth. privat communications, 2000.

[88] M. J. Frisch , G. W. Trucks , H. B. Schlegel , P. M. W. Gill , B. G. Johnson , M. A. Robb , J. R. Cheeseman , T. Keith, G. A. Petersson , J. A. Montgomery , K. Raghavachari , M. A. Al-Laham , V. G. Zakrzewski , J. V. Ortiz , J. B. Foresman , J. Cioslowski , B. B. Stefanov , A. Nanayakkara , M. Challacombe , C. Y. Peng , P. Y. Ayala , W. Chen , M. W. Wong , J. L. Andres , E. S. Replogle , R. Gomperts , R. L. Martin , D. J. Fox , J. S. Binkley , D. J. Defrees , J. Baker , J. P. Stewart , M. Head-Gordon , C. Gonzalez and J. A. Pople. Gaussian 94, revision d.4. Technical report, Gaussian, Inc., Pittsburgh PA,, 1995.

[89] D.T. Colbert and W.H. Miller. *J.Chem. Phys.*, 96:1982, 1991.

[90] K. Hermansson. *Chem. Phys. Lett.*, 233:376, 1995.

[91] C. Stuhlmann, G. Bogdami and H. Ibach. *Phys. Rev. B*, 45:6786, 1992.

[92] S. Gao , D.G. Busch and W. Ho. *Surf. Sci.*, 344:L12252, 1995.

[93] S. Gao. *Phys. Rev. B*, 55:1876, 1997.

[94] G. Ma and H. Guo. *Chem. Phys. Lett.*, 317:315, 2000.

[95] R.E. Walkup , D.M. Newns and Ph. Avouris. *Phys. Rev. B*, 48:1858, 1993.

[96] B.N.J. Persson and J.E. Demuth. *Solid State Comm.*, 57:769, 1986.

[97] S. Gao, M. Persson and B.I. Lundqvist. *Phys. Rev. B*, 55:4825, 1997.

[98] Kobayashi, Y. Toyozawa M. Ueta, H. Kanzaki, K and E. Hanamura. *Excitonic Processes in Solids.* Springer, Berlin, 1986.

[99] B.N.J. Persson and A. Baratoff. *Phys. Rev. Lett*, 59:339, 1987.

[100] K. Stokbro. *Surf. Sci.*, 429:327, 1999.

[101] P. Dumas, Y.J. Chabal and G.S. Higashi. *Phys. Rev. Lett.*, 65:1124, 1990.

[102] P. Guyot-Sionnest. *Phys. Rev. Lett.*, 67:2323, 1988.

[103] M. Nest and P. Saalfrank. J. chem. phys. 113:8753, 2000.

[104] M. Nest and P. Saalfrank. to be published, 2000.

[105] R. Zhang and D.G. Ivey. J. vac. sci. technol. b. 14:1, 1996.

[106] L. Olsson, N. Lin, V. Yakimov and R. Erlandsson. J. appl. phys. 84:4060, 1998.

[107] I. Andrianov and P. Saalfrank. to be published, 2001.

[108] T. Vondrak and X.-Y. Zhu. *Phys. Rev. Lett.*, 82:1967, 1999.

[109] T. Vondrak and X.-Y. Zhu. *J. Phys. Chem.*, 103:4892, 1999.

[110] T. Hertel, M. Wolf and G. Ertl. *J. Chem. Phys.*, 102:3414, 1995.

[111] X.-Y. Zhu and J.M. White. *Phys. Rev. Lett.*, 68:3359, 1992.

[112] K.-H. Bornscheuer, W. Nessler, M. Binetti, E. Hasselbrink and P. Saalfrank. *Phys. Rev. Lett.*, 78:1174, 1997.

[113] S. Shi, A. Woddy and H. Rabitz. *J. Chem. Phys.*, 88:6870, 1988.

[114] Y.J. Yan, R.E. Gillian, R.M. Whitnell, K.R. Wilson and S. Mukamel. *J. Chem. Phys.*, 97:2320, 1993.

[115] A. Bartana, R. Kosloff and D.J. Tannor. *J. Chem. Phys.*, 99:196, 1993.

[116] R. Schinke. *Photodissociation Dynamics.* Cambridge University Press, Cambridge, 1993.

[117] T. Klamroth and P. Saalfrank. *Surf. Sci.*, 410:21, 1998.

[118] A. Pusel, U. Wetterauer and P. Hess. *Phys. Rev. Lett.*, 81:645, 1998.

[119] S. Ruhman and R. Kosloff. *J. Opt. Soc. Am. B*, 7:1748, 1990.

[120] G. Cerullo, C.J. Bardeen, Q. Wang and C.V. Shank. *Chem. Phys. Lett.*, 262:362, 1996.

[121] S. Chelkowski, A.D. Bandrauk and P.B. Corkum. *Phys. Rev. Lett.*, 65:2355, 1990.

[122] I. Pastirk, E.J. Brown, Q. Zhang and M. Dantus. *J. Chem. Phys.*, 108:4375, 1998.

[123] K. Mishima and K. Yamashita. *J. Chem. Phys.*, 110:7756, 1999.

[124] J. Cao, C. Bardeen and K.R. Wilson. *J. Chem. Phys.*, 113:1898, 2000.

[125] K. Fukutani, A.Peremans, K. Mase and Y. Murata. *Surf. Sci.*, 283:158, 1993.

[126] P.M. Ferm, F. Budde, A.V. Hamza, S. Jakubith, D.Weide, P. Andresen and H.-J. Freund. *Surf. Sci.*, 218:467, 1989.

[127] K. Fukutani, T.T. Magkoev, Y. Murata and K. Terakura. *Surf. Sci.*, 363:185, 1996.

[128] L.J. Richter, S.A. Buntin, D.S. King and R.R. Cavanagh. *J. Electr. Spec. Relat. Phenom.*, 54:181, 1990.

[129] T. Mull, B. Baumeister, M. Menges, H.-J. Freund, D.Weide, C. Fischer and P. Andresen. *J. Chem. Phys.*, 96:7108, 1992.

[130] M. Menges, B. Baumeister, K. Al-Shamery and H.-J. Freund. *J. Chem. Phys.*, 101:3318, 1994.

[131] J.A. Prybyla, T.F. Heinz, J.A. Misewich, M.M.T. Loy and J.H. Glowina. *Phys. Rev. Lett.*, 64:1537, 1990.

[132] G. Eichhorn, M. Richter, K. Al-Shamery and H. Zacharias. *Surf. Sci.*, 368:67, 1996.

[133] P. Saalfrank. *Surf. Sci.*, 390:1, 1997.

[134] O. Kühn and V. May. *Chem. Phys.*, 208:117, 1996.

[135] H. Guo. *J. Chem. Phys.*, 106:1967, 1997.

[136] F.M. Zimmermann. *Surf. Sci.*, 390:174, 1997.

[137] W. Reimer, T. Fink and J. Küppers. *Surf. Sci.*, 193:259, 1988.

[138] H. Guo and F. Chen. *Faraday Discuss.*, 108:1, 1997.

[139] D.M. Newns, T.F. Heinz and J.A. Misewich. *Prog. Theo. Phys. Suppl.*, 106:411, 1991.

[140] P.B. Corkum, F. Burnel, N.K. Sherman and T. Srinivasan. *Phys. Rev. Lett.*, 61:2886, 1988.

[141] D.O. Harris , G.G. Engerholm and W.D. Gwinn. *J. Chem. Phys.*, 43:1515, 1965.

[142] A.S. Dickinson and P.R. Certain. *J. Chem. Phys.*, 49:4209, 1968.

[143] J.V. Lill , G.A. Parker and J.C. Light. *Chem. Phys. Lett.*, 89:483, 1982.

[144] J.C. Light , I.P. Hamilton and J.V. Lill. *J. Chem. Phys.*, 82:1400, 1985.